Accurate Needle Insertion and Tissue Sampling in Biopsy

by

Dian-Ru Li

A dissertation submitted in partial fulfillment
of the requirements for the degree of
Doctor of Philosophy
(Mechanical Engineering)
in the University of Michigan
2019

Doctoral Committee:

Professor Albert J. Shih, Chair
Associate Professor Cynthia Chestek
Research Investigator Lei Chen
Professor Kornel Ehmann
Assistant Research Scientist Grant Kruger
Professor Jeffrey S. Montgomery
Assistant Professor Alex Shorter

Dian-Ru Li

drli@umich.edu

ORCID iD: 0000-0003-0348-8104

© Dian-Ru Li 2019

Dedication

To my family, thank you all for your love and support to help me get through this journey.

To those who guided me, helped me, take care of me, and love me, thank you all for making me strong and undefeatable.

This dissertation is dedicated to all of you.

Acknowledgments

I sincerely appreciate everyone that has helped, guided me, and supported me along my way through this doctorate degree. I regret not being able to put everyone's name down here, but I will try my best to name a few.

First, I would like to express my greatest appreciation to my advisor, Prof. Albert Shih. He has been a great mentor who is always willing to spend time on me to understand my barriers, coaches me to overcome all the challenges, and guides me to enhance my academic and professional capabilities. He always encourages me to get involved with different projects and training programs to acquire versatile skills beyond my main research topic. I really appreciate Prof. Shih for bring so many positive changes in my life personally and professionally and unconditionally supporting me to get through this tough but enriching PhD journey.

I also want to express my great gratitude to my dissertation committee for their guidance and support. I would like to thank Prof. Kornel Ehmann for looking for the funding opportunity for my research and guiding me to form the research goals at the beginning of my PhD journey. I would like to thank Prof. Cynthia Chestek, Prof. Alex Shorter, and Dr. Grant Kruger for their critical suggestions to refine my research plans and help me to accomplish the final steps to complete this dissertation. I would like to thank Dr. Lei Chen for being my mentor in many aspects, collaborating with me for various research projects, and motivating me all the time. Last, I would like to thank Dr. Jeffrey Montgomery for providing me the critical guidance to identify the clinical needs, closely working with me to advance the needle biopsy technology, and supporting my research in many public presentations. Without his support, all I have achieved would not have been possible.

I would like to thank all my current and past labmates at the Biomedical Manufacturing and Design Lab in the S. M. Wu Manufacturing Research Center, including (in no particular order):

Jeff Plott, Yang Liu, Robert Chisena, Yihao Zheng, Ketut Bagus Priambada, Matthew Hildner, Jingxuan (Jessie) Lyu, Tianshu (Kelly) Dong, Miguel Angel Funes Lora, Nathaly Villacis, William Van den Bogert, Lindsey Furness, Anni Wang, Barry Belmont, Roland Chen, and Bruce Tai. I am really lucky to have a wonderful research group where everyone supports each other, helps each other, encourages each other, and loves each other.

I would like to sincerely thank Steve Field, John Schaftenaar, and Patrick Grashorn at Inrad Inc. for supporting my research and closely collaborating with us to develop the new needle biopsy device. They provided the most critical assistance to let me make the great progress in my PhD studies and successfully acquire several research funding opportunities. I also want to thank the Michigan Medicine Pathology Morgue for the assistance in obtaining the cadaver prostate tissue to bring the significance to my research study.

Additional thanks to the funding grants that support my PhD studies: NSF CMMI grant #1266063, NIH National Cancer Institute STTR Phase I #R41CA228877, and NSF INTERN program 17-091. Special thanks to the University of Michigan Coulter Translational Research Partnership Program (Thomas Marten and Matthew Okoneski) for the support of my side projects.

I would like to thank my master advisor at National Taiwan University, Prof. Hao-Ming Hsiao. He has been a great mentor and also a good friend to give me opportunities to equip myself with versatile skills, encourage me to start this PhD journey, and support me to acquire the admission to University of Michigan.

Finally, I would like to thank my family for their unconditional support and love to make me feel beloved and brave. I would also want to thank all my friends in Taiwan and the US. They provided so many mental supports to enrich my PhD life. I feel blessed to have them accompany me, share every great moment with me, and encourage me all the time even some of them are not physically here with me. I would like to thank my amazing roommate, Shan-Huey (Erin) Yu, for taking care of me every day, keeping my PhD life in order, and treating me like a family. Last, I would like to thank my love, Hung-Hsi Lin, for always being there for me, making me happy, and loving me wholeheartedly. I am so thankful to have him by my side.

Thank you, all of you, for making me who I am today.

Table of Contents

List of Figures

Abstract

Needle biopsy is a minimally invasive clinical procedure to acquire tissue samples from various organs, such as lymph node, lung, breast and prostate, for pathological diagnosis of cancer. Accurate needle deployment and adequate tissue sampling in biopsy are crucial for accurate diagnosis and individualized treatment decisions. Advances in medical imaging can identify suspicious cancerous lesions as targeted sites for biopsy to improve the disease assessment. As the use of targeted biopsy expands, the sub-mm accuracy for needle deployment is clinically desired but technically challenging. During the biopsy procedure, the needle insertion force deforms and moves the soft tissue and the surrounding organ. Currently available biopsy needles often induce significant needle deflection. Such deflection causes variances in targeted and actual locations of the sampled tissue core, leading to lesion undersampling, false-negative and cancer misdiagnosis. Prior researches of needle insertion have identified the needle insertion motion and needle tip geometry as the main factors affecting needle deployment accuracy. Robotic needle steering has been developed for accurate needle guidance. However, there is not yet a needle biopsy technology that can be effectively adopted for clinical use. Furthermore, relationship between needle deployment accuracy and tissue sampling volume, two key factors affecting cancer diagnostic accuracy, remains unexplored.

This dissertation aims to establish the scientific and technological foundations for accurate needle insertion and tissue sampling in biopsy. First, the effect of needle insertion motion on the tissue deformation and organ displacement was studied. The mosquito-proboscis inspired (MPI) insertion was developed to reduce the local tissue deformation and global prostate displacement during needle insertion. Second, the effect of needle tip geometry on needle deflection and tissue sampling length was investigated to understand the needle-tissue interaction in biopsy. Third, the multi-bevel needle tip geometries were explored to identify the biopsy needle design criteria

enabling low needle deflection and high tissue sampling. Last, a needle-tissue interaction modeling using the Lagrangian analysis coupled with smoothed particle Galerkin method (L-SPG) was formulated to study the needle deflection and tissue deformation during needle insertion.

The MPI needle insertion demonstrated the capability to reduce the local tissue deformation and global prostate displacement, by up to 38% and 48%, respectively, when compared to the traditional direct needle insertion. The tissue separation location at the needle tip was revealed to affect both needle deflection and tissue sampling length. By varying the tissue separation location and creating a multi-bevel needle tip geometry, the bending moments could be altered to reduce the needle deflection. However, the tissue separation location also affected the tissue contact inside the needle groove, potentially reducing the tissue sampling length. Two critical design criteria for biopsy needle were identified: 1) the tissue separation point below the needle groove face and 2) the multi-bevel needle tip geometry generating the upward forces while maintaining the low separation point. A multi-bevel needle achieving the above criteria demonstrated the reduced needle deflection (with up to 88% reduction in magnitude) and equivalent tissue sampling length when compared to current biopsy needle design. Finally, the L-SPG model was established to simultaneously model the needle deflection and tissue deformation during needle insertion. This L-SPG model achieved a reasonably good prediction on the correlation of the needle tip type vs. the resultant needle deflection and tissue sampling length, matching the trend observed in the experimental results.

Chapter 1: Introduction

1.1 Motivation

Needle biopsy is a minimally invasive tissue sampling method for cancer diagnosis of various organs such as lymph node, breast, lung, liver, and prostate. Accurate needle deployment and adequate tissue sampling are crucial for accurate cancer diagnosis and individualized treatment decisions [1–4]. With more recent advances in medical imagining, particularly magnetic resonance imagining (MRI), suspicious cancerous lesions can be identified for targeted biopsy. Although intraoperative MRI can help precisely guide the needle to the targeted site [5, 6], high cost and low availability make this method prohibitive. Ultrasound guidance is commonly used to navigate the needle in clinical procedures; however, it is blind to the cancerous lesions [1, 7, 8]. Multimodality imaging technology has allowed the fusion of MRI and ultrasound images to provide the real-time needle guidance to the targeted lesion site in many biopsy procedures [9–13]. One of the examples is the co-registered MRI-ultrasound fusion targeted biopsies (MRF-TB) for prostate cancer diagnosis [14–17].

The MRF-TB procedure is illustrated in Fig. 1-1. This procedure is commonly performed using a trucut needle biopsy device with a solid needle (inside) and a hollow cannula (outside) to acquire the tissue sample. As shown in Fig. 1-1(a), the trucut needle has a sharp tip with a single-bevel face and a groove (on the same side) to store the biopsied tissue sample cut by the outer cannula. During tissue sampling, the mechanical springs in the handle of the trucut biopsy device actuate the needle and cannula sequentially to advance through the targeted lesion site at high speed (about 4 m/s) to cut and store the tissue sample inside the needle groove. This particular needle geometry and high-speed insertion has been found to enable better cancer diagnostic accuracy due to intact tissue architecture after biopsy [18, 19]. The trucut needle device has also

been used in lymph node [20], breast [21], liver [22] and other biopsy procedures. Another common needle biopsy type is called end-cut biopsy which utilized a hollow cannula to extract the tissue sample and is typically used in the procedure with lower insertion speed and shorter insertion depth when compared to trucut biopsy. Needle targeting accuracy is typically not a major concern in end-cut biopsy.

Figure 1-1(b) shows a transrectal ultrasound (TRUS) image fused with a targeted lesion identified by MRI in MRF-TB. The purple contour illustrates the original shape of prostate in MRI. After the prostate is compressed by the ultrasound probe, it is deformed to the shape of yellow contour. The cancerous lesion and its center as the target for needle insertion are marked as the green contour and red point, respectively. The ideal path (marked by the pink dotted line), defined as a line through the target (lesion center), is displayed to assist urologists with needle targeting.

Despite proven advantages of MRF-TB, the diagnostic accuracy is limited by current needle insertion process. Figs. 1-1(c)-(h) illustrate two sources of error in two phases of MRF-TB:

- Phase I – Low-speed pre-insertion for needle positioning: The needle and cannula are positioned in proximity to the targeted cancerous lesion site. The current needle delivery process deforms and moves the surrounding tissue and prostate, altering the target location as shown in Fig. 1-1(c). During the insertion, the needle and cannula are directly inserted together at a low speed (1-10 mm/s), exerting the compression and friction forces on the tissue as shown in Fig. 1-1(d). The compression force at the needle tip contacts and compresses the tissue. The friction forces on the needle and cannula surfaces are acting along the same directions, together deforming and dragging the tissue during the insertion. This potentially induces a significant displacement of the target prior to needle firing for tissue sampling and decreases the needle targeting accuracy.
- Phase II – High-speed needle firing for tissue sampling: Once the needle is positioned to the proximity of targeted lesion (Fig. 1-1(e)), it is followed by a high-speed needle firing (as discussed previously) to cut and store the tissue sample inside the needle groove. The single-bevel needles in the current biopsy devices can deflect (or bend) significantly in MRF-TB [23, 24], forming an arc rather than a straight line through the targeted lesion center as shown in Fig. 1-1(f). The actual needle path, marked by the yellow line, is deviated from the ideal path due to the needle deflection. The needle deflection is due to the cutting force, tip force, tissue pressure, and friction force creating the unbalanced moments which bend the needle as shown in Fig. 1-

1(g). The cutting force is generated at the needle tip point A, where tissue is cut and separated (as illustrated by the red arrows in 1-1(g)). The separated tissue contacts the bevel face of the needle tip and creates a downward face force, inducing needle deflection [25]. The needle-tissue interaction also generates a distributed tissue pressure (acting on regions of direct contact between tissue and needle) and friction force on the needle, which can further aggravate the deflection (Fig. 1-1(g)).

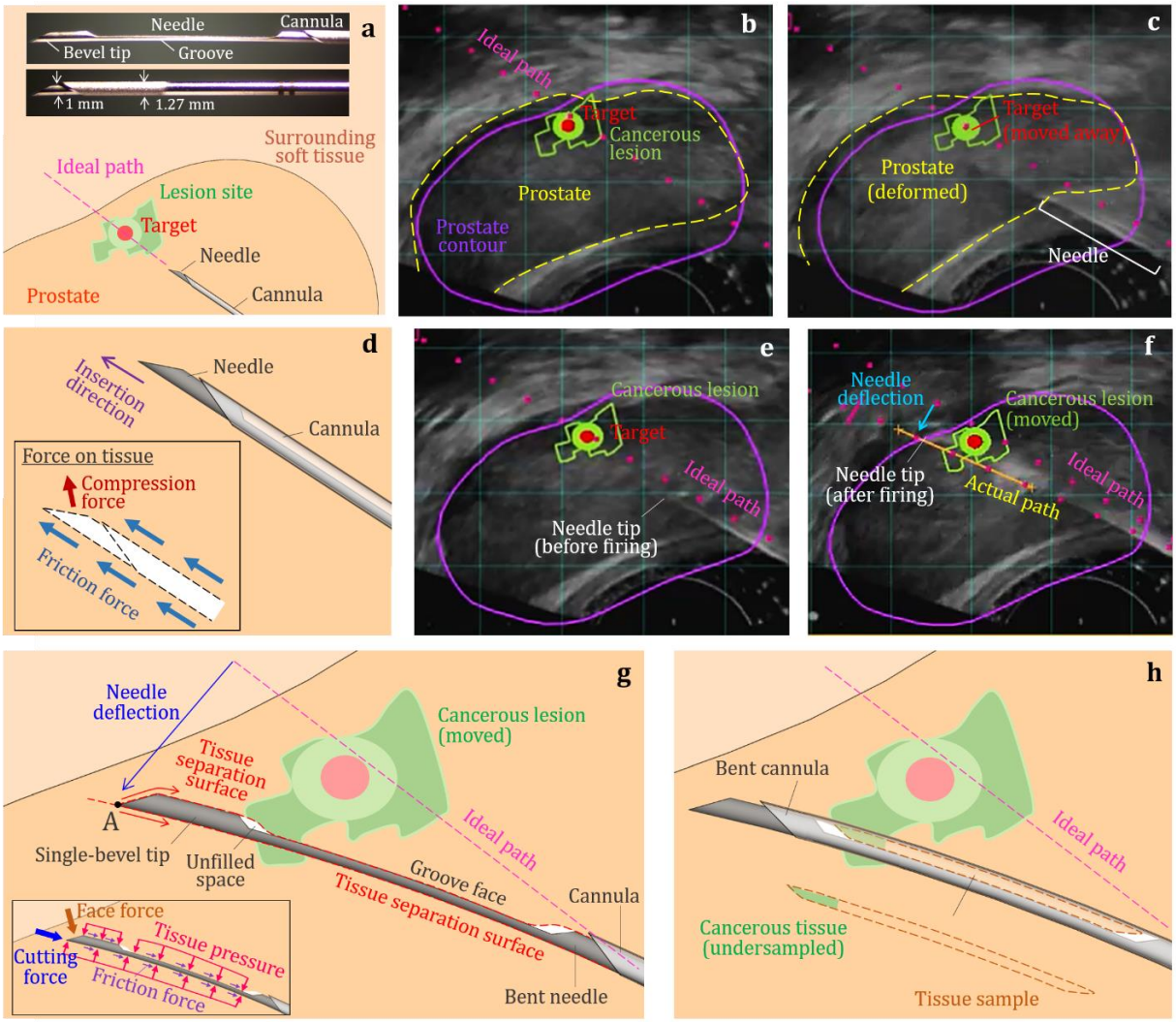

Fig. 1-1 MRF-TB procedure: (a) a commercial biopsy needle and cannula (Pro-Mag Ultra Biopsy Needle by Argon Medical Devices, Frisco, Texas, USA) and overall three dimensional (3D) model of the cancerous prostate, needle, and cannula, (b) MRF-TB image with pre-identified cancer site, (c) the deformation and displacement of prostate which move the target location away from the ideal needle insertion path in Phase I, (d) the current need delivery process where the needle and cannula are inserted together and generate the forces on the tissue which deform and push the tissue forward during insertion, (e) the needle position in proximity to the targeted lesion before the needle firing, (f) the bent needle, cannula, and displaced cancer site after high speed needle firing in Phase II, (g) the needle deflection, tissue separation surfaces initiated at the needle tip point A, and the cutting force, face force, tissue pressure, and friction force acting on the needle during insertion, (h) undersampled cancerous tissue due to needle deflection.

Such target displacement and needle deflection in Phases I and II, respectively, cause the needle to miss or undersample (failing to sample the lesion center) the targeted lesion as shown in Fig. 1-1(h). Since prostate lesions tend to be heterogeneous with more aggressive cancer cells at the lesion center [26], such sampling errors can have clinical impacts such as false-negative and cancer misdiagnosis [27, 28]. In prostate biopsy, urologists often obtain extra biopsy cores from each targeted site to account for the sampling uncertainty due to needle deflection. Even with this multiple-biopsy approach, clinically significant cancer was still undersampled in 135 of 1,003 MRF-TB cases (13.5%) [29]. More needle passes also result in greater patient risk for complications including pain, infection and bleeding, negatively impacting the patient's experience [30]. This affirms the clinical need for the needle biopsy technology enabling accurate needle insertion and tissue sampling to improve the cancer diagnostic accuracy and patient outcome.

1.2 Literature Review

To address the aforementioned clinical needs, it is crucial to understand needle insertion mechanics to develop the supportive technology improving the biopsy procedures. Based on the literature review of existing needle insertion studies, five major areas of focus relevant to the scope of this dissertation and corresponding limitations on needle biopsy technology have been identified:

(1) *Needle insertion motion:* The needle insertion motion has a strong influence on tissue deformation during the insertion. It was observed that optimizing the needle insertion speed could minimize the tissue deformation and damage [31]. Rotational motion during needle insertion lowered the needle insertion force [32, 33] and reduced the resultant tissue deformation and displacement [34, 35]. Vibration-assisted needle cutting showed the similar benefit of reducing the deformation of surrounding tissue due to the smaller insertion force [36, 37]. The incremental insertion with relative motions among the needle components was studied and demonstrated the reduction in targeted tissue displacement during the insertion [38]. However, it is technically challenging to implement these motions

into the current hand-held biopsy devices. Furthermore, the suitable needle insertion motion for trucut biopsy needle device in the pre-insertion of biopsy (Phase I) still remains unknown.

(2) *Needle tip geometry:* Besides needle insertion motion, the needle tip geometry is another factor affecting insertion force and inducing needle deflection [25]. Needle tip cutting edge could be characterized by the rake and inclination angles [39]. It was found that the high inclination and rake angles could lower the needle rupture/insertion force [40, 41]. A needle tip with the enhanced cutting edges (by increasing inclination angle) for end-cut biopsy demonstrated the lower insertion force when compared to the two-plane symmetric needle [42]. On the other hand, the single-bevel needle tip has been found to cause a large needle deflection (larger than needle diameter) comparing to that of conical [43, 44] or Franseen needle tips [45]. Increased bevel angles reduced the needle deflection by reducing the lateral bending force at the needle tip [46]. However, the ideal biopsy needle geometry to reduce needle deflection for high-speed firing of biopsy (Phase II) also remains unknown. This limitation explains the fact that the single-bevel needle tip geometry is still widely used in the current trucut biopsy device where needle deflection remains unsolved.

(3) *Needle-tissue interaction modeling:* A model to predict the needle deflection and tissue deformation is crucial to gain insights of needle-tissue interaction and improve the needle biopsy for more accurate acquisition of targeted disease tissue enabling a definite diagnosis. Mechanics-based model is a common approach to relate needle insertion forces to needle deflection [25, 47]. The Euler-Bernoulli beam bending theory was applied to model the needle as a cantilever beam and predict the needle deflection using the measured needle insertion forces [25, 48, 49]. Finite element analysis (FEA) is another modeling approach to visualize the tissue deformation and contact with the needle during insertion. The cohesive zone (CZ) method in Lagrangian FEA was commonly applied to model the tissue rupture by assigning the tissue separation threshold level when contacting with the needle [40, 50, 51]. The CZ method enabled a better representation of the tissue deformation around the needle. However, the CZ method often suffered from the mesh distortion and required a pre-defined element separation path during needle insertion. This affirms the need of having a modeling method to effectively simulate needle insertion with soft tissue rupture. On the other hand, most models in existing studies were limited to the rigid needle

(no bending/deflection). A model to simultaneously predict the needle deflection and tissue deformation remained unexplored.

(4) *Needle steering system:* With the understanding of needle-tissue interaction, robotic needle steering has been developed for accurate needle guidance and insertion [4, 47, 52]. Rotating a beveled needle during the insertion could compensate the needle deflection and enable a predictable trajectory [4]. The multiple degrees-of-freedom robots were applied to navigate the needle with sub-mm targeting accuracy [53–55]. The robotic system was further combined with the medical imagining platform to perform the needle insertion under the imaging guidance for error compensation [53–55]. However, high cost and low availability make the robotic technique prohibitive in most clinical procedures [56]. Current biopsy procedures are still performed using the hand-held needle biopsy devices, where tissue deformation, organ displacement, and needle deflection remain as the issues (Fig. 1-1).

(5) *Tissue sampling volume:* Besides needle deployment accuracy, the tissue sampling volume in needle biopsy is also critical for accurate pathological analysis and a definite cancer diagnosis [19, 57, 58]. Tissue sampling length is the parameter used clinically to quantify the sampling amount in biopsy. Low bevel angle and high inclination angle of the needle tip could increase the sampling length in end-cut biopsy [39, 42]. Smoothly polished needle could result in a longer biopsy sample in end-cut biopsy when compared to the needle with high surface roughness [59]. However, research on the tissue sampling length in trucut needle biopsy is limited. Moreover, there is also a lack of understanding of relationship between the needle targeting accuracy and resultant tissue sampling volume, which are two key factors affecting the cancer diagnostic accuracy.

In summary, three major research gaps in this field are identified:

(1) There is a lack of needle devices/technologies that can be effectively adopted for clinical use to solve tissue deformation and needle deflection issues in Phases I and II of biopsy, respectively.

(2) Research on tissue sampling volume in trucut needle biopsy is limited. Furthermore, relationship between the needle targeting accuracy and resultant tissue sampling volume, which are two key factors affecting the cancer diagnostic accuracy, remains unknown.

(3) There is still a need of having a method to effectively model the needle insertion and reveal needle-tissue interaction during needle insertion, especially when needle deflection exists.

1.3 Research Goal and Objectives

The goal of this study is to fulfill the above identified research gaps to establish the supporting technological and scientific foundations for accurate needle insertion and tissue sampling in biopsy. To achieve this goal, four objectives are identified:

(1) Investigate needle insertion motion to develop the mosquito proboscis-inspired needle insertion to reduce tissue deformation and organ displacement in low-speed pre-insertion (Phase I) of biopsy;
(2) Understand the effect of needle tip geometry on needle deflection and tissue sampling length in biopsy procedures;
(3) Explore multi-bevel trucut biopsy needle tip geometries to identify the needle design criteria enabling low needle deflection and high tissue sampling in high-speed firing (Phase II) of biopsy;
(4) Establish the numerical predictive modeling of needle deflection and tissue deformation to investigate the needle-tissue interaction during the insertion.

Achieving these objectives will provide the engineering insights of needle-tissue interaction to establish the needle biopsy technology for more accurate and adequate acquisition of targeted disease tissue, enabling a definite diagnosis and better patient outcome.

1.4 Organization of the Dissertation

The rest of this dissertation has the following organization.

Chapter 2 investigates a mosquito-proboscis-inspired (MPI) needle insertion to reduce tissue deformation and organ displacement for low-speed pre-insertion in Phase I of biopsy. Two critical features of mosquito proboscis were adopted for current biopsy needle to create MPI needle insertion: 1) the harpoon-shape notches at the needle tip and 2) needle-cannula opposite motions for vibratory incremental insertion. The local tissue deformation and global prostate displacement during the MPI vs. traditional direct insertion were quantified by tracking the displacements of the particle-embedded tissue-mimicking phantoms based on the imaging tracking analysis.

Chapter 3 studies the effect of trucut biopsy needle tip geometry on the needle deflection and tissue sampling length for high-speed firing in Phase II of biopsy. Four needle tip geometries (single-, dual-, vertical-, and asymmetric multi-bevel) are explored. A coupled Eulerian-Lagrangian model for needle-tissue interaction is utilized to gain insights of tissue deformation, separation, and contact inside the needle groove. Multilayered tissue-mimicking phantoms are used to study needle deflection. Trucut needle biopsies of ex-vivo tissue are conducted to identify the relationship between needle tip geometry and tissue sampling length.

Chapter 4 quantifies and compares the needle deflection and tissue sampling of the current single-bevel to three multi-bevel tip geometries in trucut biopsy. The needle deflection is experimentally measured in optically transparent tissue-mimicking phantoms and analyzed by the image processing. The length and weight of sampled tissue in biopsy of ex-vivo chicken breast tissue are investigated. Finally, the evaluation of the new multi-bevel trucut needle biopsy device on human cadaver prostate is performed.

Chapter 5 establishes a needle-tissue interaction modeling using Lagrangian analysis coupled with smoothed particle Galerkin method (L-SPG) to investigate the needle deflection and tissue deformation in biopsy. The configuration of the L-SPG model is presented. The modeling results are then discussed and compared with the experimental results of needle deflection and tissue sampling (as the outcome of needle-tissue interaction) in Chapter 4.

Chapter 6 draws the conclusions and summarizes the original contributions of the dissertation. Several topics for future research are also proposed.

Chapter 2: Mosquito Proboscis-Inspired Needle Insertion to Reduce Tissue Deformation and Organ Displacement

2.1 Introduction

Mosquito proboscis is an ideal needle device which minimizes the deformation and displacement of surrounding tissue during insertion for accurate guidance to targeted vessels. The flexible proboscis has a hollow labrum (about 25 μm wide) and two maxillae (about 15 μm wide) with harpoon-shape notches on the side [60] as shown in Fig. 2-1(a). During insertion, the proboscis advances incrementally with the vibratory relative movements of the labrum and maxillae at low-frequency (2-15 Hz) [61, 62]. Figure 2-1(b) illustrates the steps of proboscis insertion into a soft tissue [60]. In Step 1, the left maxilla moves forward into the tissue at μm scale while the labrum retracts in the opposite direction with a shorter distance. Such opposite motions of labrum and maxilla stabilize the surrounding soft tissue. In Step 2, the labrum moves forward while the left maxilla retracts and the right maxilla also moves slightly backward to utilize their notches to anchor the surrounding tissue. The forward motion of right maxilla and backward motion of labrum in Step 3 mirror the motions in Step 1. In Step 4, motions of both maxillae and labrum in Step 2 are mirrored. After moving the left maxilla forward and the labrum backward in Step 5, the relative positions of two maxillae and labrum are the same as in Step 1. The proboscis has moved forward by a distance marked by the wide arrow in Fig. 2-1(b). By repeating the above steps, the proboscis incrementally advances with vibratory motions in soft tissue [63]. The harpoon-shape notches of maxillae provide critical anchoring and support to reduce tissue displacement during the proboscis insertion [60, 64].

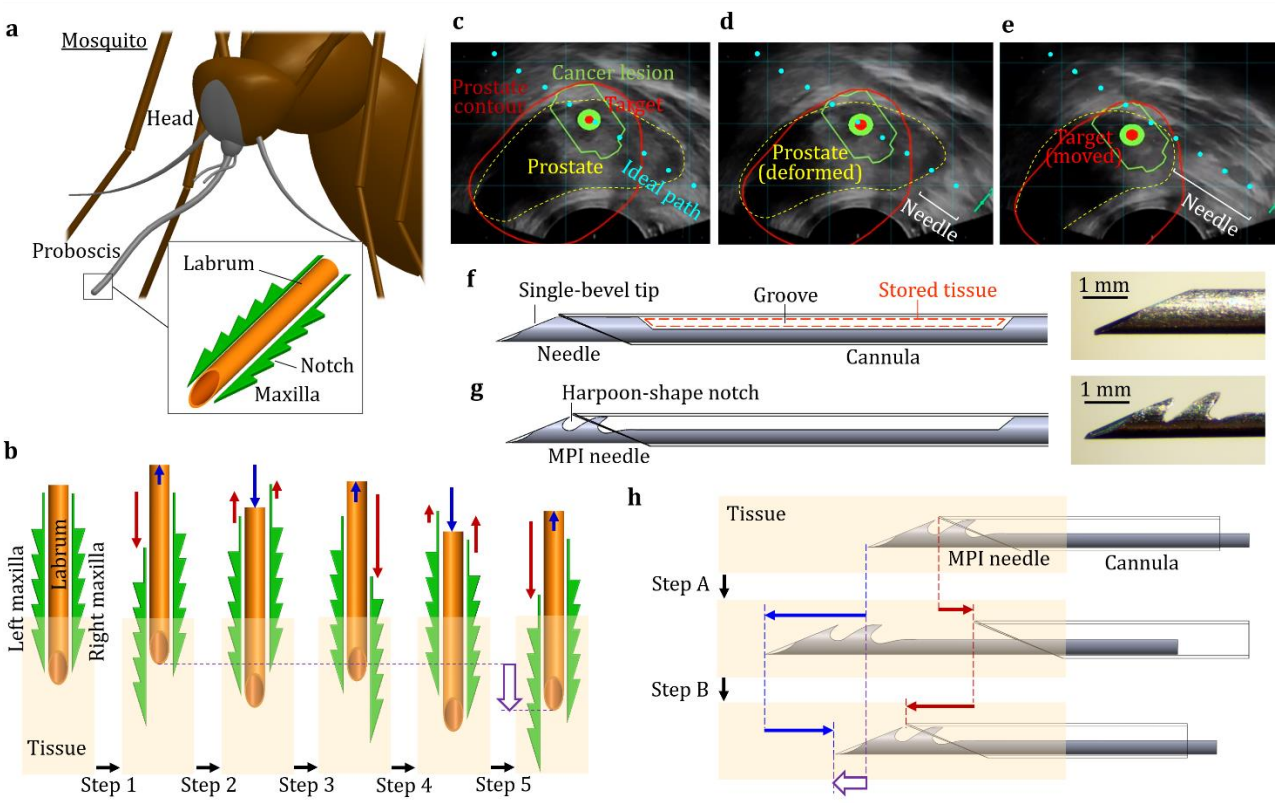

Fig. 2-1 (a) The mosquito proboscis has a hollow labrum and two harpoon-shape notched-maxillae. (b) The incremental motion during the proboscis insertion reduces surrounding tissue deformation and displacement. (c) The fused magnetic resonance-ultrasound image with pre-identified cancer lesion allows the targeted sampling of specific lesions in prostate needle biopsy. (d) The current direct needle insertion motion deforms and moves the prostate. (e) The deformation and displacement of prostate and surrounding tissue move the target location away from the ideal needle insertion path during the needle insertion. (f) The current trucut biopsy needle comprises an outer hollow cannula and an inner solid needle. (g) The mosquito-proboscis inspired needle comprises an outer hollow cannula and a needle with two harpoon-shape notches at the tip to provide critical tissue anchoring. (h) The needle-cannula incremental motion for vibratory insertion aims to reduce tissue deformation and displacement.

Tissue deformation and displacement during needle insertion are major issues for accurate needle biopsy in clinical procedures [23, 25, 29, 33]. As discussed in Section 1.1, such tissue deformation and displacement alter target position (identified cancerous lesion site) in the pre-insertion of biopsy (Phase I) and decrease the needle targeting accuracy. This issue is highlighted

in the transrectal ultrasound (TRUS) images from a clinical MRF-TB procedure for prostate needle biopsy shown in Figs. 2-1(c)-(e) for three needle positions during insertion. In Fig. 2-1(c), the MRF-TB fusion software generates features on the ultrasound image to guide the clinicians to deploy the needle to the cancerous lesion and its center (marked as the green contour and red point, respectively) for biopsy. The red contour illustrates the original shape of prostate in MRI. The ultrasound probe will compress the prostate and deform it to the shape shown as the yellow contour. The blue dots indicate the ideal needle path for clinician to follow to reach the targeted lesion site.

When the needle is inserted, the insertion force pushes the surrounding tissue, which further deforms the prostate as shown in Fig. 2-1(d). The needle then touches the prostate to the ready position of biopsy, as shown in Fig. 2-1(e). However, the prostate has been deformed and moved significantly and the target location has been moved away from the ideal path at this state before biopsy. The discrepancy between desired and actual target locations led to the needle mistargeting [24] and cause errors in tissue sampling [23, 25, 29, 33]. Such errors have the clinical impacts such as false-negative mis- or non-diagnostic biopsy and lesion undersampling [65], reducing the cancer diagnostic accuracy [29].

The current trucut biopsy needle for MRF-TB is shown in Fig. 2-1(f). This trucut needle has a solid needle (inside) with a single-bevel tip and a groove to store the sampled tissue cut by the hollow cannula (outside). In this study, two key ideas inspired by the mosquito proboscis are:

- Harpoon-shape notches at the needle tip: As shown in Fig. 2-1(g), a mosquito proboscis-inspired (MPI) needle has two harpoon-shape notches at the tip to mimic the notches in maxilla (Fig. 2-1(a)). Notches can anchor the surrounding soft tissue to reduce its deformation and displacement during needle insertion.
- Needle-cannula incremental motions for vibratory insertion: As shown in Fig. 2-1(h), the MPI needle and cannula are advanced incrementally with relative motions to mimic the movements of maxillae and labrum (Fig. 2-1(b)). In Step A, the needle moves forward while the cannula retracts to generate the opposite motion to reduce the deformation of surrounding tissue. In Step B, the cannula moves forward while the needle retracts with the notches anchoring the tissue to reduce their displacement during cannula insertion. After a complete cycle of Steps A and B, the needle and cannula move by a distance marked by the wide arrow in Fig. 2-1(h).

Bio-inspired needle design and insertion motion were investigated in prior research. An early study demonstrated the feasibility of the harpoon-shape notches in silicon needle tip for insertion into a soft tissue phantom [66]. In experiments of insertion to tissue-mimicking phantom [60] and ex-vivo tissue [67], the notched needle tips exhibited lower insertion forces when compared to the needle without notches. The insertion of a needle with four incrementally moving segments without the harpoon-shape notches was studied and showed the benefit of incremental motion to reduce the tissue displacement during insertion [38]. For the notched needle with incremental insertion motion, the puncture [68] and insertion forces [69] could be reduced by about 40% and 70%, respectively, in comparison to that of notched needle without incremental motion. The goal of this study is to utilize the above findings to create the MPI insertion applicable to existing biopsy needle (Figs. 2-1(g) and (h)) and investigate the tissue deformation and displacement during MPI insertion.

In this chapter, the particle-embedded optically transparent tissue-mimicking phantoms are utilized to experimentally quantify the deformation and displacement of the phantom induced by the needle insertion. The local tissue deformation and global prostate displacement (both based on imaging tracking of particles embedded in the phantoms) and needle insertion forces are measured to quantify effect of MPI needle insertion with incremental motion.

2.2 Materials and Methods

2.2.1 Needle Insertion Motion and Force on Tissue

The tissue deformation and displacement for three needle insertion motions shown in Fig. 2-2 are investigated and compared. The first is needle-cannula direct (NCD) insertion (Fig. 2-2(a)) which is the current biopsy needle delivery process. In NCD insertion, the needle and cannula are inserted together at a constant speed V. Three forces, the needle compression force F_c, needle friction force F_{nf}, and cannula friction force F_{cf}, exert on the tissue during insertion. The F_c at the needle tip contacts and compresses the tissue. The F_{nf} and F_{cf} have the same directions as that of horizontal component of F_c, and together generate significant displacement of surrounding soft tissue and decreasing the needle targeting accuracy of the insertion (Fig. 2-1(e)).

The second motion is needle-cannula incremental (NCI) insertion as shown in Fig. 2-2(b). The needle (without the harpoon-shape notches at the tip) and cannula advance incrementally with the relative vibratory motions in NCI insertion. From t_0 to $t_0+\Delta t$ (Step A), the needle moves forward by d_{na} while the cannula moves backward by d_{cb}. Such opposite motions of needle and cannula generate the F_{cf} against F_c and F_{nf}, reducing the surrounding tissue deformation. In Step B (from $t_0+\Delta t$ to $t_0+2\Delta t$), the cannula moves forward by d_{ca} while the needle moves backward by d_{nb}. The F_{cf} and F_{nf} are also opposite to each other to reduce the tissue displacement. The needle and cannula can advance by a distance d_{in} ($= d_{na} - d_{nb} = d_{ca} - d_{cb}$) after a complete incremental motion cycle of Steps A and B.

The third motion is mosquito proboscis-inspired (MPI) insertion as shown in Fig. 2-2(c). The MPI needle with harpoon-shape notches at the tip and cannula advance incrementally like the incremental motion of NCI insertion. The harpoon-shape notches at the MPI needle tip anchor the surrounding tissue during insertion. With the same d_{na}, d_{nb}, d_{ca}, and d_{cb} as in NCI insertion, the F_{nf} in Step A will be lower due to reduced contact area (as marked by the red dotted line in Fig. 2-2(c)). In Step B, MPI needle anchors the surrounding soft tissue by notches, generates an anchoring force F_{na} in addition to the F_{nf} to balance the F_{cf}, and further reduces the overall tissue displacement during insertion.

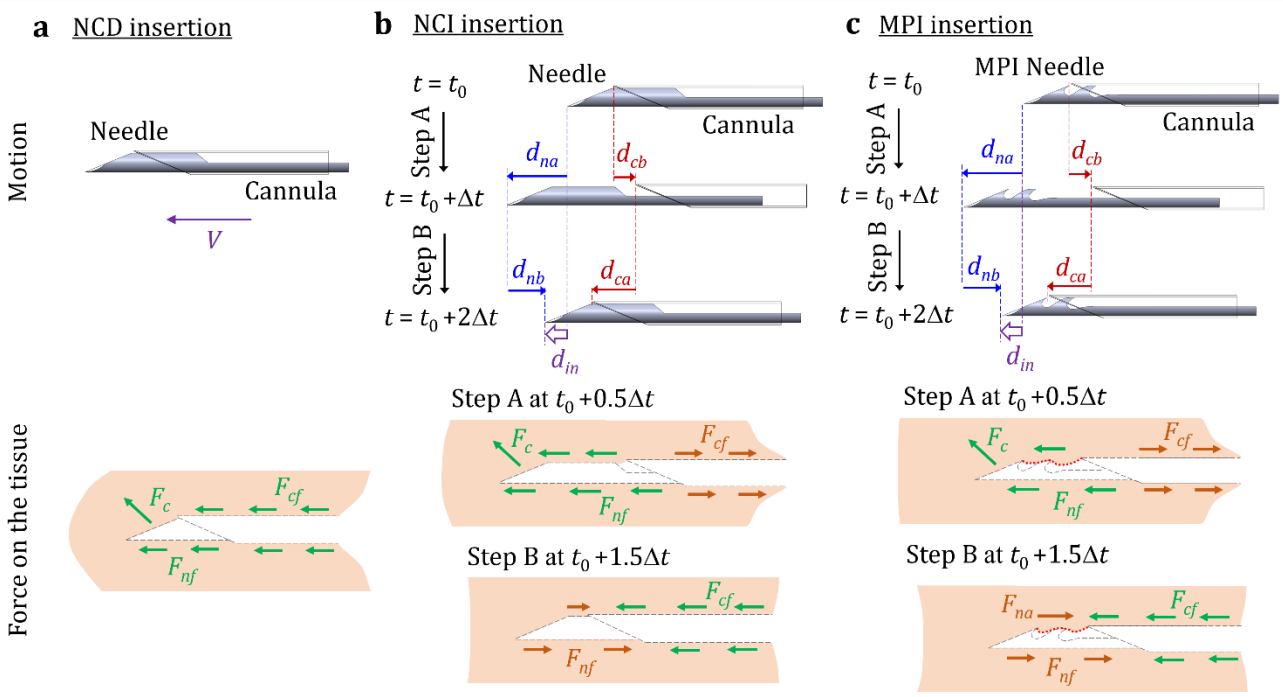

Fig. 2-2 (a) NCD insertion (the current needle delivery process): The needle and cannula are inserted together and generate the forces on the tissue which deform and push the tissue forward during insertion. (b) NCI insertion: the needle (without notches) and cannula are incrementally inserted with the opposite motions to reduce the deformation and displacement of surrounding tissue during insertion. (c) MPI insertion: the MPI needle (with notches) and cannula are incrementally inserted with notches anchoring the tissue during insertion to further reduce the overall tissue displacement.

2.2.2 Optical Measurements of Local Tissue Deformation and Global Prostate Displacement.

This study established the optical measurement methods to quantify the tissue deformation and displacement during NCD, NCI, and MPI insertion motions. The measurement setup is shown in Fig. 2-3(a). The transparent polyvinyl chloride (PVC) tissue-mimicking phantom materials with the stiffness and needle insertion properties similar to those of prostate and surrounding muscle tissues [70, 71] were used as the surrogate of the soft tissue for needle insertion experimental studies. In this study, the ratio of PVC polymer solution (liquid plastic, M-F Manufacturing), softener (plastic softener, M-F Manufacturing), and the mineral oil (white mineral oil, W.S. Dodge

Oil) was adjusted to match the stiffness and needle insertion properties to those of prostate tissues [70, 71]. Particles were embedded in the transparent phantom to visualize the displacement of phantom material during the needle insertion [38, 72].

Two particle-embedded phantoms, namely the local tissue deformation (LTD) and global prostate displacement (GPD) phantoms, were studied. The LTD phantom had a thin particle-embedded PVC (P-PVC) layer between two transparent PVC (T-PVC) layers as shown in Fig. 2-3(b). All three layers had the same material properties with the elastic modulus E of 21.3 kPa to mimic the healthy prostate tissue [73, 74]. The P-PVC layer contained the fine (240 mesh size) aluminum oxide powder for imaging tracking to measure the tissue deformation [38]. In fabrication, the heated and transparent PVC liquid mixture was poured into a phantom holder (100 mm in length, 80 mm in width and 30 mm in height) to form the first T-PVC layer with about 14 mm in height. Before this layer was completely cured, the same PVC mixture (as the T-PVC) blended with the aluminum oxide powder was poured onto the top of first layer to form a 2 mm thick P-PVC layer. Finally, the transparent PVC mixture was poured into the holder to form another 14 mm thick T-PVC layer. This three-layered LTD phantom design enabled the camera to be able to focus on particles around the needle to measure the local tissue deformation during the needle insertion (Fig. 2-3(e)).

The GPD phantom, as shown in Fig. 2-3(f), had a round prostate phantom with the outer layer (40 mm in diameter), inner core (25 mm in diameter), and surrounding soft tissue to mimic the in-vivo prostate tissues [71]. The E of the inner core, outer layer, and surrounding soft tissue was 41.7, 21.3, and 9.4 kPa, respectively (all within the range measured by elastography ultrasound of the inner and hard core of healthy prostate [73, 74]). As shown in Fig. 2-3(h), the inner core was embedded with particles (fine ground pepper powder suitable for image tracking at global scale [72]) for tracking and measuring the prostate displacement. In fabrication, the PVC liquid mixture (for E = 41.7 kPa) was first blended with about pepper powder and poured into a cylinder mold (25 mm inner diameter) placed in the middle of a 100 mm × 100 mm phantom holder (30 mm deep). Next, the PVC mixture (for E = 21.3 kPa) was poured into a cylinder mold with 40 mm inner diameter and concentric to the inner core to mold the outer layer. This outer layer was dyed in red to illustrate different tissue regions. Finally, the PVC mixture (for E = 9.4 kPa) filled the rest of the space to mimic the surrounding soft tissue.

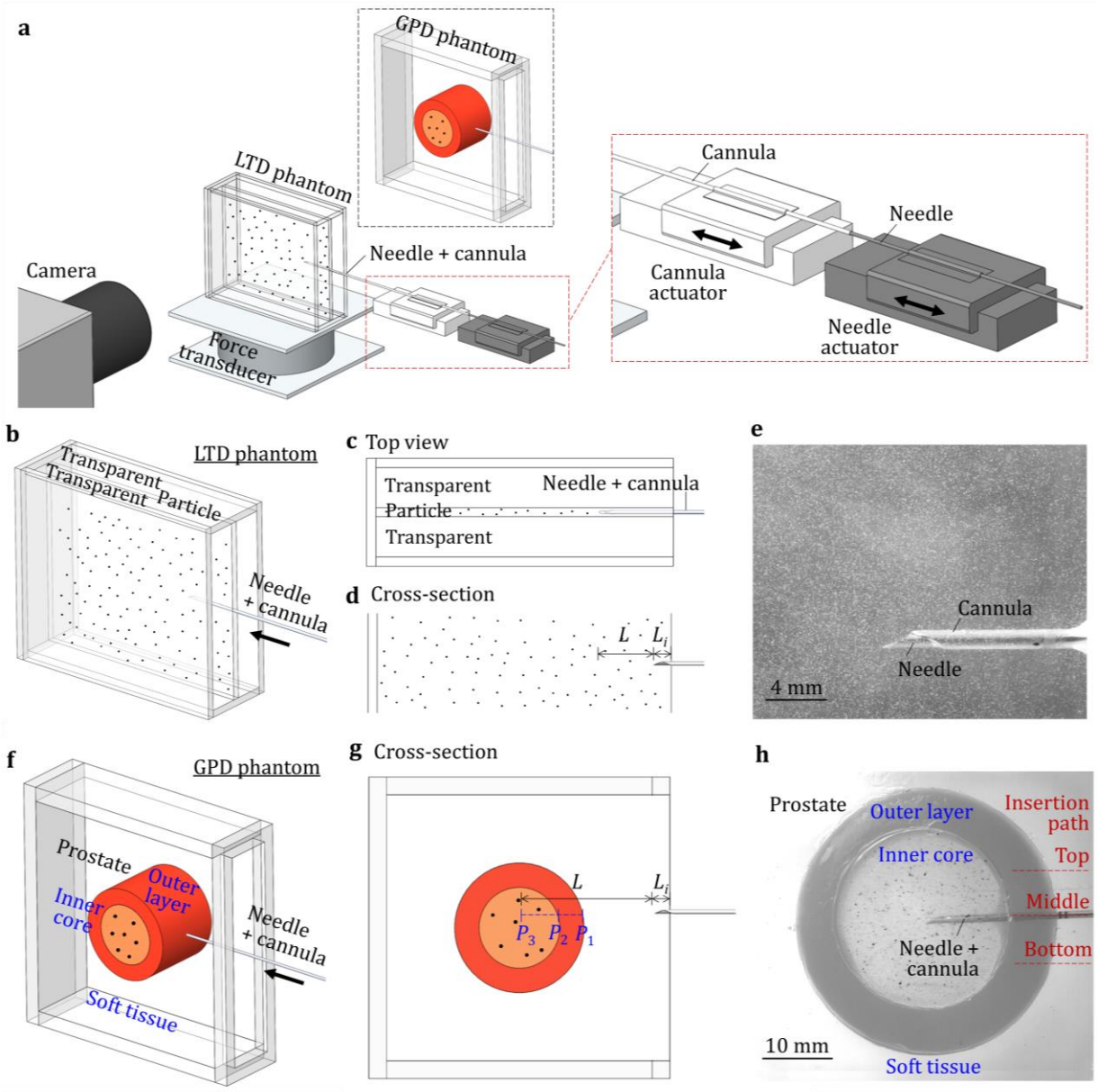

Fig. 2-3 Optical measurements of local tissue deformation and global prostate displacement during needle insertion. (a) The experimental setup for needle insertion and optical measurement. (b) The LTD phantom, needle, and cannula. (c) Top view of the LTD phantom during needle insertion. (d) Needle tip positions at the start and end of insertion into the LTD phantom. (e) An image of the needle in the LTD phantom at the end of insertion. (f) The GPD phantom, needle, and cannula. (g) Needle tip positions at the start and end of insertion into the GPD phantom. (e) An image of the needle in the GPD phantom at the end of insertion.

2.2.3 Needle Insertion Experimental Setup

The needle insertion experimental setup is shown in Fig. 2-3(a). The LTD or GPD phantom was fixed on a force transducer (Gamma F/T Sensor, ATI) to measure the needle insertion force. A high-speed camera (Model 100K, Photron) was used to record the needle insertion for imaging tracking (to be discussed in the next section). The needle and cannula were attached to two linear actuators (Model HLD 60, Moog Animatics), which were programmed using the motor control interface (SmartMotor Interface, Moog Animatics) to generate NCD, NCI, and MPI insertion motions (Fig. 2-2). The constant needle insertion speed V for NCD insertion (Fig. 2-2(a)) was 5 mm/s, close to the insertion speed in clinical prostate needle biopsy procedures [75]. For NCI and MPI insertions (Figs. 2-2(b) and (c)), the incremental motion parameters were Δt = 0.2 s, d_{na} = 4 mm, d_{nb} = 2 mm, d_{ca} = 3 mm, d_{cb} = 1 mm, and d_{in} = 2 mm (with the same average V of 5 mm/s as in NCD insertion).

2.2.4 Experimental Design

Two needle insertion experiments were performed using the LTD and GPD phantoms for measurements of the local tissue deformation and global prostate displacement, respectively. In the LTD phantom experiment, the needle tip was positioned with L_i = 3 mm and then inserted by L = 12 mm as shown in Fig. 2-3(d). Three insertion motions (NCD, NCI, and MPI) were performed at different locations of the LTD phantom. The high-speed camera with 1024 × 1024 pixel resolution and 125 fps was used to take images of embedded particles during needle insertions. The captured images were analyzed using digital image correlation (DIC) to track particle displacements and quantify the local tissue deformation during insertion.

In the GPD phantom experiment, the needle tip was positioned with L_i = 3 mm and then inserted by L = 48 mm to penetrate through the soft tissue, outer layer, into inner core, as shown in Fig. 2-3(g). The P_1, P_2, and P_3 were defined as three needle tip positions at the edge of outer layer, edge of the inner core, and end of the needle insertion, respectively. Three insertion motions (NCD, NCI, and MPI) were repeated three times for the top, middle, and bottom paths as shown in Fig. 2-3(h). The high-speed camera with 1024 × 1024 pixel resolution and 60 fps was used to capture the displacements of the particles embedded in the inner core of the GPD phantom. The global prostate displacement during insertion was measured using the particle tracking algorithm.

2.2.5 DIC for Local Tissue Deformation Measurement

The DIC analysis was applied to measure the tissue deformation. The open source 2D-DIC software (Ncorr [76]) implemented in Matlab (R2015, MathWorks) was utilized. A region of interest (ROI) in the captured image was first defined as the tissue region around the needle and cannula (details to be presented in Sec. 2.3.1). Inside the ROI, pixels overlapping with the needle and cannula during the insertion were removed to avoid DIC tracking errors due to the severe particle displacements. The backward DIC analysis in Ncorr using the last frame as the reference to back calculate the tissue deformation during the needle insertion was adopted. This allowed the measurement of large deformation.

In DIC analysis, the ROI was divided into subsets with the radius of 30 pixels and spacing of 1 pixel. The DIC algorithm calculated the deformation of surrounding tissue by searching the neighboring subsets and matching the features (based on the patterns generated by the embedded particles) between two successive frames. Two measurements in DIC, Eulerian strain and displacement, were used to visualize the local tissue deformation [76] during the needle insertion. Such local tissue deformation was quantified as a variable U_A by averaging the DIC displacement data of each pixel in a designated region A within the ROI (the region further close to the needle, details to be presented in Sec. 2.3.1).

2.2.6 Particle Tracking for Global Prostate Displacement Measurement

The particle tracking analysis was applied to measure the global prostate displacement U_p. The Kanade-Lucas-Tomasi (KLT) feature tracking algorithm in Matlab (R2015, MathWorks) was applied to measure displacements of tracking points in the GPD phantom (Fig. 2-3(h)) during the needle insertion [77]. The top 100 trackable points among the embedded particles were identified using the minimum eigenvalue method [77]. These 100 points were tracked frame by frame during insertion. Tracking points which overlapped with the needle during insertion were removed. The displacements of tracking points between the initial and deformed positions for each frame were calculated. The average displacement of all tracking points without overlapping with the needle and cannula was calculated as U_p.

2.3 Results

2.3.1 Results of Local Tissue Deformation

The local deformation of LTD phantom during the needle insertion were quantified as the tissue stain and displacement in DIC. Figure 2-4 shows the distributions of tissue strain within the ROI of 455 × 800 pixels at t = 2.0, 2.2, and 2.4 s for NCD, NCI, and MPI insertions. The Eulerian strain along the x-axis (the needle insertion direction), denoted as E_{xx}, is presented.

In NCD insertion (Fig. 2-4(a)), the needle and cannula were inserted at a constant speed and compressed the tissue in front of the needle. At t = 2.0 s, the E_{xx} in front of the needle tip was about −0.2. As needle continued advancing, the compressive E_{xx} in front of the needle tip was increased to about −0.5 (with two local concentrated peaks) and −0.6 at 2.2 and 2.4 s, respectively. Such nonuniform, stick-slip deformation had been reported in the force measurement of needle insertion at a constant speed [42, 59]. During the insertion, the tissue was compressed to a threshold level and then the cutting occurred. The high compressive strain and force in front of the needle during the insertion pushed the tissue forward, induced the prostate displacement, and decreased the needle targeting accuracy in biopsy (Fig. 2-1(e)). The intermittent cutting and nonuniform deformation created ripples of local concentrated deformation in strain distribution around the needle and cannula surfaces [72]. The E_{xx} around the cannula remained about −0.1 to −0.2 over the entire insertion due to the friction force under the constant insertion speed. Away from the needle, the tissue was generally under the low strain with E_{xx} of about 0.0.

In NCI insertion (Fig. 2-4(b)), at t = 2.0 s, the needle and cannula just finished retracting and advancing, respectively. The compressive strain in front of the needle tip was small (E_{xx} of about −0.1 to −0.15) compared to that in NCD insertion. The strain of tissue around the cannula was rippled with the compressive E_{xx} about −0.3 to −0.4, much larger than that in NCD insertion due to cannula's advancing motion which compressed the tissue. At t = 2.2 s, the needle and cannula just finished advancing and retracting, respectively. The needle tip compressed the tissue to E_{xx} of about −0.35 to −0.45. The tissue around the cannula was in tension with E_{xx} of about 0.1 due to the cannula retraction which pulled and deformed the tissue. Such tissue tension near cannula could balance the tissue compression around the needle tip, stabilizing the surrounding tissue (to be discussed in Fig. 2-5). At t = 2.4 s, the needle and cannula finished retracting and

advancing, respectively, as in t = 2.0 s. The distribution of E_{xx} was also similar to that at t = 2.0 s. The balance of compressive and tensile E_{xx} reduced the overall displacement of the surrounding tissue during the insertion (to be discussed in Fig. 2-5).

In MPI insertion (Fig. 2-4(c)), at t = 2.0 s, the needle and cannula finished retracting and advancing, respectively, as in NCI insertion. Compared to the E_{xx} in NCD and NCI insertions, the tissue compressive strain in front of the needle was even smaller with E_{xx} of about −0.1 because of the notches at the needle tip. The E_{xx} around the cannula had less ripples (likely due to less tissue displacement when compared to NCI insertion) and was reduced to about −0.2 to −0.3. At t = 2.2 s, as in NCI insertion, the needle and cannula finished advancing and retracting, respectively. The strain in front of the needle was also small with E_{xx} of about −0.15 due to the reduced friction force as a result of notches and reduced contact area at the needle tip. Compared to NCI insertion, the E_{xx} of about −0.25 around the cannula was compressive (instead of tensile in NCI) and more uniform. Since the E_{xx} in front of the needle tip was low due to the reduced needle tip friction force, the deformation of tissue was also small. At t = 2.4 s, as in NCI insertion, the needle and cannula finished retracting and advancing, respectively. The E_{xx} of about −0.1 in front of the needle was the smallest among three insertions. The E_{xx} around the cannula was also reduced (compared to that of NCI insertion) to about −0.2 due to notches at the needle tip anchored the tissue during the retraction. Such anchoring balanced the tissue deformation caused by cannula advancement and needle retraction as well as reduced the overall displacement of the surrounding tissue (to be discussed in Fig. 2-5).

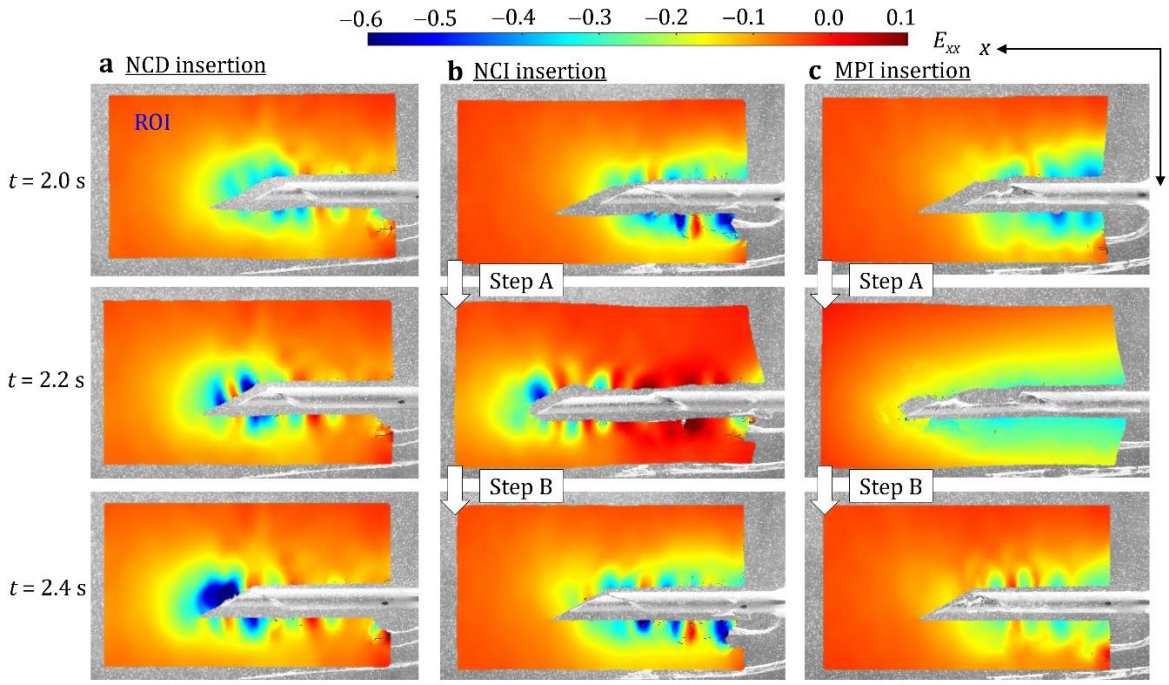

Fig. 2-4 Tissue strain E_{xx} during three insertion motions at t = 2.0, 2.2, and 2.4 s (scale: cannula diameter of 1.27 mm). (a) NCD insertion: the direct insertion motion generated the highly concentrated compressive tissue strain in front of the needle which could induce the prostate displacement. (b) NCI insertion: the opposite motions of needle and cannula reduced the tissue strain in front of the needle and stabilized the surrounding tissue displacement. (c) MPI insertion: the notches at the MPI needle tip provided the critical tissue anchoring to further reduce the overall tissue displacement.

Figure 2-5 shows the tissue displacement and needle insertion force during NCD, NCI, and MPI insertions in three ways. The first is the distribution of tissue displacement (analyzed using the DIC) along the x-axis in the ROI at t = 2.0, 2.2, and 2.4 s. The second is the average overall displacement of the Region A (as illustrated by the dash line enclosures near the needle in Fig. 2-5), denoted as U_A, vs. time during the 2.4 s insertion. The third is the measured insertion force vs. time.

In NCD insertion (Fig. 2-5(a)), the needle and cannula steadily moved forward and deformed the tissue. At t = 2.0 s, the tissue displacement around the cannula was large, about 3 mm, and gradually decayed to about 1.0 mm in front of the needle tip. From t = 2.0 to 2.4 s, the tissue displacement in front of the needle increased from 1.0 to 1.5 mm due to the direct insertion

motion. This caused the U_A to increase from 1.7, 1.9, to 2.1 mm at t = 2.0, 2.2, and 2.4 s, respectively. The needle insertion force also kept increasing from 3.2, 3.3, to 3.5 N at 2.0, 2.2, and 2.4 s, respectively.

In NCI insertion (Fig. 2-5(b)), at t = 2.0 s, the tissue displacement was reduced by about 0.5 mm in front of the needle compared to that in NCD insertion, due to the opposite motions of the needle and cannula. This was also reflected in U_A with 1.3 mm (vs. 1.7 mm in NCD insertion). At t = 2.2 s, the tissue displacement was about 1.5 to 2.0 mm inside Region A with U_A = 1.8 mm (lower than the U_A in NCD insertion). The distribution of tissue displacement was more uniform compared to that in NCD insertion. This was due to the cannula retraction which generated the tissue tension to balance the compression caused by the needle advancement (Fig. 2-4(b)) and stabilize the surrounding tissue. At t = 2.4 s, the tissue displacement was also much smaller, only about 1 mm in front of the needle tip compared to about 1.5 mm in NCD insertion. The U_A was also reduced to 1.5 mm (vs. 2.1 mm in NCD insertion). This was caused by the needle retraction to reduce the tissue deformation caused by the cannula advancement (Fig. 2-4(b)), similar to that at t = 2.2 s. Such opposite motions had resulted the oscillations in U_A during the insertion since the needle advanced more and retracted less to create an incremental advancement. The NCI insertion had a smaller needle insertion force (compared to those in NCD insertion) with 2.4, 2.9, and 3.0 N at 2.0, 2.2, and 2.4 s, respectively.

In MPI insertion (Fig. 2-5(c)), at t = 2.0 s, the distribution of tissue displacement was similar to that in NCI insertion but with a smaller U_A = 1.3 mm (vs. 1.5 mm in NCI insertion) because of the notches at the needle tip. At t = 2.2 s, the tissue displacement was further reduced to about 1.0 to 1.5 mm in Region A (with the U_A = 1.4 mm vs. 1.8 mm in NCD insertion). This was due to the reduced friction force and tissue deformation in front of the needle (Fig. 2-4(c)) as a result of the notches at the needle tip. At t = 2.4 s, the tissue displacement was about 0.5 mm in front of the needle tip, the smallest in comparison to NCD and NCI insertions. The U_A was also the smallest with 1.3 mm (vs. 2.1 and 1.5 mm in NCD and NCI insertions, respectively). The notches at the needle tip provided the critical tissue anchoring to balance the deformation caused by the cannula during the insertion (Fig. 2-4(c)). Such tissue anchoring also led to the smaller amplitude of oscillation of U_A compared to those of NCI insertion. The MPI insertion had the smallest needle insertion forces with 2.4, 2.2, and 2.6 N at 2, 2.2, and 2.4 s, respectively, among three insertions.

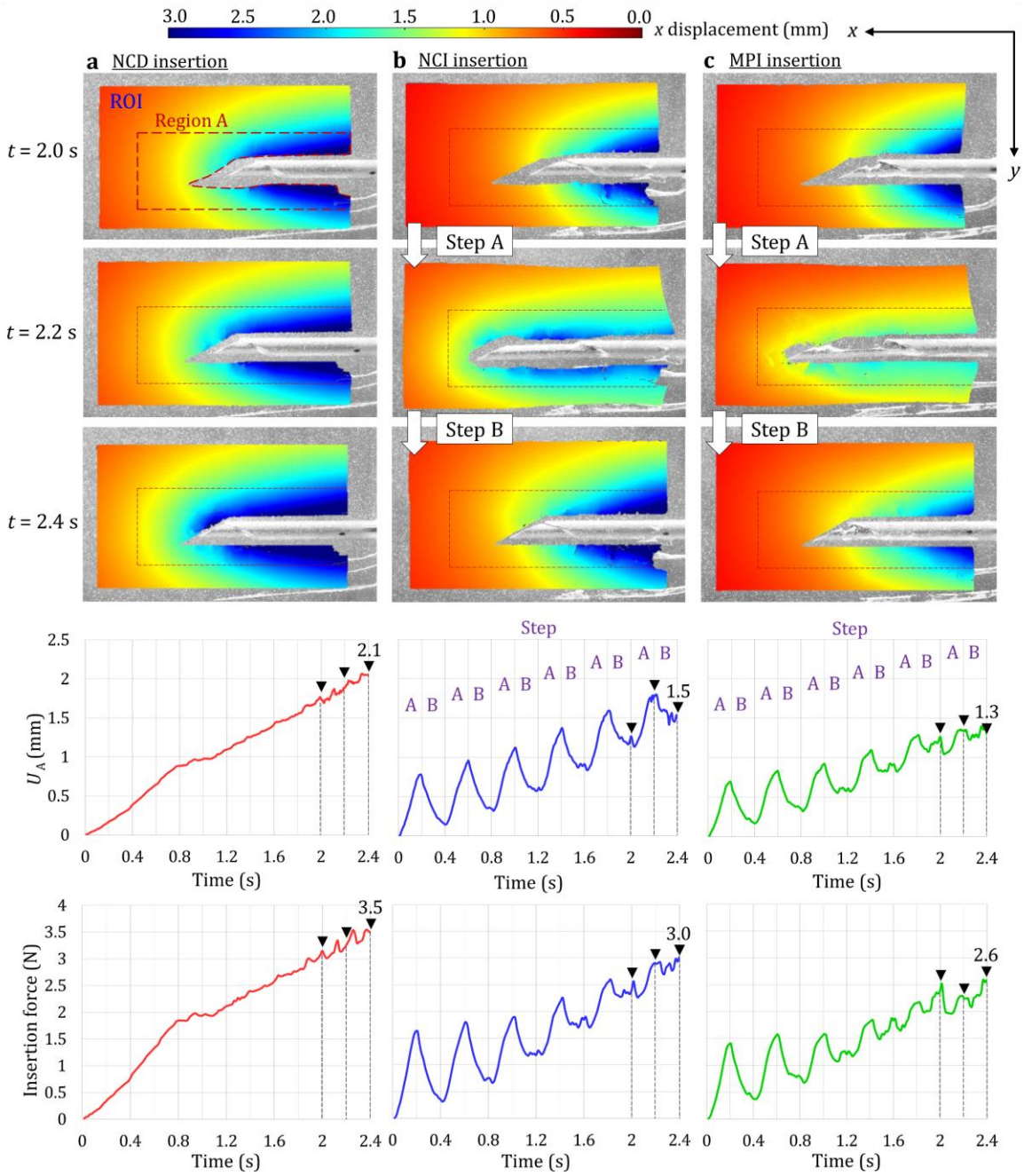

Fig. 2-5 The distribution of tissue displacement, the average overall displacement in Region A (U_A), and the needle insertion force during NCD, NCI, and MPI insertions (scale: cannula diameter of 1.27 mm). (a) NCD insertion: the direct insertion motion induced the largest displacement of surrounding tissue and force during the insertion. (b) NCI insertion: the opposite motions of needle and cannula stabilized and reduced the displacement of surrounding tissue. (c) MPI insertion: notches at the MPI needle tip provided the anchoring to further reduce the overall tissue displacement during insertion.

2.3.2 Results of Global Prostate Displacement

The GPD phantom, as shown in Figs. 2-3(f)-(h), was utilized to track and quantify the global prostate displacement during the needle insertion. As illustrated by the red circles in the inner core of the GPD phantom in Fig. 2-6, 100 trackable points on the particles were automatically identified by the tracking algorithm before the needle insertion. The global prostate displacement U_P was defined as the average of tracking point displacements at a specific time. Figure 2-6 shows the U_P vs. time during the NCD, NCI, and MPI insertions of the top needle path (as illustrated in Fig. 2-3(h)). Three needle tip positions, P_1, P_2, and P_3 (also illustrated in Fig. 2-3(g)) were defined as positions of the needle tip at the edge of outer layer, edge of the inner core, and end of the needle insertion, respectively.

In NCD insertion, the U_P continued increasing with time until the slight drop near the end of the insertion (9.4 s) due to the slipping of tissue on the needle and cannula to cause the change in displacement. The U_p is equal to 0.6, 1.0, to 2.2 mm at P_1, P_2, and P_3, respectively. This increasing of U_P matched to the trend of steadily increasing U_A in Fig. 2-5(a).

In NCI insertion, the U_P was 0.4, 0.7, to 1.8 mm (lower than the 0.6, 1.0, and 2.2 mm in NCD insertion) at P_1, P_2, and P_3, respectively, due to the opposite needle-cannula motions during the insertion. Such opposite motions also caused the oscillations of U_P (also observed in U_A in Fig. 2-5(b)). At the beginning of the insertion (less than 1.3 s), the U_P was larger than that of NCD insertion due to the unsteady tissue deformation. After 1.3 s, the opposite needle-cannula motions reduced the U_P in comparison to that in NCD insertion.

In MPI insertion, the U_P was further reduced compared to that of NCI insertion because the notches at the needle tip anchored the tissue to balance the deformation caused by cannula's friction force. The U_P of 1.5 mm at P_3 (vs. 2.2 and 1.8 mm in NCD and NCI insertions, respectively) was the smallest. The notches and tissue anchoring also reduced the amplitude of oscillation of U_P during the MPI insertion.

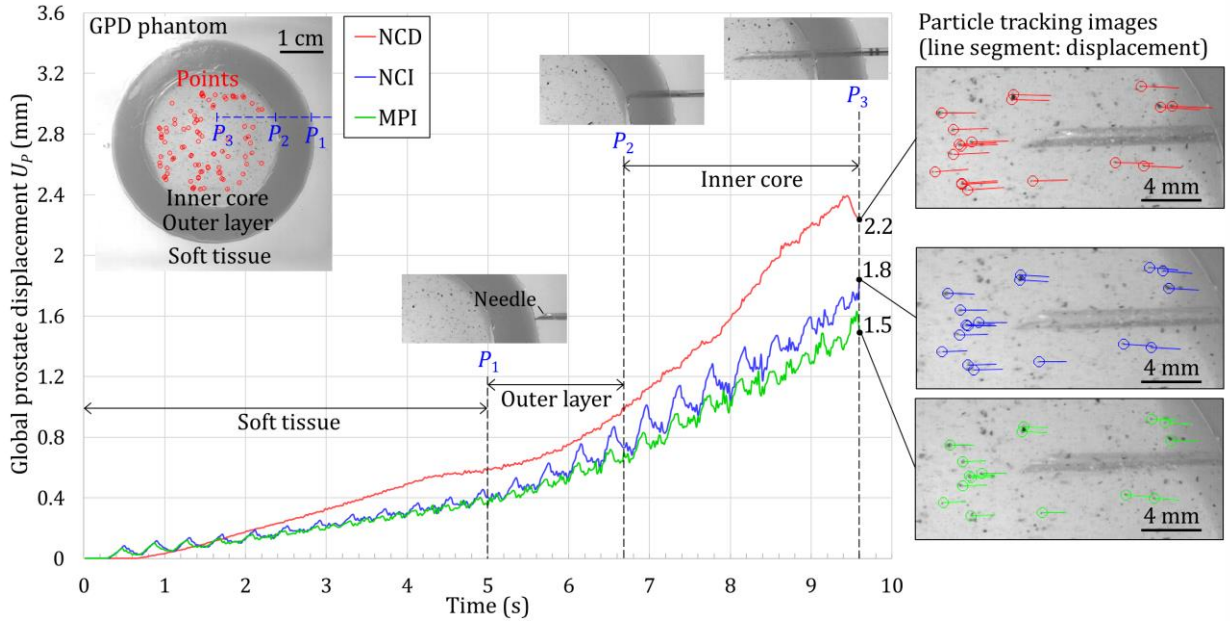

Fig. 2-6 The global prostate displacement U_P vs. time during NCD, NCI, and MPI insertions in the top path. The NCD insertion continued increasing the U_P until the slight drop near the end of the insertion due to the direct insertion motion. The NCI insertion reduced the U_P by the opposite needle-cannula motions. The MPI insertion had the smallest U_P since the notches at the tip provided the tissue anchoring. Images in the particle tracking analysis at the end of each insertion were also shown with line segments representing the tracking point displacement.

Figure 2-7 summarizes the histogram of tracking point displacements at the end of the NCD, NCI, and MPI needle insertions with the top, middle, bottom paths (illustrated in Fig. 2-3(h)). For these 9 insertion tests, the average and standard deviation of the tracking point displacements are presented. The average of tracking point displacements is equal to U_P. The NCD direct insertion motion had the largest U_P of 2.2, 2.5, and 2.1 mm in the top, middle, and bottom paths, respectively. The NCI insertion (with the opposite needle-cannula motion) reduced the U_P to 1.8, 1.7, and 1.6 mm in the top, middle, and bottom paths, respectively. With the notches at the needle tip, the MPI insertion had the smallest U_P of 1.5, 1.3, and 1.4 mm in the top, middle, and bottom paths, respectively.

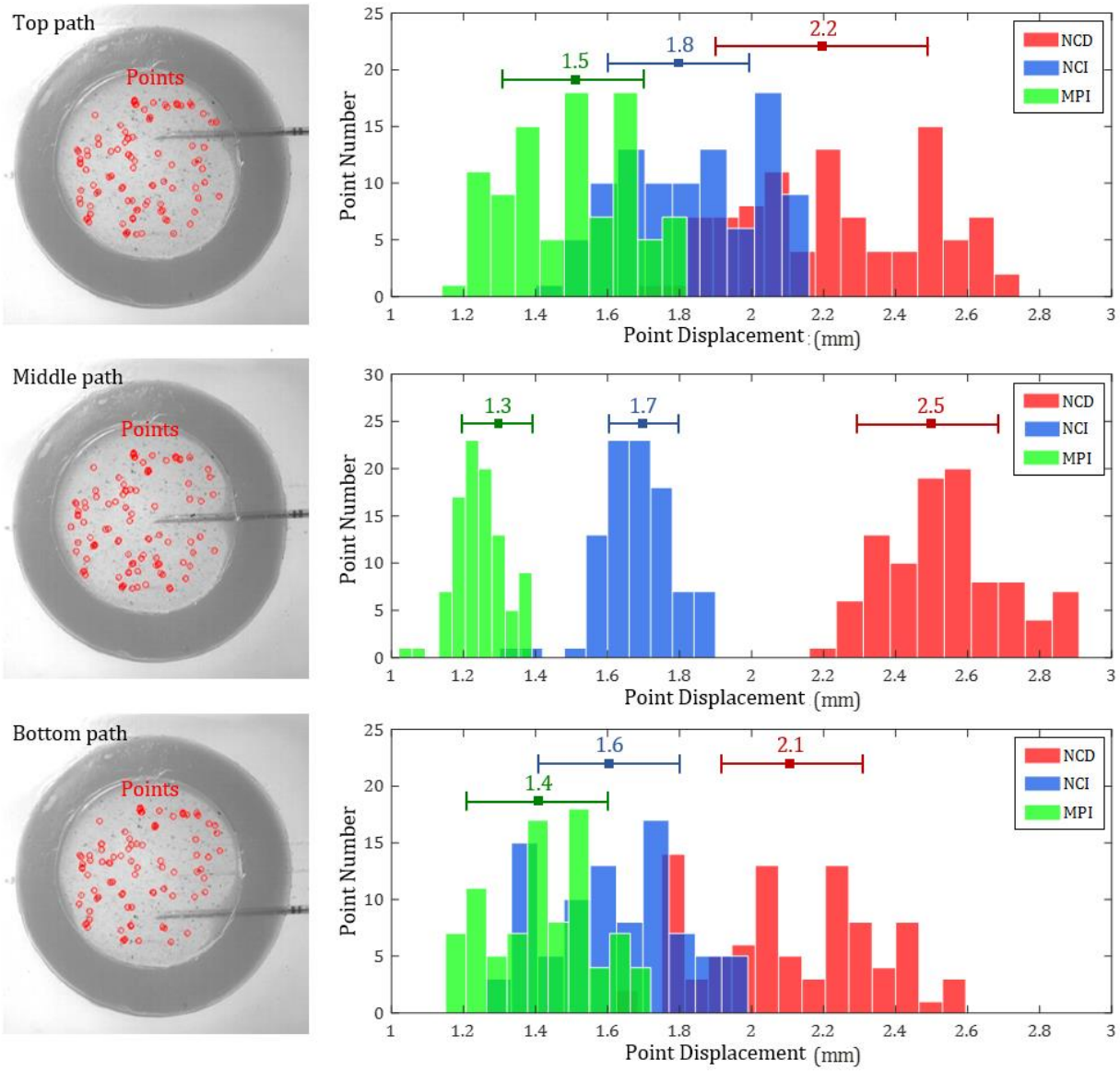

Fig. 2-7 The histogram of tracking point displacements at the end of the NCD, NCI, and MPI insertions in the top, middle, bottom needle paths. The average (U_P) and standard deviation of the tracking point displacement are shown at the top of the histogram. For all three insertion paths, the NCD insertion had the largest U_P, the NCI insertion had the reduced U_P compared to NCD insertion, and the MPI insertion had the smallest U_P.

2.4 Discussions

This study investigated the local tissue deformation and global prostate displacement, quantified as U_A and U_P, respectively, during NCD, NCI, and MPI insertions. The opposite needle-cannula motions (mimicking mosquito proboscis's insertion [60–62]) in NCI and MPI insertions reduced the U_A and U_P compared to those of NCD insertion. The incremental advancements of needle and cannula first generated the vibratory insertion as that of mosquito proboscis for easier penetration into the soft tissue [63]. The cannula/needle retraction further created the opposite force to reduce the tissue deformation caused by the needle/cannula advancement during the incremental insertion. The tissue and organ displacement could also be stabilized and reduced [38, 63]. The harpoon-shape notches at the needle tip (mimicking mosquito proboscis's notches [60, 64]) in MPI insertion had resulted the smallest U_A and U_P among three insertions with up to 38% and 48% reduction in U_A and U_P, respectively, when compared to NCD insertion. During the needle advancement, the notches reduced the contact area (compared to that of the needle without the notches) and resulted in a low friction force [68] which reduced the tissue deformation (compared to that of NCI insertion). When needle retracted, the notches were able to anchor the tissue during the opposite needle-cannula motion [60, 64] to further reduce the overall displacements of surrounding tissue and prostate. The NCD insertion generated the largest U_A and U_P due to the direct insertion motion which significantly deformed the surrounding tissue (in the local scale) and pushed the prostate forward (in the global scale). Such deformation and displacement could cause the tissue sampling errors shown in Figs. 2-1(d) and (e) and decrease the accuracy of cancer diagnostic in needle biopsy [23, 25, 29, 33].

In summary, needle insertion motion has a strong influence on deformation and displacement of soft tissues. The effectiveness of MPI insertion in reducing the surrounding tissue deformation and organ displacement in needle biopsy has been demonstrated. Future work will focus on implementing MPI insertion into current hand-held biopsy device. Mechanical-driven mechanism to generate the incremental motion will be investigated to enhance the feasibility of MPI insertion for clinical use. Findings here also provide the insights of needle-tissue interaction during needle insertion which can guide the researchers to develop the technology to improve the needle deployment accuracy in biopsy as well as other clinical procedures requiring accurate needle guidance.

Chapter 3: Needle Deflection and Tissue Sampling Length in Needle Biopsy

3.1 Introduction

Needle deflection is one of the major issues affecting needle biopsy performance [23, 25]. As discussed in Section 1.1, such needle deflection in high-speed firing of biopsy (Phase II) reduces needle deployment accuracy to the targeted diseased tissue site, potentially affecting cancer diagnostic accuracy [27, 28]. Needle deflection is due to the cutting force, tip force, tissue pressure, and friction force creating the unbalanced moments which bend the needle as shown in Fig. 3-1(a). The cutting force is generated at the needle tip point A, where tissue is cut and separated (as illustrated by the red arrows in Fig. 3-1(a)). The separated tissue contacts the bevel face of the needle tip and creates a downward face force, inducing needle deflection [25]. The needle-tissue interaction also generates a distributed tissue pressure (acting on regions of direct contact between tissue and needle) and friction force on the needle, which can further aggravate the deflection (Fig. 3-1(a)). Such deflection can cause the needle to miss or undersample (failing to sample the lesion center) the targeted lesion as shown in Fig. 3-1(b). Since prostate lesions tend to be heterogeneous with more aggressive cancer cells at the lesion center [26], such sampling errors can have clinical impacts such as false-negative and cancer misdiagnosis [27, 28].

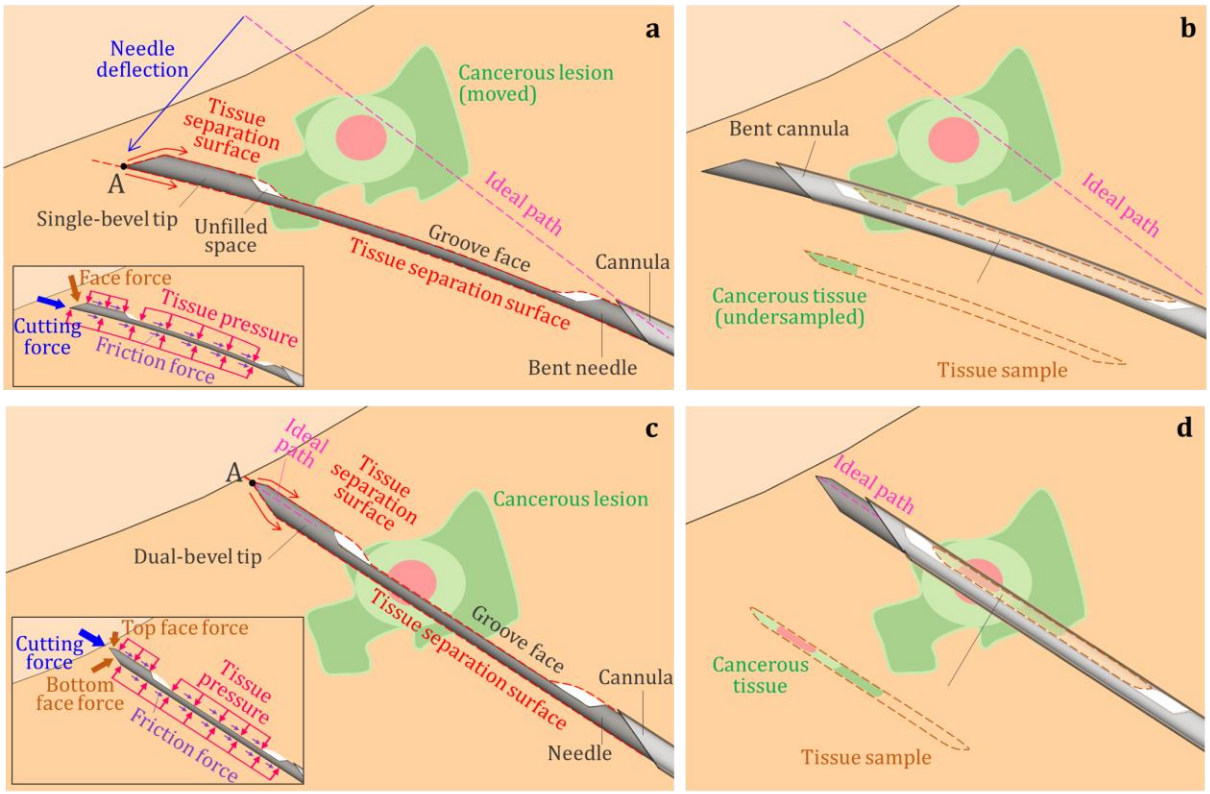

Fig. 3-1 Needle deflection in biopsy procedure: (a) the needle deflection, tissue separation surfaces initiated at the needle tip point A, and the cutting force, face force, tissue pressure, and friction force acting on the needle during insertion, (b) undersampled cancerous tissue due to needle deflection, (c) the dual-bevel needle tip improving the force and moment balance to reduce needle deflection during insertion, and (d) accurate tissue sampling with a more predictable and straight needle insertion path to sample the cancerous lesion center.

This study investigates multi-bevel needle tip geometries to balance the bending moments, reduce the needle deflection, and enable a more predictable and straight insertion path in trucut biopsy. For example, Fig. 3-1(c) shows a dual-bevel needle with two bevel faces at the needle tip generating top and bottom face forces. The bottom face force is designed to be larger than the top face force to balance the bending moments created by the insertion forces, thereby reducing needle deflection. The goal of this study is to utilize the needle tip geometry to improve the force balance and resulting bending moment, allowing the needle to accurately sample the targeted lesion in biopsy, as illustrated in Fig. 3-1(d).

Besides needle sampling accuracy, the tissue sampling length in needle biopsy is also critical for pathological analysis [42]. Research on the tissue sampling length in trucut needle biopsy is limited. During needle biopsy, the tissue in front of the needle tip is separated at tip point A into two separation surfaces marked in Figs. 3-1(a) and (c). The top tissue after separation is compressed and then rebounds once it reaches the open needle groove. The tissue that fills inside the groove is then cut by the outer cannula and sampled for biopsy. In this study, the location of the tip point A relative to the groove face as illustrated in Figs. 3-1(a) and (c) is identified as a key factor affecting the amount of tissue filled inside the groove. The effect of needle tip location on tissue sampling length is explored in this study.

In this chapter, four trucut needle tip geometries (single-, dual-, vertical-, and asymmetric multi-bevel) are investigated. A coupled Eulerian-Lagrangian model for needle-tissue interaction is utilized to gain insights of tissue deformation, separation, and contact inside the needle groove. Multilayered tissue-mimicking phantoms are used to study needle deflection. Trucut needle biopsies of ex-vivo tissue are conducted to identify the relationship between needle tip geometry and tissue sampling length.

3.2 Materials and Methods

The needle tip geometry, needle flexural rigidity, coupled Eulerian-Lagrangian finite element analysis of needle-tissue interaction, needle deflection experimental setup, multilayered tissue-mimicking phantoms, ex-vivo tissue sampling length, and statistical analysis are presented.

3.2.1 Needle Tip Geometry

Four trucut needle tip geometries, denoted as single-bevel (SB), dual-bevel (DB), vertical-bevel (VB), and asymmetric multi-bevel (AMB) needles, as shown in Figs. 3-2(a), (b), (c), and (d), respectively, are studied. The needle tip cutting point A (for SB needle) or cutting edge AB (for DB, VB, and AMB needles) initiates the top and bottom tissue separation surfaces during insertion. The needle tip geometry can be defined by four parameters. The first parameter is the bevel angle ξ, as shown in Figs. 3-2(a)-(d). The second parameter is the distance from the tip point

A to the needle groove face d_a, as shown in Fig. 3-2(e). The d_a determines the tissue separation location relative to the groove face. Positive d_a (Figs. 3-2(b)-(d)) means the tissue separation point is above the groove face and less tissue will be inside the groove for biopsy. Conversely, negative d_a (Fig 3-2(a)) means the tissue separation surface is below the groove face with which allow the tissue to contact most of the groove during biopsy while generating the pressure on the groove face contributing to needle bending. The third parameter is the distance from the tip point A to the top edge of the needle, marked as d_t in Fig. 3-2. The fourth parameter is the distance from the tip point B to the bottom edge of the needle, denoted as d_b in Fig. 3-2. Both d_t and d_b are positive.

Details of the SB, DB, VB, and AMB needle tip geometries and the resulting insertion force components are as follows:

- SB needle: As shown in Fig. 3-2(a), the SB needle has a single-bevel face on the same side of the needle groove. The tip point A is below the groove face ($d_a < 0$). The downward face force is denoted as F_f, which bends and deflects the needle during insertion (Fig. 3-1(d)).
- DB needle: The DB needle has the top and bottom bevel faces with F_{tf} and F_{bf} face forces, respectively, as shown in Fig. 3-2(b). The tip point A is above the groove face ($d_a > 0$). The needle tip is designed to have the d_b larger than d_t; therefore, F_{bf} is larger than F_{tf} to balance the bending moment created by tissue pressure on the groove face (Fig. 3-1(f)), reducing the needle deflection during insertion.
- VB needle: The VB needle has two symmetric vertical bevel faces. As shown in Fig. 3-2(c), the cutting edge AB is perpendicular to the groove face to separate the tissue laterally. The VB needle has the tip point A above the groove face ($d_a > 0$). Due to this vertical symmetry, two lateral face forces F_{fl} at the needle tip can balance each other during insertion.
- AMB needle: The DB and VB needles are combined to form the AMB needle with four asymmetric bevel faces shown in Fig. 3-2(d). The tip point A is above the groove face ($d_a > 0$). In addition to two balanced lateral face forces F_{fl}, the AMB needle has two other forces F_{tf} and F_{bf}. Like the DB needle, the AMB needle has the d_b larger than d_t ($F_{tf} < F_{bf}$) to balance the bending moment caused by the tissue pressure on the groove face.

In this study, four needle tips were fabricated using the 18-gauge (1 mm diameter) AISI 316 stainless steel rods. All four needles have the same $\xi = 22°$. The SB needle has $d_a = -0.5$ mm.

The DB needle has d_a = 0.22 mm, d_t = 0.28 mm, and d_b = 0.72 mm. The VB needle has d_a = 0.5 mm. The AMB needle has d_a = 0.32 mm, d_t = 0.18 mm, and d_b = 0.3 mm. The optical microscopy images of four needles are shown in Fig. 3-2.

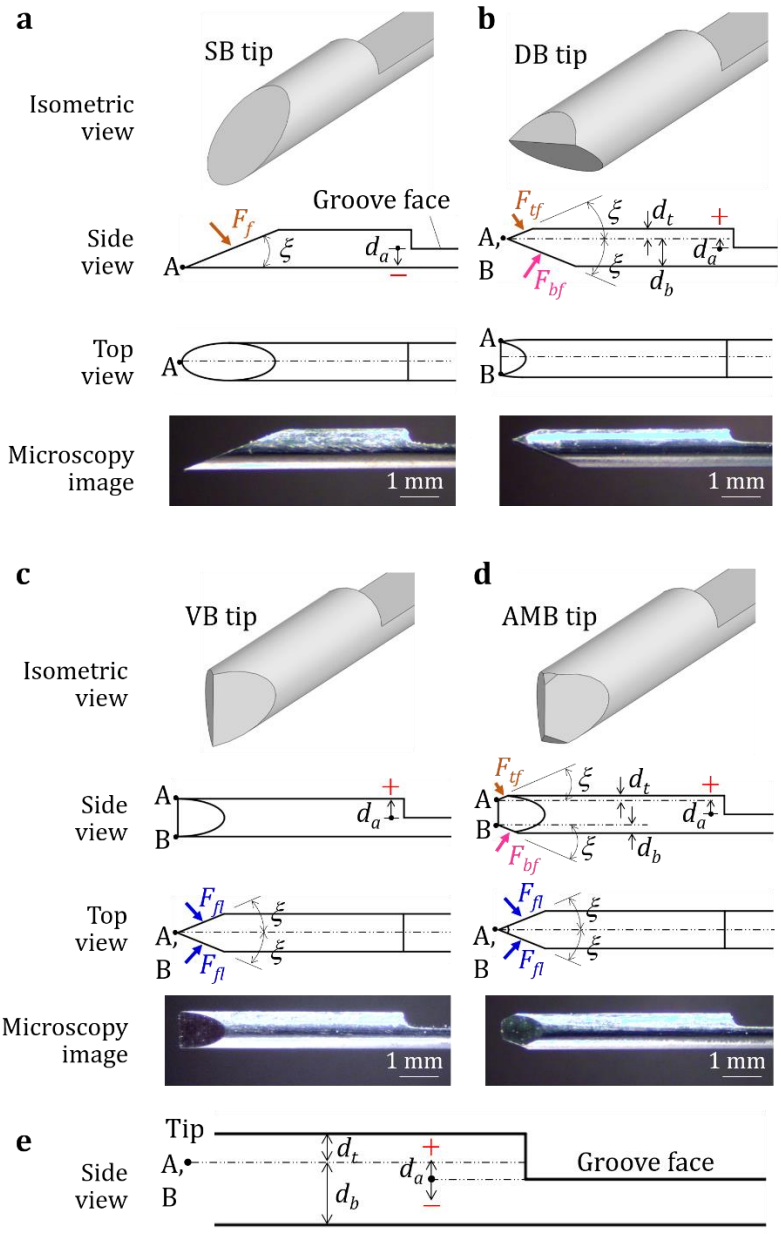

Fig. 3-2 The needle tip geometry, tip force diagram and microscopy image of the 18-gauge (a) SB, (b) DB, (c) VB, and (d) AMB needles and (e) the schematic diagram to define d_a, d_t, and d_b.

3.2.2 Needle Flexural Rigidity

The needle deflection is commonly modeled as a cantilever beam in bending [25] and analyzed using the Euler–Bernoulli beam bending equation $\partial^2 y(x)/\partial x^2 = -M(x)/EI$, where x is the position along the needle length, $y(x)$ is the needle deflection at position x, $M(x)$ is the bending moment, E is the Young's modulus, and I is the second moment of area of the needle cross-section. The flexural rigidity of the needle is defined as EI, which is the stiffness of the needle against bending due to insertion forces. The I is calculated based on the needle cross-section geometry.

Figure 3-3(a) shows the side and cross-sectional views of the needle. The length between the needle tip (point A) and the front side of the groove is d_{tg}. The groove has length l_g and depth d_g. The groove reduces the I and decreases the stiffness against bending. The I of the needle cross-section in the groove is calculated as:

$$I = r^4 \left(\frac{\theta - \sin\theta + 2\sin^2\frac{\theta}{2}\sin\theta}{8} - \frac{8r^4 \sin^6\frac{\theta}{2}}{9(\theta - \sin\theta)} \right) \tag{1}$$

$$\begin{aligned} \theta &= 2\cos^{-1}\left(\frac{r-h}{r}\right) && \text{when } h \le r \\ \theta &= 2\left(\pi - \cos^{-1}\left(\frac{h-r}{r}\right)\right) && \text{when } h > r \end{aligned} \tag{2}$$

where θ is the central angle of the circular segment, r is the needle radius, and h is the height of the circular segment, as shown in the cross-section C-C in Fig. 3-3(a). For the groove of the 18-gauge needle used in this study with r = 0.5 mm, d_{tg} = 6 mm, l_g = 18 mm, and d_g = 0.5 mm (Fig. 3-3(b)), h = 0.5 mm, and $\theta = \pi$. Based on Eq. (1), I = 0.0069 mm^4. In comparison, the I = 0.049 mm^4 in the cylindrical needle body (cross-section D-D), which is 7 times larger than the I in the groove. The groove with low stiffness is vulnerable for bending during insertion.

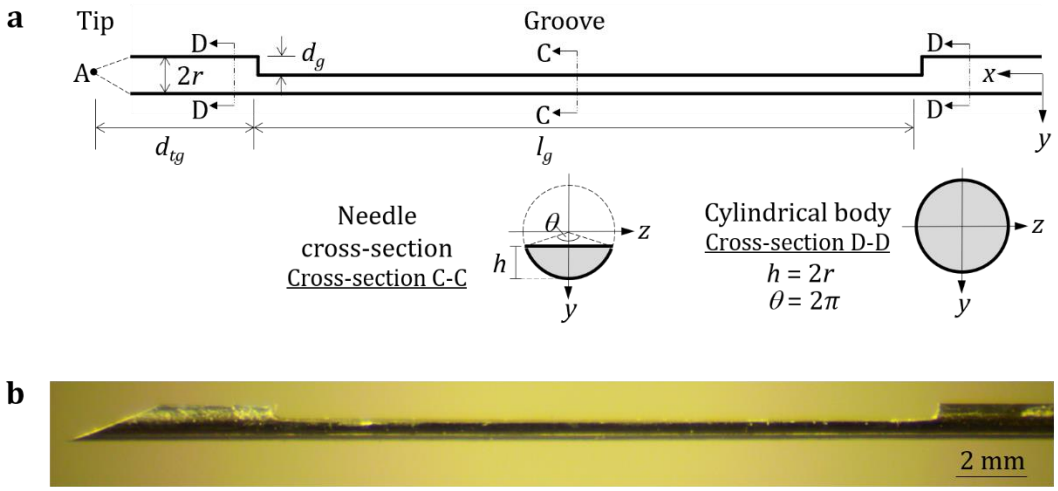

Fig. 3-3 (a) The needle cross-sections and (b) the side view of the biopsy needle in this study (r = 0.5 mm, d_{tg} = 6 mm, l_g = 18 mm, and d_g = 0.5 mm).The needle deflection is commonly modeled as a cantilever beam in bending [25] and analyzed using the Euler–Bernoulli beam bending equation

3.2.3 Coupled Eulerian-Lagrangian (CEL) Finite Element Analysis (FEA) of Needle-Tissue Interaction

This study develops a 3D CEL FEA model of needle-tissue interaction to qualitatively investigate the tissue deformation, separation surfaces, and contact inside the groove during needle insertion in biopsy. Prior researches on needle-tissue interaction modeling utilized the Lagrangian FEA, in which the tissue separation was modeled using the cohesive zone (CZ) with pre-defined element separation path [40, 50]. However, the tissue separation path is difficult to accurately pre-define in biopsy needle insertion with deflection. Furthermore, the large tissue deformation and mesh distortion at the needle tip have limited the accuracy of the CZ using the Lagrangian FEA approach.

To overcome the above limitations, this study utilized the CEL FEA [78, 79] to model the motion of a rigid needle and the deformation of soft tissue by the Lagrangian and Eulerian analysis, respectively. In CEL, the Lagrangian analysis of the rigid needle was used to precisely define the needle-tissue boundary during insertion. The coupled Eulerian analysis of the soft tissue had fixed mesh allowing the tissue to freely move within elements. This technique can avoid the mesh

distortion and effectively simulate the tissue deformation and separation during needle insertion [78, 79].

The 3D CEL FEA model of the SB needle insertion (as an example) into the soft tissue based on Abaqus Explicit (v 6.11 by Dassault Systèmes, Vélizy-Villacoublay, France) developed in this study is shown in Fig. 3-4. Due to the symmetry of the geometry, only half of the needle and tissue were modeled. An isometric view from the symmetric plane LKST is shown in Fig. 3-4(a). The soft tissue and void regions were modeled by 3D Eulerian elements as cuboids MNOPQRST and IJKLMNOP, respectively, before the needle insertion as shown in Fig. 3-4(a). The MNOPQRST region (30 mm × 3 mm × 6 mm) was the initial undeformed tissue before needle insertion. The IJKLMNOP was the void region (5 mm × 3 mm × 6 mm) to accommodate the deformed tissue (expansion of the tissue region) during needle insertion [78, 79]. The tissue and void regions were meshed using the 8-node linear cubical element (EC3D8R in Abaqus) with 0.09 mm element edge length, as shown in Figs. 3-4(b) and (c). The symmetric plane LKST was constrained in the *z*-axis while allowing deformation within the *xy* plane, as shown in Fig. 3-4(c). The surface MNOP (surface of the tissue where the needle tip touched before the insertion) was set as a free surface allowing the deformation in all three (*xyz*) directions. Outer boundary surfaces ILTQ, JKSR, IJRQ, and QRST were fixed in all three (*xyz*) directions, as shown in Figs. 3-4(b) and (c). The elastic modulus E, Poisson's ratio ν, and density ρ of the tissue was 21.3 kPa, 0.45, and 0.98 g/cm^3, respectively, based on the composition of the polyvinyl chloride (PVC) tissue-mimicking phantom used in this study to simulate the healthy prostate tissue [70, 71]. Details of tissue-mimicking phantoms are presented in Sec. 3.2.5.

Four needles (SB, DB, VB, and AMB shown in Fig. 3-2) were modeled using Lagrangian elements. The needle was positioned with the tip (point A or line BC shown in Fig. 3-2) on line PO, as shown in Fig. 3-4(a), before insertion. The needle geometry (Fig. 3-3) was defined with the radius r = 0.5 mm, distance between the needle tip and the groove opening d_{tg} = 6 mm, groove length l_g = 18 mm, and groove depth d_g = 0.5 mm. In this CEL model, the needle length l_n is 40 mm, as shown in Fig. 3-4(a). The needle was meshed using the 10-node quadratic tetrahedron elements (C3D10M in Abaqus) as shown in Figs. 3-4(b) and (c) to define its shape in CEL. The meshing algorithm with the initial mesh size of 0.3 mm element edge length in Abaqus was applied to generate the needle mesh. Figure 3-4(d) shows the isometric view of the needle mesh. The meshes in the regions around the sharp needle tip and the groove edges were automatically refined

to accurately represent the needle geometry as the close-up view shown in Fig. 3-4(d). The needle insertion motion was defined to have 25 mm travel with a constant acceleration of 1333 m/s^2 within 0.006 s based on the motion of the needle biopsy device observed by the high-speed camera (details to be presented in Sec. 3.2.4).

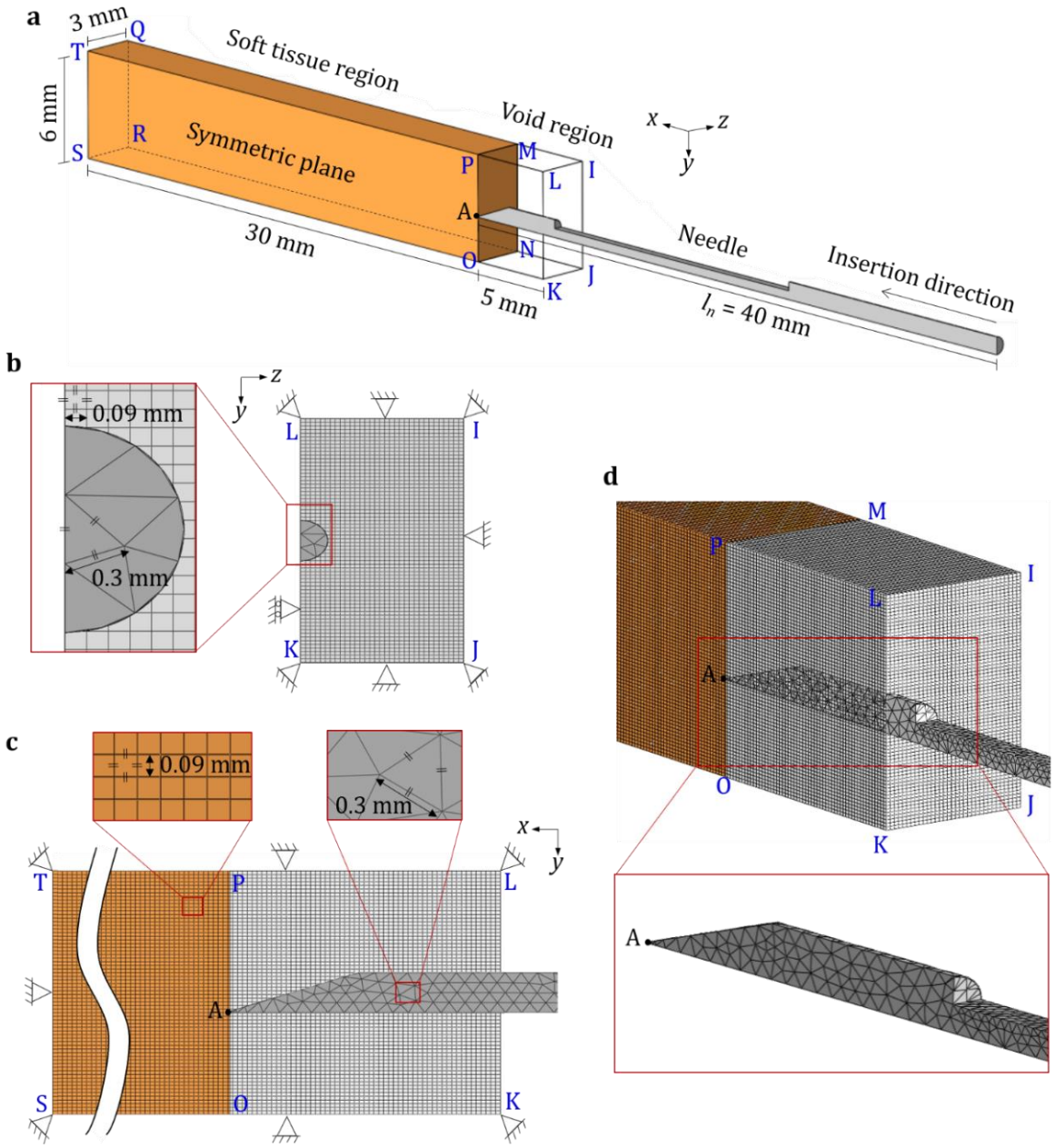

Fig. 3-4 An overview of a 3D CEL FEA of needle-tissue interaction: (a) an isometric view of the SB needle insertion to the soft tissue and the (b) front (*yz* plane), (c) side (*xy* plane), and (d) isometric views of the CEL needle and tissue meshes.

A friction coefficient μ was used at the contact between the needle and the tissue in CEL analysis. The μ was defined as $\sigma_{fi} / \sigma_{Ni}$, where σ_{fi} and σ_{Ni} are the shear and normal stresses on the needle surface, respectively [59]. The shear stress σ_{fi} was defined by $\sigma_{fi} = f_{fi} / P$, where f_{fi} is the friction force per unit length and P is the needle perimeter [59]. For the soft PVC with the 0.33 ratio of the softener to PVC and 5% mineral oil used in this study, f_{fi} was 0.022 N/mm [70]. The P was 3.14 mm for the 1 mm diameter needle. Therefore, σ_{fi} was 6.9 kPa. The normal stress σ_{Ni} can be estimated based on the method developed to estimate σ_{Ni} in the core needle biopsy where the tissue was compressed into a hollow needle [59]. In this study, the σ_{Ni} was estimated as the stress required to expand the tissue in the radial direction from the needle centerline to the outside diameter. In this case, $\sigma_{Ni} = E / (1-\nu)$ [59], where E and ν are the elastic modulus and Poisson's ratio of the tissue, respectively. For the PVC used in this CEL model with E = 21.3 kPa and ν = 0.45, the normal stress σ_{Ni} was 38.5 kPa. Based on σ_{fi} = 6.9 kPa and σ_{Ni} =38.5 kPa, the friction coefficient μ used in the CEL model of this study was 0.18.

3.2.4 Needle Deflection Experimental Setup

The needle deflection experimental setup is shown in Figs. 3-5(a) and (b). A commercial spring-loaded needle biopsy device (Pro-Mag Ultra Reusable Automatic Biopsy Instrument by Argon Medical Devices, Frisco, Texas, USA) was used as the actuator for needle insertion. The outer cannula was removed in this experiment to allow for better observation of the needle deflection. The needle was installed onto the biopsy device and supported by a biopsy guide (Endfire Biopsy Guide by BK Medical, Peabody, Massachusetts, USA) which has a plastic semi-cylindrical body for the ultrasound probe guide and a metal tube for the needle guide (Fig. 3-5(a)) in prostate biopsy. The needle guide, fixed during needle insertion, positioned the needle to the initial insertion point and supported the needle to prevent buckling during insertion. In the experiment, the needle guide was used to place the needle at the surface of a transparent multilayered tissue-mimicking phantom (details to be presented in Sec. 3.2.5) for insertion. A high-speed camera (Model 100K by Photron, San Diego, California, USA) with 1024×1024 pixel resolution and a 5.6× magnification was used to capture the images of needle tip before and after the insertion to quantify the needle deflection.

To identify the baseline tip position without deflection, the needle was first inserted without the phantom. An example is using the SB needle in Fig. 3-5(c). The needle was then inserted by the biopsy device into the multilayered phantom as shown in Fig. 3-5(d). The needle deflection δ was defined as the vertical distance (relative to the insertion direction) between the final tip location with and without phantom. Ten insertions were performed for each of the four needle tip types (SB, VB, VB, and AMB) at different locations of the phantom. In total, 40 needle insertion tests were performed. The images were analyzed using Matlab (by MathWorks, Natick, Massachusetts, USA) to find the needle tip locations and deflections.

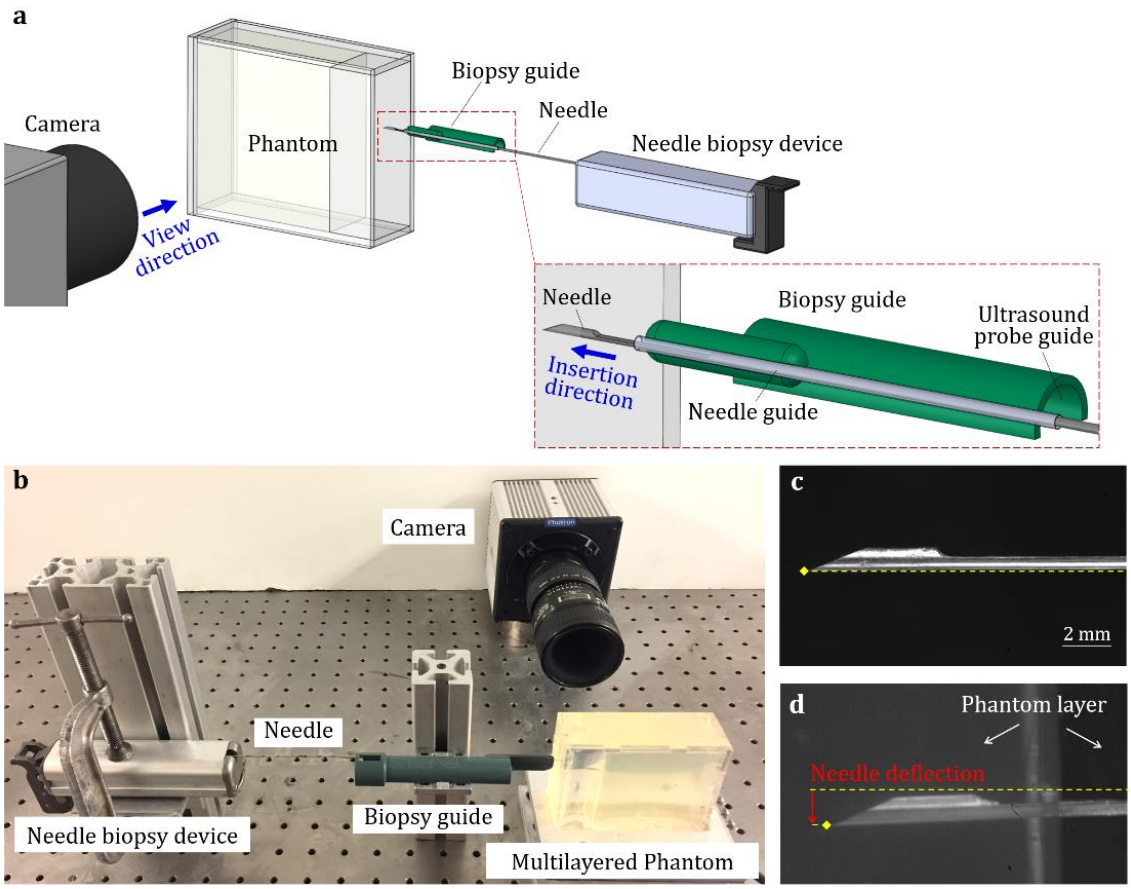

Fig. 3-5 (a) An overview of the needle deflection experiment, (b) the experimental setup, and images of the SB needle tip at the end of the insertion (c) without and (d) with the multilayered phantom.

3.2.5 Multilayered Tissue-Mimicking Phantoms

To mimic prostate tissues, which can have multiple tissue layers with different stiffness, two different multilayer tissue-mimicking phantoms were used in this study. The first phantom was composed of two PVC layers, as shown in Fig. 3-6(a). The outer layer was softer than the inner layer in the phantom to mimic the prostate with the inner hard core and outer soft layer. PVC is a tissue-mimicking material and can be fabricated with the hardness and needle insertion properties similar to prostate tissues [70, 71]. In this study, the softener, PVC polymer (both by M-F Manufacturing, Ft. Worth, Texas, USA), and mineral oil (by W.S. Dodge Oil, Maywood, California, USA) were blended together to create the final phantom materials. The mineral oil was 5% of the total weight and the ratio of the softener to PVC was 0.33 and 0 to fabricate the soft and hard layers of the phantom with 21.3 and 41.7 kPa elastic modulus (both within the range measured by elastography ultrasound of the inner and hard core of healthy prostate [73, 74]), respectively. The width was 30 mm, height was 80 mm, and depth was 25 and 75 mm for the outer and inner layers, respectively, of the two-layer PVC phantom in Fig. 3-6(a). Both PVC layers were transparent, allowing the needle tip to be visible by the camera for deflection measurement.

In needle insertion experiment of the two-layer phantom, the needle was first positioned to the starting point P_s with distance L_i from the tip to the outer layer, as shown in Fig. 3-6(b). In this experiment, L_i = 6 mm. The mechanical spring of the biopsy device was then activated to insert the needle forward by a distance L. In this study, L = 25 mm and the time duration for needle to travel this distance was 0.006 s (4 m/s average insertion speed). The needle tip penetrated the inner layer and stopped at the point P_e shown in Fig. 3-6(b) to mimic the needle penetrating through the outer layer into the stiffer inner region of the prostate. This stiffer inner region, which typically formed in a larger prostate, is considered by urologists as the cause of significant needle deflection in clinical prostate biopsy [23]. A photo of the needle inserted into the two-layer phantom at the end of the insertion is shown in Fig. 3-6(c).

The second phantom has three layers with an ex-vivo porcine tissue layer embedded between two soft PVC layers as shown in Fig. 3-6(d). The ex-vivo porcine tissue with fibrous structure was harder than the surrounding soft PVC layers. This phantom evaluates the needle deflection in the ex-vivo tissue weakly supported within two soft PVC layers, similar to the prostate which is weakly supported by the surrounding soft tissue. The width is 30 mm, height is

80 mm, and depth is 20, 20, and 60 mm for the outer PVC, middle ex-vivo porcine tissue, and inner PVC layers, respectively, of the three-layer phantom, shown in Fig. 3-6(d).

In needle insertion experiment of the three-layer phantom, the needle was first positioned to the starting point P_s with distance L_i from the tip to the outer layer as shown in Fig. 3-6(e). In this experiment, L_i = 20 mm with the needle tip aligned with the boundary of ex-vivo tissue. The needle was then inserted using the same biopsy device (L = 25 mm and 0.006 s traveling time). The needle tip penetrated through the tissue and stopped at point P_e about 5 mm beyond the ex-vivo tissue into the inner PVC layer, allowing the needle tip to be visible by the camera for deflection measurement as shown in Fig. 3-6(f).

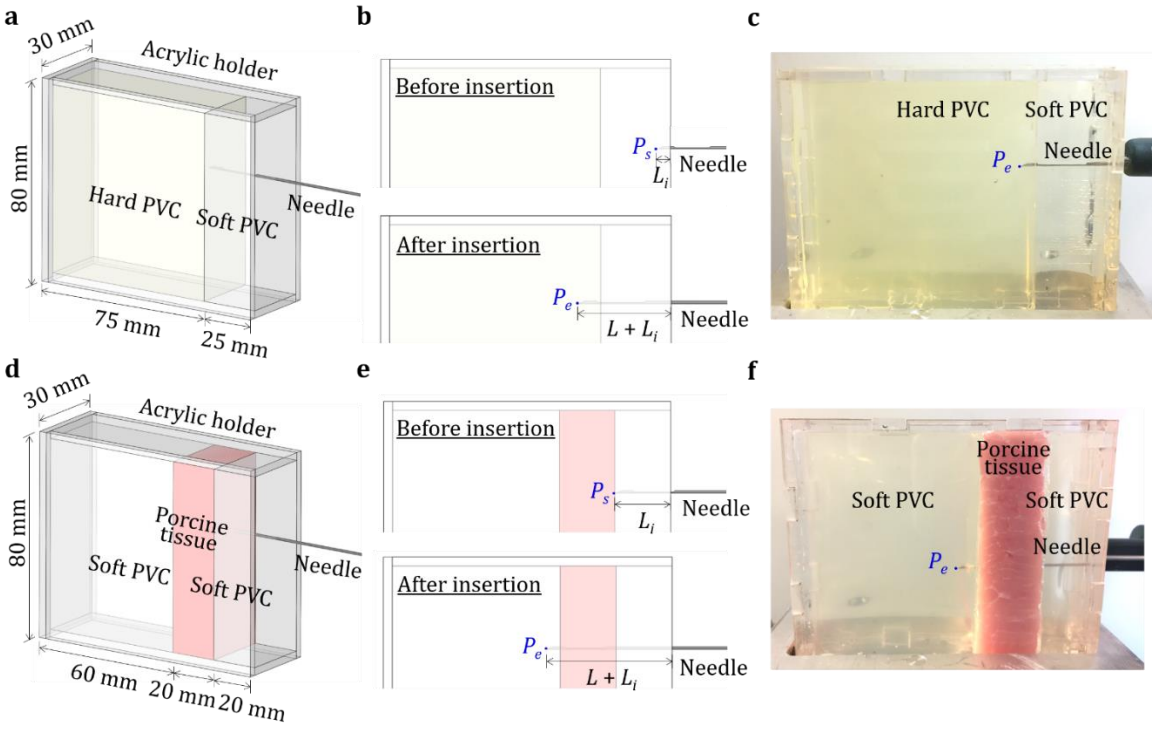

Fig. 3-6 Multilayered tissue-mimicking phantoms: (a) the two-layer phantom with outer soft and inner hard PVC layers, (b) needle positions before and after insertion into the two-layer phantom, (c) photo of needle at the end of insertion in the two-layer phantom, (d) the three-layer phantom with an ex-vivo porcine tissue layer between two soft PVC layers, (e) needle positions before and after the insertion into the three-layer phantom, and (f) photo of the needle at the end of insertion in the three-layer phantom.

3.2.6 Ex-vivo Tissue Sampling Length

The tissue sampling lengths of four needle tip types (SB, DB, VB, and AMB) were measured in experiments of trucut needle biopsy of ex-vivo porcine tissue. The experimental setup is shown in Fig. 3-7(a). The needle and the outer cannula were sequentially inserted into the ex-vivo tissue to perform tissue sampling by the biopsy device. The ex-vivo tissue was fixed onto a platform. Ten insertions were performed at different locations of the tissue for each needle. In total, 40 needle insertion tests were performed. Figure 3-7(b) shows the optical microscopy image of the biopsy sampled tissue inside the groove. The length of each tissue sample l_s was measured using a digital caliper while the tissue sample remained inside the needle groove after biopsy. After each measurement, the needle and cannula were rinsed to remove the tissue before the next insertion.

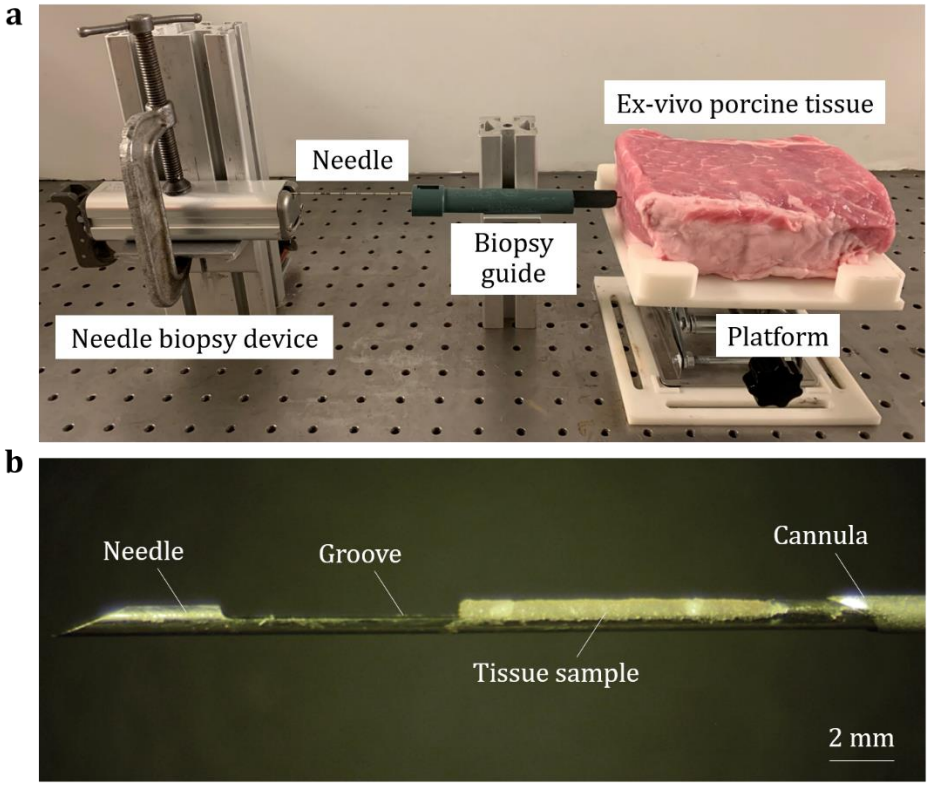

Fig. 3-7 (a) Experimental setup of a trucut needle biopsy and (b) a microscopy image of the needle, cannula and the biopsied tissue sample.

3.2.7 Statistical Analysis

This study conducted one-way analysis of variance (ANOVA) tests to identify: 1) the effect of needle type on needle deflection δ and tissue sampling length l_s and 2) the effect of the location of needle tip point A d_a (tissue separation location) on δ and l_s. The first ANOVA test evaluated the statistical differences in the data of δ and l_s among four needle designs (SB, DB, VB, and AMB needles). The d_a could not only affect the shape of the multi-bevel needle tip but also alter the tissue contact within the needle groove. Therefore, the second ANOVA test grouped four needles into two categories with $d_a < 0$ (SB needle) and $d_a > 0$ (DB, VB, and AMB needles) to identify the effect of d_a on δ and l_s.

The ANOVA with Bonferroni correction was conducted in this study using SPSS (by SPSS, Chicago, Illinois, USA). The δ in the two- and three-layer phantoms were evaluated separately. Each needle type had a d_a value and ten data points of δ and of l_s in the deflection experiment. A total of 40 data points was used in each ANOVA test.

3.3 Results

3.3.1 CEL FEA Results of Needle-Tissue Interaction

The CEL FEA results of needle-tissue interaction for SB, DB, VB, and AMB needle tip types are shown in Figure 3-8. Figure 3-8(a) shows the side view of symmetric plane (OPTS) with the SB needle (as an example) and the tissue. The von mises stress in CEL FEA, called stress hereafter, was calculated based on the deformation and tissue fraction within each Eulerian element (Sec. 3.2.3). At needle displacement D = 0 mm, the tissue was undeformed with zero stress.

Figure 3-8(b) shows the insertion of SB needle with $d_a = -0.5$ mm (tip point A below the groove face). At D = 5 mm, the stresses on the top and bottom of the needle tip were about 17 and 0 kPa, respectively. The SB needle tip A separated the tissue into the top and bottom tissue separation surfaces, denoted as the red dashed lines in Fig. 3-8(b). The top tissue separation surface was deformed and pushed upward by the single-bevel face. This deformation led to the 17 kPa stress on the bevel face and generated the downward face force which would deflect the needle

during insertion (Fig. 3-1(d)). At D = 25 mm (the end of needle travel), the stresses on the top of the needle were about 20, 10, and 20 kPa at the tip, groove face, and back side of the groove, respectively. The stress was low, about 0 kPa, at the bottom of the needle because the location of A was on the needle tip bottom surface. The needle was accelerated with constant acceleration until reaching 8 m/s at D = 25 mm (same condition as the experiment). The stress around the needle tip increased from 17 to 20 kPa. Once the top tissue separation surface reached the groove, it rebounded from the compressed state and filled into the groove. The location of the tip point A below the groove face (d_a = −0.5 mm) allowed the tissue to fill and contact most of the groove, as shown in the isometric view in Fig. 3-8(b). A small unfilled space (the gap between the tissue and groove) was observed at the front side of the groove. The back side of the groove contacted and deformed the tissue filled inside the groove during needle insertion. The SB needle had the tissue contacting with the groove face during insertion which could enable the outer cannula to acquire a sufficient tissue sample in needle biopsy. However, the contact generated the tissue stresses on the groove face, which would aggravate the needle deflection (details to be discussed in Sec. 3.3.2).

The insertion of DB needle with d_a = 0.22 mm (point A above the groove face) is shown in Fig. 3-8(c). At D = 5 mm, the stresses on the top and bottom of the dual-bevel needle tip were more balanced at about 10 and 13 kPa, respectively. At D = 25 mm (the end of needle travel), the stresses on the top of the needle were about 13, 0, and 17 kPa at the tip, groove face, and back side of the groove, respectively. The tissue at the bottom of the needle was also compressed and generated about 17 and 13 kPa stresses at the tip and below the groove, respectively. The bottom bevel face of DB needle was designed to be larger than the top bevel face to have a higher tissue stress, generating an upward face force to balance the bending moment created by the tissue contact stress on the groove face. This dual-bevel tip shape created a tip point A above the groove face (d_a = 0.22 mm). Because of this, the top tissue separation surface was above the groove face leading to more unfilled spaces within the groove, as shown in the isometric views in Fig. 3-8(c). There was almost no tissue contacting the groove face. This greatly reduced the tissue contact stress (about 0 kPa) on the groove face. Due to the higher overall stress at the bottom surface, the needle would be deflected upward during insertion (details to be discussed in Sec. 3.3.2).

Figure 3-8(d) shows the insertion of VB needle with d_a = 0.5 mm (point A above the groove face). At D = 5 mm, the stresses on the top and bottom of the needle tip were about the same (~10 kPa). The stresses at the tip were balanced because the VB had two symmetric vertical

bevel faces with a cutting edge line AB which separated and deformed the tissue laterally. At D = 25 mm, the stresses on the top of the needle were about 13, 10, and 17 kPa at the tip, groove face, and back side of the groove, respectively. The stresses at the bottom of the needle were also about 13 and 10 kPa at the tip and below the groove, respectively. Compared to the SB and DB needles, the stresses were distributed more evenly throughout the needle. This would improve the balance of the bending moments caused by the needle insertion forces and reduce the needle deflection. The top tissue separation surface was above the groove face and generated unfilled spaces due to the location of VB needle tip point A (d_a = 0.5 mm). Compared to the SB and DB needles, the top tissue separation surface was bumpy, as shown in the side view in Fig. 3-8(d). The isometric view in Fig. 3-8(d) indicates that the deformed and rebounded tissue filled in the groove laterally (as illustrated by the red dotted lines) due to the lateral tissue separation by the VB needle tip. Inside the groove, the tissue contacted the groove face with the stress of 10 kPa, generating the downward force to deflect the needle.

The insertion of AMB needle, which had the combined needle tip geometry of DB and VB needles, with d_a = 0.32 mm (point A above the groove face) is shown in Fig. 3-8(e). At D = 5 mm, the stresses on the top and bottom of the combined dual-bevel needle tip were about 10 and 13 kPa, respectively. Like the DB needle, the bottom bevel face was designed to be larger than the top bevel face and generate higher stress to balance the bending moment caused by the tissue contact stress on the groove face. At D = 25 mm, the stresses on the top of the needle were about 13, 10, and 17 kPa at the tip, groove face, and back side of the groove, respectively. The tissue at the bottom of the needle was compressed with the stresses about 17 and 13 kPa at the tip and below the groove, respectively. Like the VB needle, the top tissue surface was above the groove face (d_a = 0.32 mm) and generated unfilled spaces. The isometric view in Fig. 3-8(e) indicates that the tissue also laterally filled into the groove (as illustrated by the red dotted lines) due to the lateral tissue separation by the combined vertical-bevel needle tip. The filled tissue generated the contact stress of 10 kPa on the groove face. Compared to the VB needle, the bottom bevel face of AMB needle could generate higher overall stress at the bottom needle surface, leading to low needle deflection.

In summary, d_a determines the tissue separation location which has a strong influence on the tissue stresses on the needle and the contact with the groove face. The $d_a < 0$ (SB needle) allows the tissue to fill and contact most of the groove and potentially yields a long tissue sampling length.

However, such d_a will create a needle tip shape with a single bevel or a larger top bevel face which generates larger tissue contact stress on the top of the needle tip, deflecting the needle downward. The tissue filling inside the groove will also generate the contact stress with the groove face and aggravate the deflection. The $d_a > 0$ (DB, VB, and AMB needles) will have the top tissue separation surface above the groove face and generate more unfilled spaces inside the groove. This will reduce the tissue contact within the groove and potentially yield a shorter tissue sampling length. However, the needles with $d_a > 0$ can create multiple bevel faces at the needle tip, providing the forces to balance bending moments caused by the tissue contact stresses on the needle and reduce the needle deflection during the insertion.

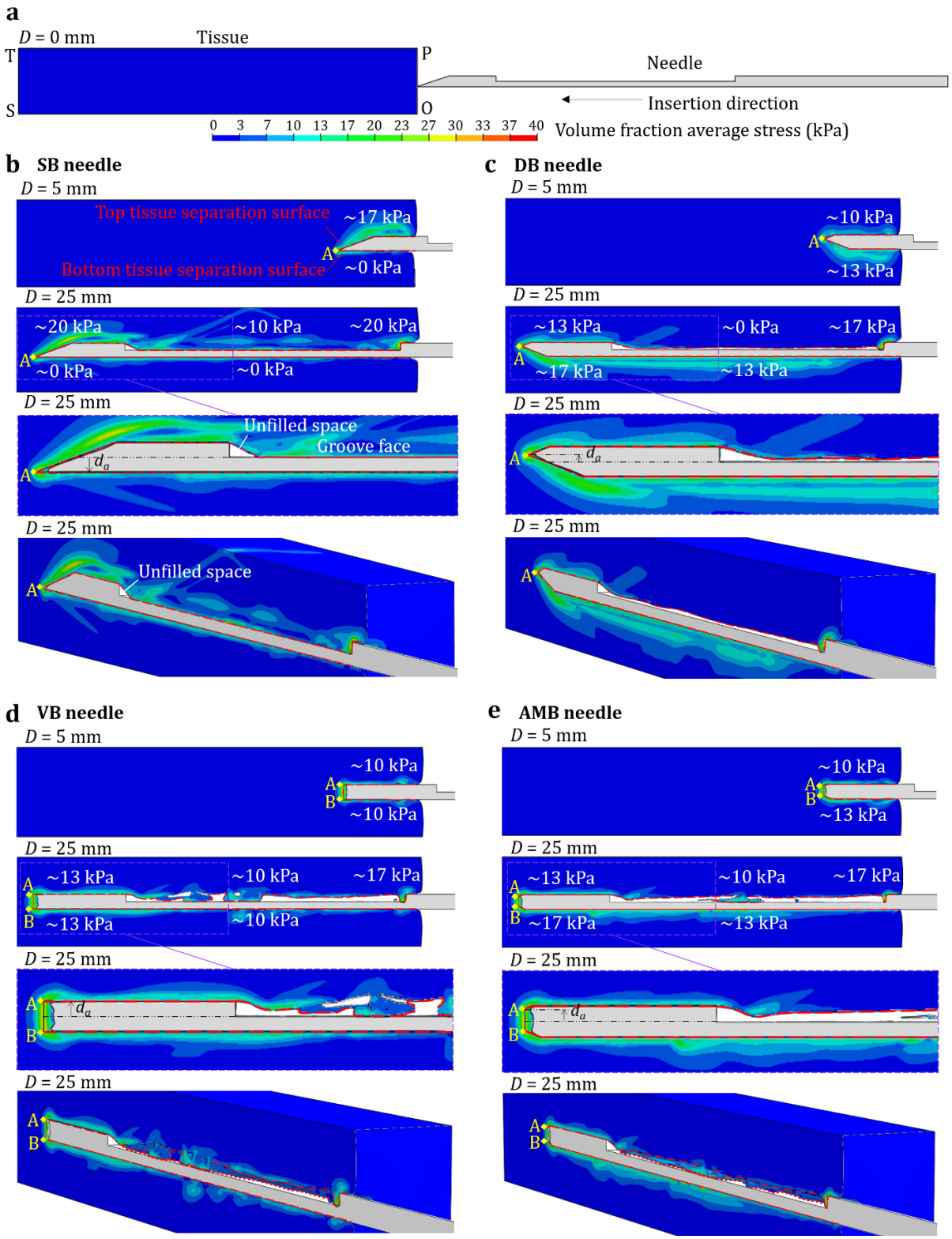

Fig. 3-8 The CEL FEA results of needle-tissue interaction**:** (a) the SB needle and the undeformed tissue before the insertion and the (b) SB, (c) DB, (d) VB, and (e) AMB needles during the insertion.

3.3.2 Needle Deflection and Tissue Sampling Length Measurement Results

Figure 3-9 compares the mean values of the needle deflection δ for the two- and three-layer phantoms (top) and tissue sampling length l_s (bottom) of the SB, DB, VB, and AMB needle tip types. The error bars indicate the standard deviations. Two images of each needle tip (point A or line AB) for the measurements of δ in the two-layer phantom are also shown in Fig. 3-9. The top image shows the needle tip inserted without the phantom. The yellow dashed line represents the needle insertion path without deflection. The bottom image shows the needle deflection after insertion into the transparent two-layer phantom.

For the two-layer phantom, the SB needle ($d_a = -0.5$ mm) had the largest deflection (mean = –1.26 mm, downward δ) among four needle types (all pairwise $p < 0.001$). The magnitude of δ was similar to the clinically measured needle deflection with a median value = 1.77 mm in prostate biopsy [23]. This downward δ was due to the downward face force on the single-bevel face (Fig. 3-8(b)) that deflected the needle as shown in Fig. 93-. Since the $d_a < 0$, the SB needle had tissue filling most of the groove and generated the tissue contact stress on the groove face (Fig. 3-8(b)) which aggravated the deflection. The needle tip image in Fig. 3-9 shows that the downward deflection exposed the groove face to the tissue, further increasing the tissue contact inside the groove. The bent needle allowed the outer cannula to sufficiently sample the tissue inside the groove. Therefore, the SB needle had the longest l_s (mean = 9.2 mm) among four needle types (all pairwise $p < 0.001$).

The DB needle ($d_a = 0.22$ mm) had an upward δ (mean = 0.52 mm) in the two-layer phantom. Compared to the SB needle, the DB needle had an upward deflection with a smaller magnitude of δ ($p < 0.001$). The bottom bevel face generated an upward face force (Fig. 3-8(c)), which overcame the combined downward bending moments caused by the top bevel and groove forces while deflecting the needle upward during the insertion. The DB needle had the $d_a > 0$ and reduced tissue contact inside the groove (Fig. 3-8(c)). The upward deflection further pushed the tissue away from the groove face, resulting in the shortest average l_s (mean = 6.9 mm) among four needle types (all pairwise $p < 0.001$).

The VB needle ($d_a = 0.5$ mm) had a downward δ (mean = –0.17 mm) in the two-layer phantom. Compared to the SB and DB needles, the δ was greatly reduced (both pairwise $p < 0.001$) since the stresses on the needle were distributed more evenly throughout the needle (Fig.

3-8(d)). Because $d_a > 0$, the tissue contact inside the groove was reduced (Fig. 3-8(d)), while the tissue still laterally filled into the groove which generated the tissue contact stress on the groove face and deflected the VB needle downward. The downward deflecting VB needle might help to expose the groove face to the tissue (like the SB needle) and resulted in the second longest average l_s (mean = 8.4 mm, all pairwise $p < 0.001$).

The AMB needle ($d_a = 0.32$ mm) had the smallest average deflection (mean = 0.07 mm) among four needle types (all pairwise $p < 0.001$). Compared to the VB needle, the combined needle tip geometry of the DB and VB needles allowed the AMB needle to balance stresses at the needle tip during the insertion (Fig. 3-8(e)). However, the reduced deflection might lead to less exposure of the groove face to the tissue, resulting in a l_s (mean = 7.6 mm) slightly shorter than that of the VB needle ($p < 0.001$).

For the three-layer phantom, the SB needle still had the largest average deflection (mean = –2.06 mm, downward δ) among four needle types (all pairwise $p < 0.001$). Compared to the two-layer phantom, the deflection in the three-layer phantom was generally larger due to the fibrous structure of the ex-vivo tissue which increased the needle insertion forces (both face force and tissue contact stress on the groove). The DB needle had the similar upward δ (mean = 0.5 mm) in both two- and three-layer phantoms since there was almost no tissue contact stress on the groove. The VB needle had a downward δ (mean = –0.45 mm). This deflection was also aggravated due to the increased tissue contact stress on the groove face. The AMB needle had a downward δ (mean = –0.35 mm). Due to the increased stress on the groove face for the AMB, the upward face force from the bottom bevel might not be able to balance the bending moment caused by the stress on the groove. Therefore, the deflection direction was flipped compared to the deflection in the two-layer phantom and the deflection magnitude was similar to that of the VB needle ($p = 1.000$, non-significant).

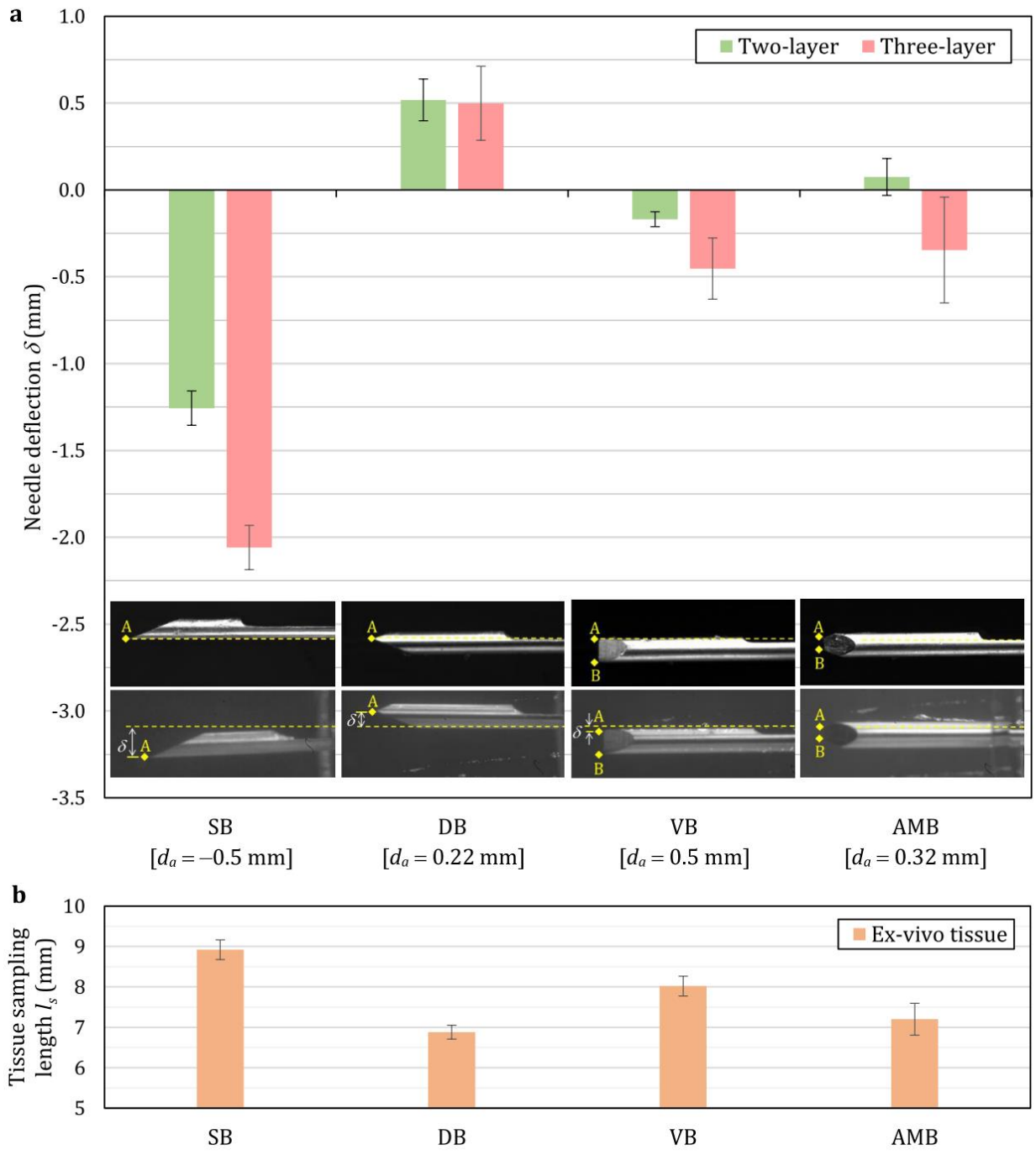

Fig. 3-9 The mean values of needle deflection δ for two- and three-layer phantoms (top) and tissue sampling length l_s (bottom) of the SB, DB, VB, and AMB needle tips (error bars represent the corresponding standard deviations).

Figures 3-10(a) and (b) shows the scatter plots of l_s versus δ in two- and three-layer phantoms, respectively. The data points of SB, DB, VB, and AMB needles are marked as red, green, blue, and yellow, respectively. An inversely proportional relationship between δ and l_s was observed for both two- and three-layer phantoms. The R^2 values for the trends in two- and three-layer phantoms were 0.83 and 0.73, respectively. This concluded that the trends of needle defection for SB, DB, VB, and AMB needles in in two- and three-layer phantoms were the same.

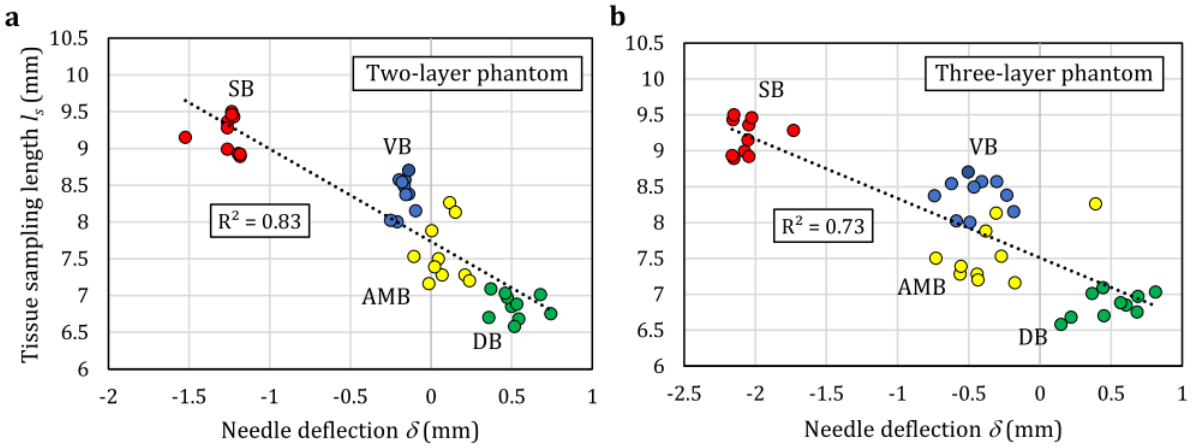

Fig. 3-10 The scatter plots for l_s versus δ in (a) two- and (c) three-layer phantoms.

In summary, two key findings were: 1) the multi-bevel needle tip geometry could balance the bending moments caused by the insertion forces to reduce the needle deflection and 2) the d_a affected the δ and l_s. The SB needle had the largest downward average deflection; however, it had the longest l_s because of the sufficient tissue contact inside the groove enabled by the $d_a < 0$ and resultant downward δ. The DB needle had the $d_a > 0$ and a reduced magnitude but upward δ which pushed the tissue away from the groove face, resulting in the shortest l_s. The VB and AMB needles had better balance of bending moments, and therefore greatly reduced the δ. However, the l_s of VB and AMB needles were still smaller in comparison to that of SB needle due to the reduced tissue contact inside the groove caused by $d_a > 0$.

3.3.3 ANOVA Analysis Result – Effect of Tissue Separation Location on Needle Deflection and Tissue Sampling Length

To elucidate the effect of tissue separation location relative to the groove face d_a on needle deflection δ and tissue sampling length l_s, the experimental data of four needle types (SB, DB, VB, and AMB needles) were analyzed in ANOVA by grouping them into two categories: $d_a < 0$ (SB needle) and $d_a > 0$ (DB, VB, and AMB needles). The ANOVA result indicates that the effect of d_a on δ and l_s was statistically significant at 0.05 significance level. The yielded F ratios were 202, 154, and 50.3 for the δ in two-layer phantom, the δ in three-layer phantom, and l_s, respectively.

Figure 3-11 illustrates the effect of d_a on δ and l_s. It was found that the needle tip geometry with $d_a < 0$ (SB needle) generated a large downward δ in both phantoms (Fig. 3-11(a)) while yielding long l_s (Fig. 3-11(b)). Since $d_a < 0$, the tissue was separated close to the bottom of the needle which led to larger tissue stresses on the top of the needle (Fig. 3-8(b)) and yielded a downward needle deflection during insertion. The $d_a < 0$ also enabled a tissue separation below the groove face and thus allowed the tissue to contact most of the groove, yielding a long tissue sample. The needle tip geometry with $d_a > 0$ (DB, VB, and AMB needles) had the smaller magnitude of δ in both phantoms (Fig. 3-11(a)) but short l_s (Fig. 3-11(b)). The $d_a > 0$ could create a multi-bevel needle tip geometry to balance the bending moments caused by the insertion forces and reduce the needle deflection (Fig. 3-11(a)). However, the tissue separation above the groove face reduced the tissue contact inside the needle groove and the resultant tissue sampling length (Fig. 3-11(b)).

The ideal tissue sampling for accurate cancer diagnosis in needle biopsy has low needle deflection (small δ in magnitude) and long l_s. Results indicate a potential trade-off between the goals of decreasing δ and increasing l_s when varying d_a. A needle tip geometry with the tissue separation point below the needle groove face ($d_a < 0$) can have adequate tissue contact inside the needle groove for long l_s. However, the feature of multiple bevel faces should be added to the needle tip with this low tissue separation point to generate the forces to balance bending moments and avoid large needle deflection during insertion.

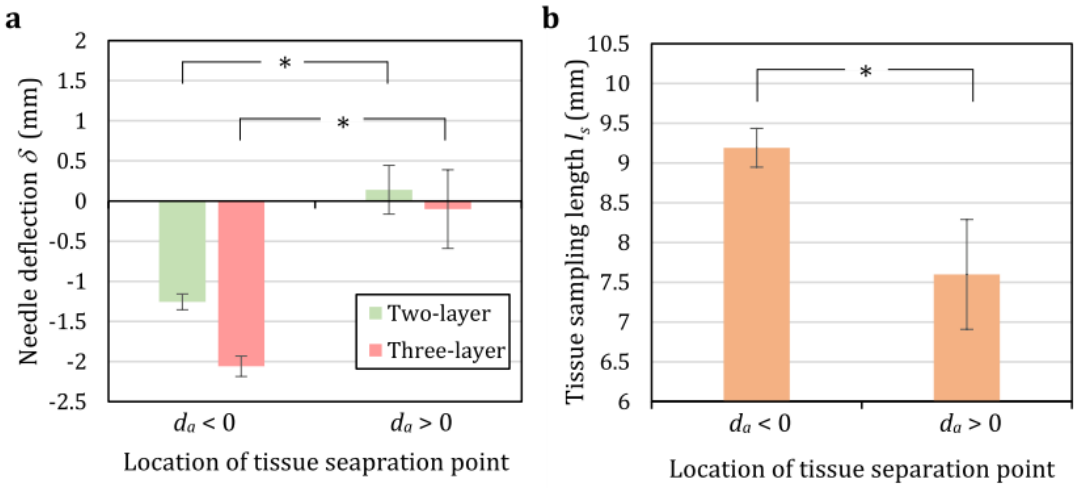

Fig. 3-11 The effect of location of tissue separation point d_a on mean values and standard deviations of (a) needle deflection δ and (b) tissue sampling length l_s. (∗: $p < 0.001$)

3.4 Conclusions

This study investigated the effect of needle tip geometry on needle deflection and tissue sampling length. The major finding was that the tissue separation location at the needle tip affects both needle deflection and tissue sampling length. A multi-bevel needle tip geometry could balance the bending moments caused by the insertion forces and reduce the needle deflection. However, the multiple bevel faces on the needle tip altered the tissue separation location, affecting the tissue contact inside the needle groove and the resultant tissue sampling length. Future work will focus on creating a needle tip geometry which can enable both low deflection and long tissue sampling length in needle biopsy. A multi-bevel needle tip geometry with the tissue separation point below the needle groove face may reduce the needle deflection while maintaining an adequate tissue sampling length. A needle insertion model which can simulate the deformation of both needle and tissue will also need to be established to predict the needle deflection and guide the needle tip design for a variety of biopsy procedures.

Chapter 4: Multi-Beveled Needle for Accurate Insertion and Tissue Sampling in Biopsy

4.1 Introduction

Needle biopsy is commonly performed as a minimally invasive tissue sampling method for cancer diagnosis of lymph node, lung, liver, and prostate [19, 57, 58]. Accurate needle deployment and adequate tissue sampling in biopsy are essential for accurate diagnosis and individualized treatment decisions [1–4]. As discussed in Chapter 3, currently available trucut biopsy needle with a single-bevel tip can yield long and adequate tissue sample but often induce significant deflection during biopsy [4, 23, 24]. Such needle deflection causes variances in the targeted and actual locations of the sampled tissue core, leading to lesion missampling or undersampling [24] as well as false-negative and cancer misdiagnosis [27, 28]. Moreover, biopsy sites may be in proximity to critical vessels and nerves in lymph node biopsy [80, 81], pulmonary alveolus in lung biopsy [82, 83], and gall bladder in liver biopsy [3]. The deflected needle could be off the target site and cause collateral damages. This puts patients at a higher risk of complications and is always a major concern of clinicians who perform trucut biopsy procedure [3, 30].

The multi-bevel needle tip geometry, as presented in Chapter 3, has demonstrated to reduce needle deflection by balancing the top and bottom face forces to reduce the needle bending moment during insertion as shown in Fig. 4-1(a). However, the tissue sampling length may be comprised. In Chapter 3, the multi-bevel tip geometry has been created and shown the location of tissue separation point at the needle tip relative to the groove face greatly influences the tissue sampling length. The tissue separation point needs to be below the needle groove face to enable the sufficient tissue contact inside the groove for subsequent cutting and acquisition of a long tissue sample by the cannula.

This study investigates a new multi-bevel needle tip geometry to enable both low needle deflection and high tissue sampling volume in trucut biopsy. This study invents a multi-bevel needle tip with high yield in tissue sample while maintaining the low bending moment and minimal deflection of needle during insertion. During biopsy, as shown in Fig. 4-1(b), the needle is first fired at high speed (about 4 m/s) and subjected to the cutting, top face, and bottom face forces at the tip as well as the tissue pressure and friction force on the needle. The bottom face force is critical to balance the combined top face force and tissue pressure in the groove, resulting the low needle bending moment and deflection. Next, as shown in Fig. 4-1(c), the outer cannula is then fired to cut and store the tissue inside the needle groove. With the tissue separation point A below the groove face, the tissue is filled inside most of the groove and cannula can cut and acquire a long tissue sample.

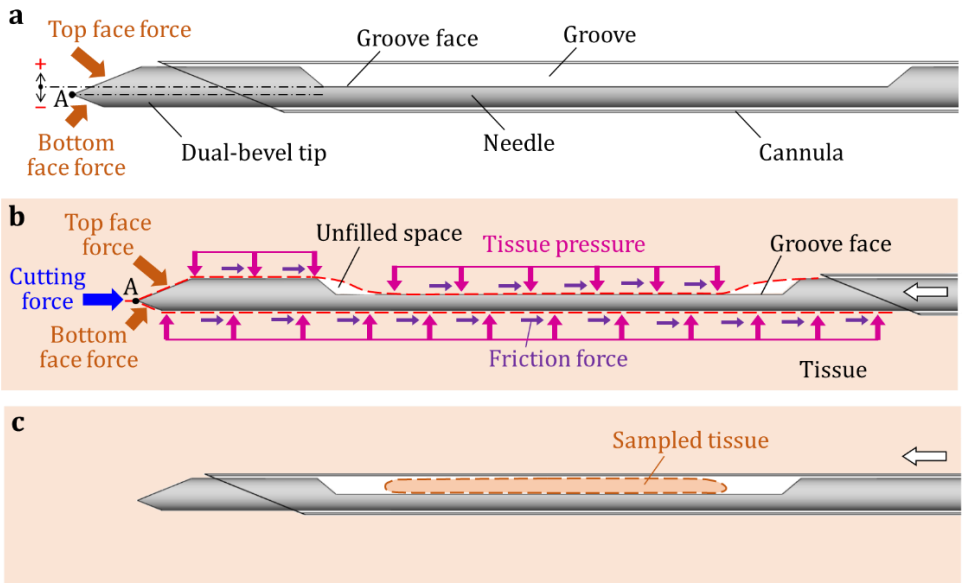

Fig. 4-1 The multi-bevel needle with the tip point A below the groove face for low needle deflection and long tissue sample in biopsy, (b) the needle insertion forces to balance bending moments to reduce needle deflection during firing, and (c) long tissue sampling enabled by the location of tissue separation point below the groove face.

In this chapter, the needle deflection and tissue sampling of the current single-bevel and three multi-bevel tip geometries in trucut biopsy are quantified and compared. The needle deflection is experimentally measured in optically transparent tissue-mimicking phantoms and analyzed by the image processing. The length and weight of sampled tissue in biopsy of ex-vivo

chicken breast tissue are investigated. Finally, the evaluation of the new multi-bevel trucut needle biopsy device on human cadaver prostate is performed.

4.2 Materials and Methods

4.2.1 Needle Tip Geometry

The single-bevel (SB) needle, as shown in Fig. 4-2(a), and three multi-bevel needles, as shown in Figs. 4-2(b)-(d), are investigated in this study. Three multi-bevel needles have four facets: the top bevel (on the same side of the groove face), bottom bevel, and two side bevels. The forces on the top face is F_{tf} and on the bottom and side bevels are F_{bf} and F_{sf}, respectively. These types of three multi-bevel needles shown in Figs. 4-2(b)-(d) are denoted as the low multi-bevel (LMB), aligned multi-bevel (AMB), and high multi-bevel (HMB) with the needle tip point A lower than, aligned with, and higher than the groove face, respectively. The distance from the tissue separation point A to the groove face d_a, as defined in Chapter 3 and Fig. 4-2(e), is negative, zero, and positive for the LMB, AMB, and HMB needle, respectively. The effect of d_a on needle deflection and tissue sampling length and weight is studied on LMB, AMB, and HMB needles. Fig. 4-2(e) defines the needle groove length l_g and thickness t_g. The distance between point A and the bottom edge of the needle is d_b. The sum of d_b and d_t (the distance between point A and the top edge of the needle) is the needle diameter. Both d_b and d_t have positive values.

The shape, features, forces on four facets, and optical microscopy images of the SB, LMB, AMB, and HMB needle tip are shown in Figs. 4-2(a)-(d) and discussed as follows:

- SB needle: The SB needle, as shown in Fig. 4-2(a), has a bevel face (on the same side of the needle groove) and two small side lancets at the tip. These two lancets creates a sharp tip point A [84]. The tissue is cut and separated at point A, contacts the bevel and lancet faces, and generates the downward forces, F_f and F_{lf}, on the bevel face and two lancets, respectively, which bend the needle during insertion. The needle tip point A is below the groove face ($d_a < 0$).

- LMB needle: The LMB needle, as shown in Fig. 4-2(c), has the bottom and side bevels generating the upward face forces F_{bf} and F_{sf} to balance the downward bending moments caused by the top face F_{tf} and tissue pressure. Similar to the SB needle, the LMB needle has the tip point A below the groove face ($d_a < 0$).
- AMB needle: The AMB needle, as shown in Fig. 4-2(d) and compared to LMB needle, has larger bottom and side bevels for the larger combined upward forces F_{bf} and F_{sf}, aiming to reduce the downward needle deflection.
- HMB needle: Like LMB and AMB needles, the HMB needle, as shown in Fig. 4-2(e), has the bottom bevel face much larger than the other three faces. This will greatly increase F_{bf} and F_{sf} to deflect the needle upward during the insertion.

In this study, four needle tip geometries and the groove were fabricated by computer numerical control grinding using the 18-gauge (1 mm diameter) AISI 304 stainless steel rod. In the fabrication, the steel rod was first tilted by a bevel angle of 23.5° to grind a baseline bevel facet (for the SB needle). The lancets for the SB needle was added onto this bevel face [84]. For LMB, AMB, and HMB needles, the rod was then tilted to a second bevel angle of 12° and rotated around the needle centerline axis by 180° and ±110° from the baseline bevel facet to create the bottom and two side bevel facets, respectively. The ground amount for each bevel facet was determined by the d_a and d_b at the needle tip. The SB needle has $d_a = -0.43$ mm and $d_b = 0$ mm. The LMB needle has $d_a = -0.22$ mm and $d_b = 0.2$ mm. The AMB needle has $d_a = 0$ mm and $d_b = 0.43$ mm. The HMB needle has $d_a = 0.37$ mm and $d_b = 0.8$ mm. Finally, the rod was tilted back to 0° to grind the needle groove with the l_g = 22 mm and t_g = 0.43 mm. All four needles had the same groove geometry.

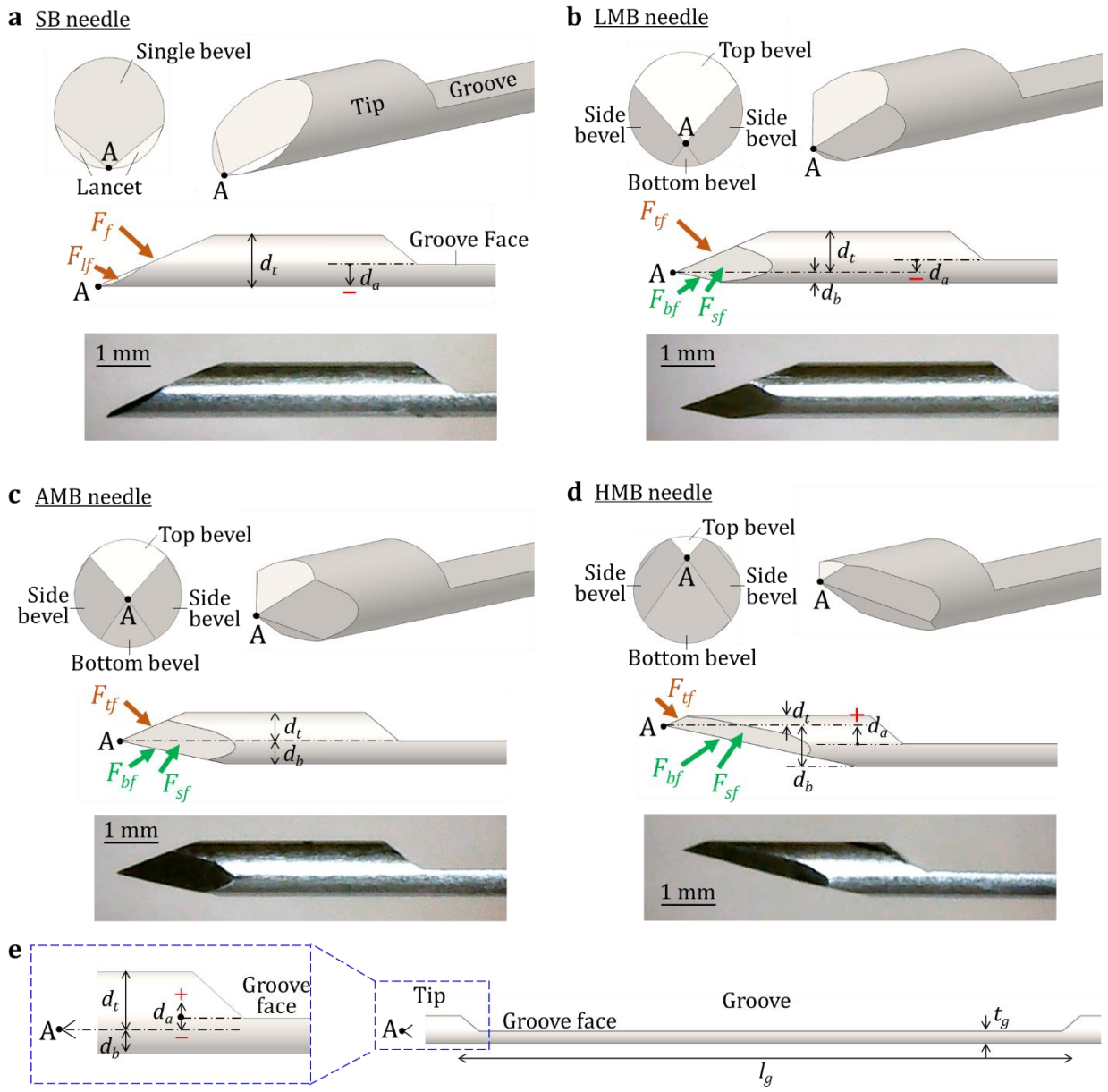

Fig. 4-2 The needle tip geometry, tip face forces, and optical microscopy image of the (b) SB, (c) LMB, (d) AMB, and (e) HMB needles, and (e) the schematic diagram to define the needle parameters of d_a, d_b, d_t, l_g, and t_g.

4.2.2 Tissue-Mimicking Phantoms

The tissue-mimicking phantoms made of polyvinyl chloride (PVC), as shown in Fig. 4-3(a), are used as the surrogate of soft tissue in the needle deflection experiments (details to be presented in Sec. 4.2.3). PVC is a common tissue-mimicking material and can be fabricated with

the hardness and needle insertion properties similar to in-vivo prostate tissues [70, 71]. The softener, PVC polymer (both by M-F Manufacturing, Ft. Worth, Texas, USA), and mineral oil (by W.S. Dodge Oil, Maywood, California, USA) were blended together to create the phantom material with the targeted hardness [70]. In this study, the transparent PVC phantom with 100 mm in length, 80 mm in width, and 30 mm in height, as shown in Fig. 4-3(a), was fabricated. Each phantom has a uniform hardness to study needle deflection in a specific material property. Three PVC phantoms, namely Phantoms I, II and, III, were built to mimic the soft tissue surrounding prostate, outer soft layer of prostate, and inner hard core of the prostate with Shore OOO-S hardness of 23, 34 and 55, respectively. These hardness values were determined based on clinician's haptic feedback for the hardness of a specific organ.

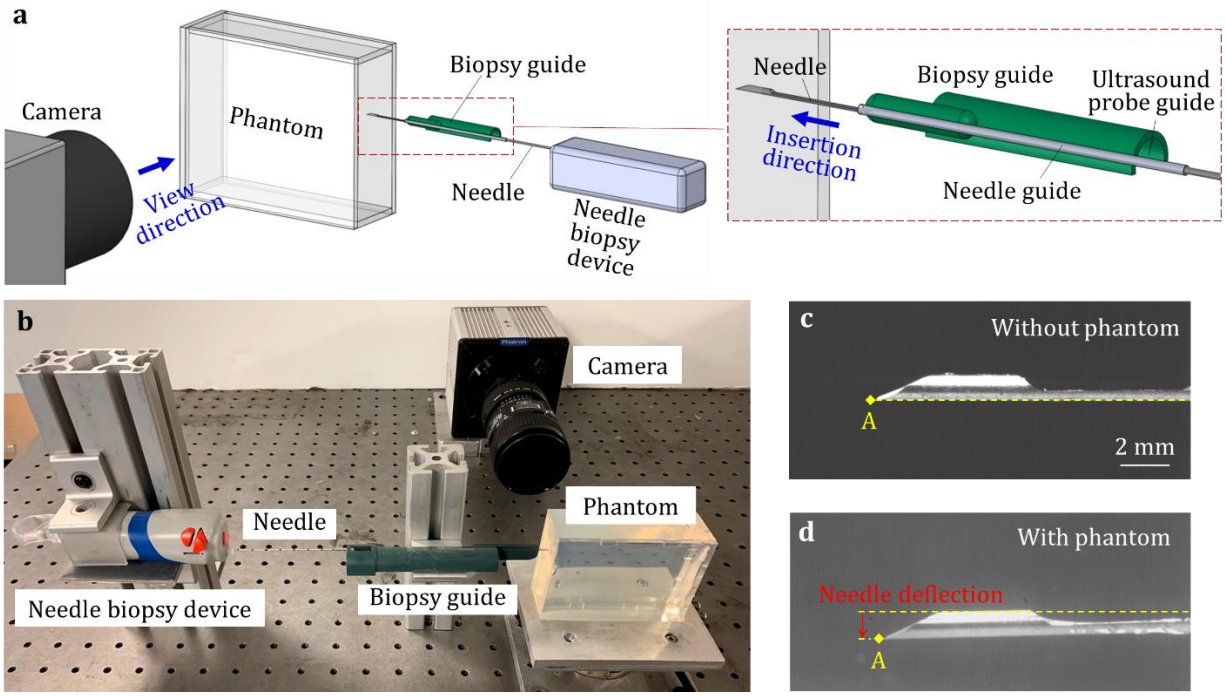

Fig. 4-3 (a) An overview of the needle deflection experiment, (b) the experimental setup, and the images with the locations of SB needle tip point A at the end of the insertion (c) without and (d) with the tissue-mimicking phantom.

4.2.3 Needle Deflection Experimental Setup

The setup for needle deflection experiment is shown in Fig. 4-3. A commercial spring-loaded needle biopsy device (SelectCore Variable Throw Biopsy Device by Inrad, Kentwood,

Michigan, USA) was used to perform the needle insertion with a 25 mm firing length for both needle and cannula (Fig. 4-1). Both needle and cannula were installed on the biopsy device and supported by a prostate biopsy guide (Endfire Biopsy Guide by BK Medical, Peabody, Massachusetts, USA). The biopsy guide had a plastic semi-cylindrical body for the ultrasound probe guide and a metal tube for the needle guide (Fig. 4-3(a)). The needle guide was fixed to position the needle and support it to avoid buckling during needle insertion. In the experiment, the needle guide was used to place the needle at the surface of the phantom for insertion. The biopsy device fired only the needle at a high speed (about 4 m/s) to have a clear view of the needle deflection. A high-speed camera (Model 100K by Photron, San Diego, California, USA) with 1024×1024 pixel resolution and a 5.6× magnification was used to capture the images of needle tip before and after the insertion to measure the needle deflection.

To acquire the baseline tip position without deflection, the needle was first inserted without the phantom as the image of SB needle shown in Fig. 4-3(c). The needle was then advanced by the biopsy device into the transparent phantom as shown in Fig. 4-3(d). The needle deflection δ was calculated as the vertical distance (relative to the insertion direction) between the final tip locations with and without the phantom. Ten insertions of each needle tip types (SB, LMB, AMB, and HMB) were performed for each phantom (Phantoms I, II, and III) at different locations in the phantom. A total of 120 needle insertion tests were performed. The images were analyzed using Matlab (by MathWorks, Natick, Massachusetts, USA) to identify the needle tip locations and quantify the deflections.

4.2.4 Ex-Vivo Tissue Sampling Test

The tissue sampling amount for four needle tip types (SB, LMB, AMB, and HMB) were quantified in the trucut needle biopsies test using the ex-vivo chicken breast tissue, as shown in Fig. 4-4(a). The needle and outer cannula were sequentially fired by the biopsy device (same as that of needle deflection experiments) into the ex-vivo tissue fixed on a platform for tissue sampling. For each type of needle tip, ten insertions were performed at different locations of the ex-vivo tissue. A total of 40 needle insertion tests were conducted. An example of the optical microscopy image of the sampled tissue inside the groove is shown in Fig. 4-4(b). The length of each tissue sample l_s was measured using a digital caliper with the sample stayed on the needle groove after biopsy. The tissue sample was then removed from the groove to measure the weight

w_s using a digital scale (Gemini-20 by American Weigh Scales, Cumming, Georgia, USA). The needle and cannula were rinsed for cleaning before the next insertion.

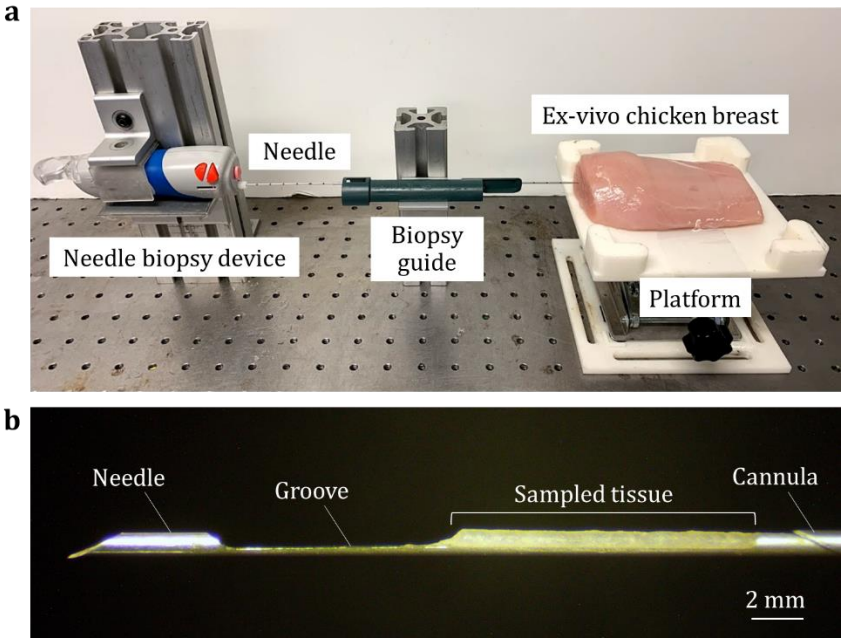

Fig. 4-4 (a) The experimental setup of ex-vivo tissue sampling test and (b) a microscopy image of the needle, cannula, and the sampled tissue.

4.2.5 Cadaver Prostate Tissue Sampling Test

The tissue sampling test on cadaver prostate tissue was conducted to evaluate the biopsy performance on human tissue for SB and LMB needles (both with $d_a < 0$). The cadaver prostate was acquired from the University of Michigan Medicine Pathology Morgue under the donation consent allowing for research purpose. The tissue was refrigerated for storage and recovered at room temperature prior to the test. The prostate has the size about 45 mm in diameter with part of the bladder wall and the surrounding soft tissues. In this test, the tissue surrounding the prostate was fixed to maintain the in-vivo weakly supported condition for prostate biopsy. Five insertions were performed at different locations of the prostate for the SB and LMB needles. A total of 10 needle insertion tests were conducted in the cadaver prostate. The length of each tissue sample was measured using a digital caliper with the sample stayed on the needle groove. After each measurement, the needle and cannula were rinsed to remove the tissue before the next insertion.

4.2.6 Statistical Analysis

The one-way analysis of variance (ANOVA) tests were performed to calculate the statistical significance among the experimental data of needle deflection (in three phantoms) and the lengths and weights of tissue samples (in chicken breast and cadaver prostate) for SB, LMB, AMB, and HMB needles. Each needle has ten data points for each measured variable. A total of 40 data points was used in each ANOVA test. The mean values in each experiment of any two of the four needles were compared (pairwise comparisons) to calculate the *p* values with Bonferroni correction at 95% confidence level.

4.3 Results

4.3.1 Needle Deflection and Tissue Sampling Results

Figure 4-5 summarizes the mean values of needle deflection δ in three phantoms (top), and tissue sample length l_s and weight w_s of chicken breast tissue (bottom) with the error bars representing the standard deviations for the SB, LMB, AMB, and HMB needles. Two images of needle tip point A in Phantom II experiment are shown in Fig. 4-5. The top image shows the needle tip location before the insertion with the yellow dashed line marked as the insertion path without needle deflection. The bottom image shows the needle with deflection after inserting into the phantom. The optical microscopy images of the tissue samples on the needle groove are also presented. Table 4-1 shows the *p* values in ANOVA tests for each pairwise comparison (any two of SB, LMB, AMB, and HMB needles) of δ, l_s, and w_s.

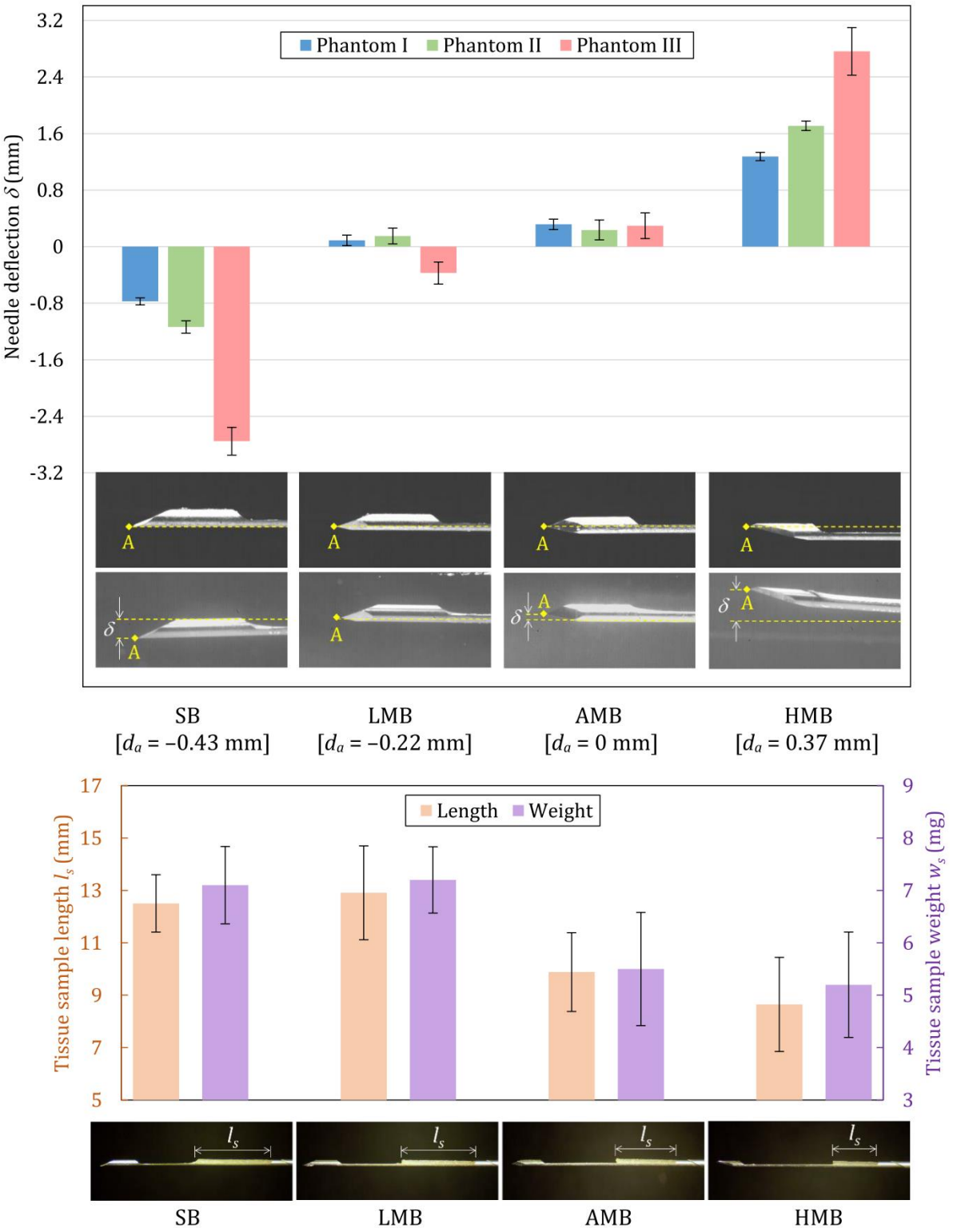

Fig. 4-5 The mean values of δ (top) and l_s and w_s (bottom) in three phantoms for SB, LMB, AMB, and HMB needles (error bars represent the corresponding standard deviations) and the images in the needle deflection and tissue sampling experiments.

Table 4-1 Results of p values in ANOVA tests for the pairwise comparisons of δ, l_s, and w_s for SB, LMB, AMB, and HMB needles. (∗: $p < 0.001$)

		Needle deflection δ			Tissue sampling	
		Phantom I	Phantom II	Phantom III	Length l_s	Weight w_s
SB	LMB	∗	∗	∗	1.000	1.000
	AMB	∗	∗	∗	0.004	0.002
	HMB	∗	∗	∗	∗	∗
LMB	AMB	∗	0.457	∗	0.001	0.001
	HMB	∗	∗	∗	∗	∗
AMB	HMB	∗	∗	∗	0.510	1.000

The SB needle (d_a = –0.43 mm) had the large δ of –0.78, –1.14, and –2.75 mm in Phantoms I, II, and III, respectively, and also yielded the long l_s of 12.5 mm with w_s of 7.1 mg. The downward force on the SB face significantly deflected the needle, as shown in Fig. 4-5. The needle deflection correlates positively with the hardness of the phantom material due to the increased needle insertion forces. This has resulted the largest downward δ in all three phantoms among four needles (all with pairwise $p < 0.001$ as shown in Table 4-1). The magnitude of δ was similar to the clinically measured needle defection (using ultrasound images) with a median value of 1.77 mm in prostate biopsy [23]. Since the tissue separation point is below the groove face ($d_a < 0$), the SB needle allowed the tissue to fill the groove and enabled a long (over 12 mm) tissue sample, as shown in Fig. 4-5. However, such tissue contact generated the tissue pressure on the groove face which further aggravated the needle deflection.

The LMB needle (d_a = –0.22 mm) had the low δ of 0.09 (almost 0), 0.15, and –0.37 mm in Phantoms I, II, and III, respectively, while maintained the long l_s of 12.9 mm with w_s of 7.2 mg. Compared to the SB needle, the magnitude of δ was much lower in all three phantoms ($p < 0.001$, Table 4-1). This indicated that the LMB needle could have better needle deployment accuracy with low deflection in biopsy procedure. The bottom and side bevel faces generated the upward face forces which balance the downward bending moments caused by the top face force and tissue pressure on the groove face. This has resulted the slightly upward δ in Phantoms I and II, as shown in Fig. 4-5. In Phantom III, the δ became downward because of the increased top face force and tissue pressure caused by the high hardness of Phantom III. Since $d_a < 0$, as shown in Fig. 4-5, the LMB needle also had high l_s and w_s, which are equivalent to that of the SB needle (p = 1.000, non-

significant, as indicated in Table 4-1). The LMB needle enabled both accurate needle insertion and tissue sampling in biopsy and demonstrated to be an ideal tip design.

The AMB needle (d_a = 0 mm) had the upward δ of 0.32, 0.24, and 0.30 mm in Phantoms I, II, and III, respectively, and the l_s of 9.9 mm with w_s of 5.5 mg. Compared to the LMB needle, the AMB needle had a larger upward δ for three phantoms ($p < 0.001$ in Phantoms I and III, $p = 0.457$ in Phantom II). The AMB needle, compared to the LMB needle, had larger bottom and side bevel faces and generated the upward forces to deflect the needle upward, as shown in Fig. 4-5. The δ was almost identical in all three phantoms for AMB needle. Since d_a = 0 mm, the location of the tissue separation point was higher than that of SB and LMB needles, resulting in lower l_s and w_s ($p < 0.005$ with both SB and LMB needles).

The HMB needle (d_a = 0.37 mm) had the large upward δ of 1.27, 1.71, and 2.76 mm in Phantoms I, II, and III, respectively, and the short l_s of 8.6 mm with w_s of 5.2 mg. Since the bottom bevel face was much larger than the other three faces, the combined bottom and side face forces significantly deflected the needle upward, as shown in Fig. 4-5, with all pairwise $p < 0.001$. The magnitude of δ also increased with the hardness of phantom material, the same trend observed in the δ of SB needle. The HMB needle has the lowest l_s and w_s among all four needles ($p < 0.001$ with both SB and LMB needles, $p = 0.510$ with the AMB needle) due to $d_a > 0$.

In summary, the LMB needle is an ideal design enabling both low needle deflection by self-balancing the needle bending moments and high tissue sampling (l_s and w_s) with $d_a < 0$. The AMB needle also had low needle deflection while the tissue sampling was limited due to $d_a = 0$. The SB needle in current trucut biopsy device ($d_a < 0$) yielded high l_s and w_s but had a large downward deflection during needle insertion. Finally, the HMB needle caused large upward deflection and greatly reduced l_s and w_s as a result of the high tissue separation location ($d_a > 0$).

4.3.2 Cadaver Prostate Test Results

Figure 4-6 summarizes the results of tissue sampling length in the cadaver prostate tests for SB and LMB needles (both with $d_a < 0$). The average sample length of 14.8 and 15.6 mm for the SB and LMB needles, respectively. The LMB needle had the equivalent tissue sampling length compared to that of the SB needle ($p = 0.676$). The capability of tissue sampling on human cadaver prostate for the LMB needle biopsy device was confirmed.

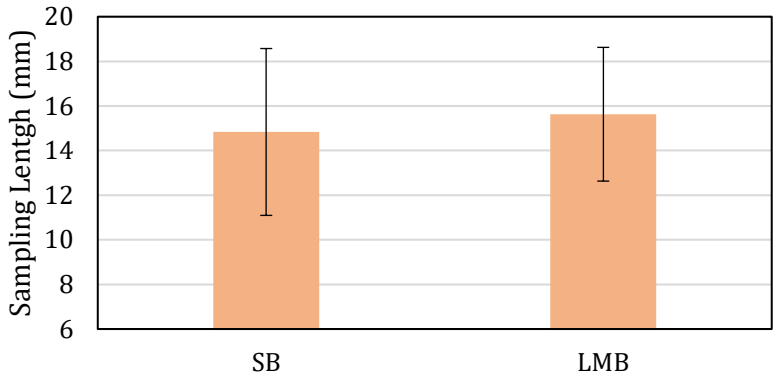

Fig. 4-6 The mean values of tissue sampling length in cadaver prostate tests for SB and LMB needles.

4.4 Conclusions

This study revealed two critical design criteria for ideal needle in trucut biopsy: 1) the tissue separation point should be below the needle groove face to ensure high tissue sampling and 2) the multi-bevel needle tip geometry, which can have bevel faces generating the upward forces while maintaining the low separation point, will be needed to balance the bending moments during the insertion and enable low needle deflection. In this study, the LMB needle has demonstrated the lowest needle deflection (with up to 88% reduction in magnitude compared to SB needle) and long tissue sampling among SB, LMB, AMB, and HMB needles. The capabilities of improved needle deployment accuracy and tissue sampling on human tissue for the LMB needle biopsy device have also been confirmed. Results from this study can have broad applications for various biopsy procedures as well as other procedures requiring accurate needle insertion.

Chapter 5: Interaction Modeling of Needle Deflection and Tissue Deformation

5.1 Introduction

The needle deflection and tissue deformation are coupled with needle-tissue interaction phenomenon during the needle insertion into soft tissue. The deflected needle interacts with the soft tissue to generate high forces and bending moments on the needle to further increase the needle deflection and deform the soft tissues and the surrounding organ [25, 29, 33]. The deformed tissue also exerts forces on the needle and aggravates the needle deflection – forming an arc rather than a predictable straight line [24, 35, 80]. As discussed in Section 1.1, such coupled needle-tissue interaction strongly affects the deployment accuracy of needle to the diseased lesion site to acquire tissue samples for diagnosis [4, 25].

A model to predict the needle deflection and tissue deformation is crucial to gain insights of needle-tissue interaction and improve the needle biopsy technology for more accurate acquisition of targeted disease tissue enabling a definite diagnosis. As presented in Section 1.2, needle-tissue interaction modeling using the finite element analysis (FEA) is common modeling approach to visualize the tissue deformation and contact with the needle during insertion. The needle cutting was simulated by updating the deformed mesh coordinates in FEA based on the needle position to maintain the needle-tissue boundaries and calculate the resultant tissue deformation [85, 86]. The cohesive zone (CZ) method in Lagrangian FEA was applied to model the tissue rupture by assigning the tissue separation threshold level when contacting with the needle [40, 50, 51]. The CZ method enabled a better representation of the tissue deformation around the needle. However, the CZ method required a pre-defined element separation path during needle insertion. In Chapter 3, the coupled Eulerian-Lagrangian FEA has demonstrated the capability to effectively simulate tissue rupture and large tissue deformation by modeling the tissue

and needle using the Eulerian and Lagrangian analysis, respectively. However, the aforementioned studies were limited to the rigid needle (no bending/deflection). A modeling method to simultaneously predict the needle deflection and tissue deformation remained unexplored.

This study establishes a needle-tissue interaction modeling using the Lagrangian analysis coupled with smoothed particle Galerkin (SPG) method, denoted as L-SPG, to investigate the needle deflection and tissue deformation in biopsy. SPG is a mesh-free method to discretize the simulated object into particles and has demonstrated the capability of modeling soft tissue deformation during tool cutting without mesh distortion [87]. This study utilizes L-SPG to model the deflection of a deformable needle and the deformation of soft tissue by the Lagrangian analysis and SPG method, respectively. In this chapter, the configuration of the L-SPG model is presented. The modeling results are then discussed and compared with the experimental results of needle deflection and tissue sampling (as the outcome of needle-tissue interaction) in Chapter 4.

5.2 Materials and Methods

The needle geometry, L-SPG model configuration, material and contact properties, and L-SPG model verification are presented.

5.2.1 Needle Geometry

Four trucut biopsy needle geometries, denote as single-bevel (SB), low multi-bevel (LMB), aligned multi-bevel (AMB), and high multi-bevel (HMB) needles, as shown in Figs. 5-1(a), (b), (c), and (d), respectively, are utilized to study the tissue interaction with different needle geometries. The SB needle is the currently available needle design with a single bevel face at the needle tip and a groove at the same side to store the biopsied tissue sample as shown in Fig. 5-1(a). Three multi-bevel needles, LMB, AMB, and HMB needles, as defined in Chapter 4, have four bevel facets at the needle tip with the tissue separation location lower, aligned, and higher than needle groove face. The distance from the needle tip point A to the groove face d_a is negative, zero, and positive for the LMB, AMB, and HMB needles, receptively. The distance between point A and the top edge of the needle is d_t. The sum of d_t and d_b (the distance between point A and the

bottom edge of the needle) is the needle diameter. Both d_t and d_b have positive values. Figure 5-1(e) defines the distance between point A to the front edge of needle groove opening l_t, groove opening length l_g, groove thickness t_g, and distance between the back edge of groove opening to the needle base point B l_b.

Details of the SB, LMB, AMB, and HMB needle tip geometries are as follows:

- SB needle: The SB needle, as shown in Fig. 5-1(a), has a bevel face with a bevel angle ζ (on the same side of the needle groove) and two small side lancets at the tip. The surface normal of this bevel face is illustrated by the blue arrow in the front view of Fig. 5-1(a). The lancet facets have the same bevel angle ζ_l and are orientated with $\pm\theta_l$ from the bevel face around centerline axis O-O (the axis through the center point O) as the front and side views shown in Fig. 5-1(a). These two lancets creates a sharp tip point A [84] below the groove face with $d_a <$ 0.
- LMB needle: The LMB needle, as shown in Fig. 5-1(b), has the top, bottom and two side bevel facets. The bevel angles for the top and bottom bevel facets are denoted as ζ and ζ_b, respectively. The surface normal of the top bevel facet is illustrated by the blue arrow in the front view of Fig. 5-1(b). The side bevel facets have the same bevel angle ζ_s and are orientated with $\pm\theta_s$ from the top bevel facet ($\theta_s > 90°$, at the opposite side relative to the needle groove face) around centerline axis O-O as shown in Fig. 5-1(b). These four facets also create a sharp point A with $d_a < 0$ as that of SB needle.
- AMB needle: The AMB needle, as shown in Fig. 5-1(c), also has four bevel facets with the same bevel angles and orientations with respect to the top bevel facet as those of LMB needle. These four facets create the tip point A aligned with the needle grove face ($d_a = 0$).
- HMB needle: With the same bevel angles and orientations as those of LMB and AMB needles, the HMB needle, as shown in Fig. 5-1(d), has the tip point A higher than the needle grove face ($d_a > 0$).

In this study, all four needles have the needle diameter of 1 mm (18-gauge), the needle groove with the l_g = 22 mm, t_g = 0.43 mm, and l_b = 8 mm. The SB needle has $\zeta = 23.5°$, $\zeta_l = 35°$, $\theta_l = 42°$, $d_a = -0.43$ mm, $d_t = 1$ mm, and $l_t = 5.6$ mm. The LMB needle has $\zeta = 23.5°$, $\zeta_b = \zeta_s = 12°$, $\theta_s = 110°$, $d_a = -0.22$ mm, $d_t = 0.8$ mm, and $l_t = 5.3$ mm. The AMB

needle has $\zeta = 23.5°$, $\zeta_b = \zeta_s = 12°$, $\theta_s = 110°$, $d_a = 0$ mm, $d_t = 0.57$ mm, and $l_t = 4.8$ mm. Finally, the HMB needle has $\zeta = 23.5°$, $\zeta_b = \zeta_s = 12°$, $\theta_s = 110°$, $d_a = 0.37$ mm, $d_t = 0.2$ mm, and $l_t = 4.0$ mm.

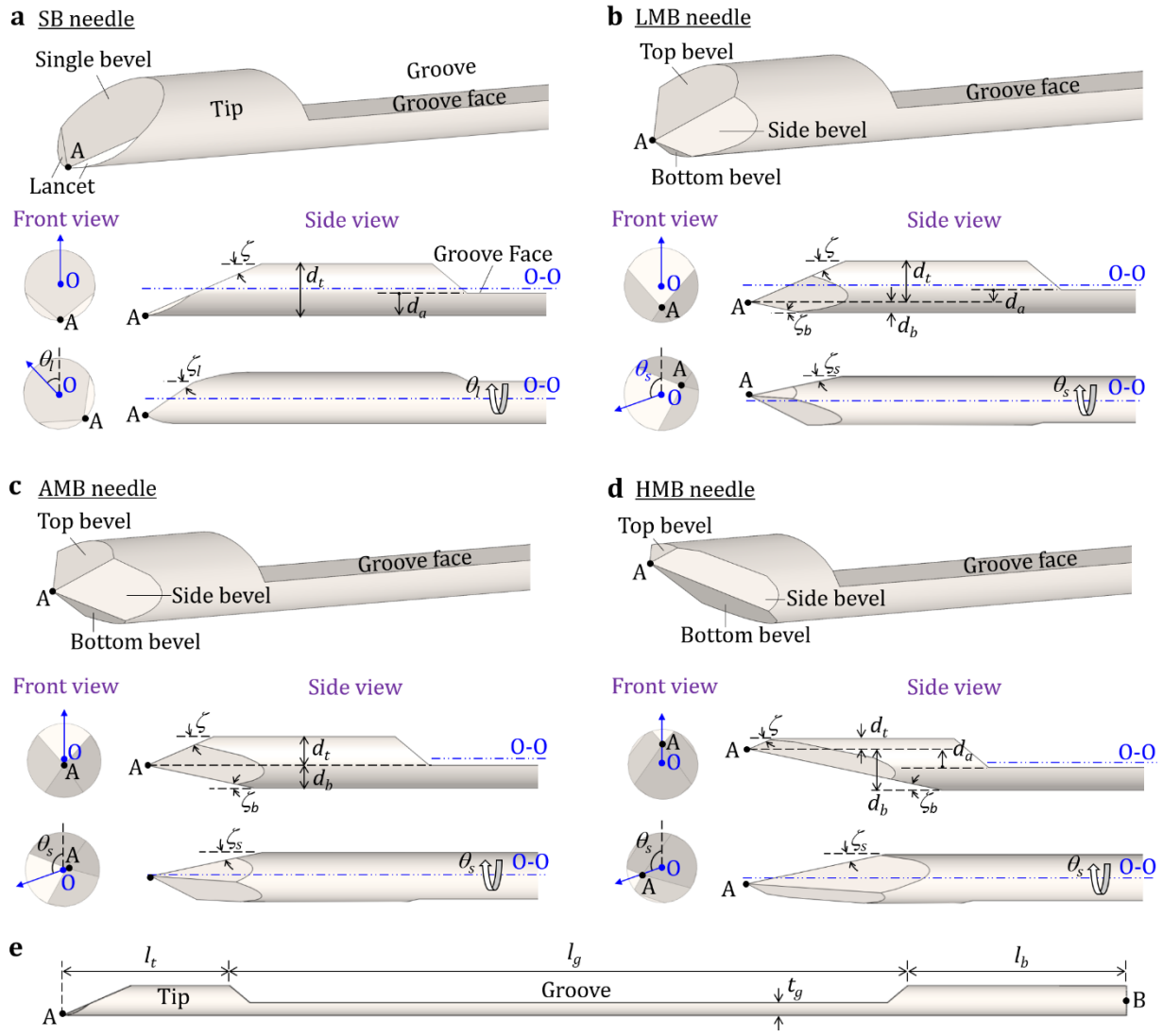

Fig. 5-1 The geometrical parameters of (a) SB, (b) LMB, (c) AMB, and (d) HMB needle tips and (e) overall needle geometry.

5.2.2 L-SPG Model Configuration

This study establishes a needle-tissue interaction modeling using the L-SPG to investigate needle deflection and tissue deformation during needle insertion in biopsy. SPG is a mesh-free method developed to effectively simulate the material separation and failure under large

deformation based on the bond-based failure criterion [88, 89]. In SPG, the simulated object is discretized into particles with the kernel function defined around a particle of interest to formulate the material constitutive model [88]. Any two neighboring particles has an interaction bond. This interaction bond is disconnected once the average effective strain and stretch ratio reach a specific threshold level and then the material separation occurs. This approach increases the material tensile stability, avoids mesh distortion under large formation, and enables more accurate modeling of the material separation and failure for SPG compared to the traditional FEA methods [88, 89]. A recent study utilized SPG to model the soft blood clot deformation and separation during tool cutting, and demonstrated to predict the cutting forces with the errors from 3-30% [87]. However, the capability of modeling the interaction between two deformable objects (needle and tissue in this study) with a large difference in material hardness has not been overcome using SPG.

In this study, the SPG method was coupled with the Lagrangian analysis to formulate the L-SPG which enabled the modeling of the deformation of needle and tissue during insertion. The Lagrangian mesh defines the needle boundary with fine spatial resolution to precisely represent the needle geometry (particularly the sharp needle tip) and bending deformation during interaction. The needle was modeled by the Lagrangian meshed elements which ensured the continuities between neighboring elements (no interaction bonds as the particles in SPG), allowing the representation of needle deflection while maintain the needle rigidity when interacting with highly deformable tissue.

The three-dimensional (3D) L-SPG model was developed in LS-DYNA (v971 R11 by LSTC, Livermore, California, USA). An example of the SB needle insertion into the soft tissue is shown in Fig. 5-2. The L-SPG model comprises three regions: tissue, needle, and cannula. Due to the symmetry of geometry, only half of tissue, needle, and cannula were modeled. Figure 5-2 (a) shows an isometric view from the symmetric plane CDEF before the needle insertion. The tissue was modeled as a cuboid CDEFGHIJ (40 mm × 8 mm × 2 mm) and discretized into the SPG particles with the particle center equally spaced by 0.4 mm in all three (*xyz*) directions, as shown in Figs. 5-2(b)-(d). The SPG kernel function was cubic B-spline function with normalized dilation parameter of 1.8 in LS-DYNA [88]. The symmetric plane CDEF was constrained in *z*-axis, allowing the deformation on the *xy* plane as shown in Fig. 5-2(c). Three outer boundary surfaces CFJG, GHIJ, and HDEI were fixed in all three (*xyz*) directions. Surfaces FEIJ (the entry surface

of the needle insertion) and CDHG (the back surface of the tissue model) were set as the free surfaces allowing the deformation in all three (*xyz*) directions as shown in Fig. 5-2(d).

Four needles (SB, LMB, AMB, and HMB needles) were modeled using the Lagrangian mesh in the L-SPG model with geometries defined in Sec. 5.2.1. A fillet radius of 0.5 mm was applied to all edges of the needle to avoid the singularity issue in numerical analysis [90]. The needle was meshed by the 10-node quadratic tetrahedron elements with the initial size of 0.2 mm element edge length using Abaqus (v 6.11 by Dassault Systèmes, Vélizy-Villacoublay, France). The meshes in regions around the sharp needle tip and groove edges were automatically refined to precisely represent the geometrical features as the close-up view shown in Fig. 5-2(b). The refined meshes of four needles were imported to the L-SPG model in LS-DYNA. The needle symmetric plane (coincident with plane CDEF) was constrained in *z*-axis while allowing the needle deflection on the *xy* plane, as shown in Fig. 5-2(c). The needle base plane, the plane through the base point B and perpendicular to the axis, as shown in Fig. 5-2(a), defined the given needle motion. This base plane was accelerated from 0 to 8 m/s along the *x*-axis in 0.75 ms, which were measured experimentally using the high-speed camera images of a needle biopsy device (details to be described in Sec. 5.2.4). Assuming a constant acceleration, the resultant needle travel of this base plane was 30 mm in *x*-axis. The constant acceleration was 1067 m/s^2.

The stationary cannula, as shown in Fig. 5-2(a), supported the needle during the insertion to stabilize the needle tip for the initial contact with the tissue and avoid needle buckling. This cannula was modeled as a rigid shell with an outer diameter of 1.27 mm and a thickness of 0.05 mm (18 gauge), as shown in Fig. 5-2(a), and fixed in all three (*xyz*) directions.

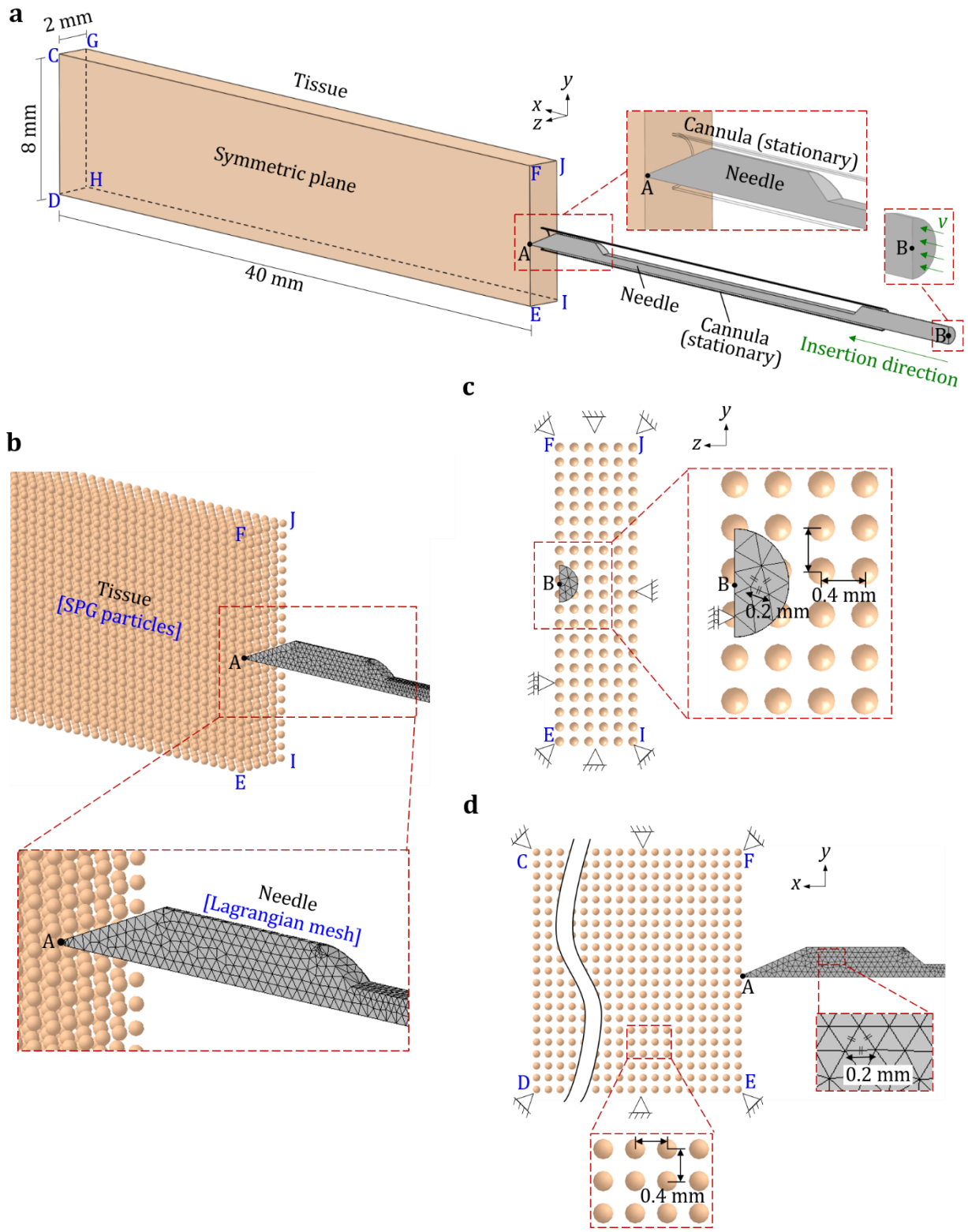

Fig. 5-2 An overview of a 3D L-SPG model of needle-tissue interaction: (a) an isometric view of the SB needle insertion into the soft tissue and the (b) isometric, (c) front (*yz* plane), and (d) side (*xy* plane) views of the SPG tissue particles and Lagrangian needle meshes.

5.2.3 Material and Contact Properties

The AISI 304 stainless steel needle was modeled as a linear elastic material with the elastic modulus E, Poisson's ratio ν, and density ρ of 193 GPa, 0.29, and 8 g/cm^3, respectively. The tissue was the soft tissue-mimicking polyvinyl chloride (PVC) material [70, 71] with Shore OOO-S hardness of 34, ν of 0.45, and ρ of 0.98 g/cm^3 (as presented in Chapter 4, details to be presented in Sec. 5.2.4). The PVC tensile and rupture properties (required for the SPG particle separation criteria) was obtained based on the ASTM D412 uniaxial tensile test, as shown in Fig. 5-3, of 16.5 mm gauge length. In the test shown in Fig. 5-3(a), the specimen was fixed to the tensile test machine (by Instron, Norwood, Massachusetts, USA) and then pulled uniaxially under a stretch rate of 500 mm/min until ruptured. Two tracking marks were added to the specimen (Fig. 5-3(b)) to optically measure the stretch during the test using the imaging tracking analysis (Kinovea, open source software) for the highly deformable PVC specimen. The measured force and stretch were utilized to calculate the true stress and true strain. Five specimens were tested to obtain the true stress vs. true strain curve up to the rupture point, as shown in Fig. 5-3(c). The Test 1 curve was removed as an outlier. The remaining four curves (Tests 2-5) were averaged as the dashed curve shown in Fig. 5-3(c).

The resultant average true stress vs. true strain curve was fitted using a power law plasticity equation: $\sigma = k\varepsilon^n$, where σ is the true stress, k is the strength coefficient, ε is the true strain, and n is the hardening coefficient. For the PVC tested in this study, k = 0.35 MPa, n = 2.75, and the root mean square error for this fitting was equal to 0.002. For the tissue separation in the L-SPG model, two adjacent SPG particles would separate when the average effective tensile strain exceeds 1.84, as shown in the tensile test rupture point of PVC in Fig. 5-3(c). To account for the strain rate dependency of the PVC during the high-speed needle insertion in biopsy, the Cowper and Symonds model [91] was used to scale the true stress with a factor of $1+(\dot{\varepsilon}/C)^{(1/p)}$, where C and p are two material constants and $\dot{\varepsilon}$ is the strain rate. In this study, the C and p were set as 0.1 ms^{-1} and 0.1, respectively, to have the best fit to the experiment results in needle deflection (details to be presented in Sec. 5.2.4). The friction coefficient μ of 0.18, as derived in Sec. 3.2.3 for the interaction between the needle and PVC phantom, was used at the contact between the needle and tissue in this study.

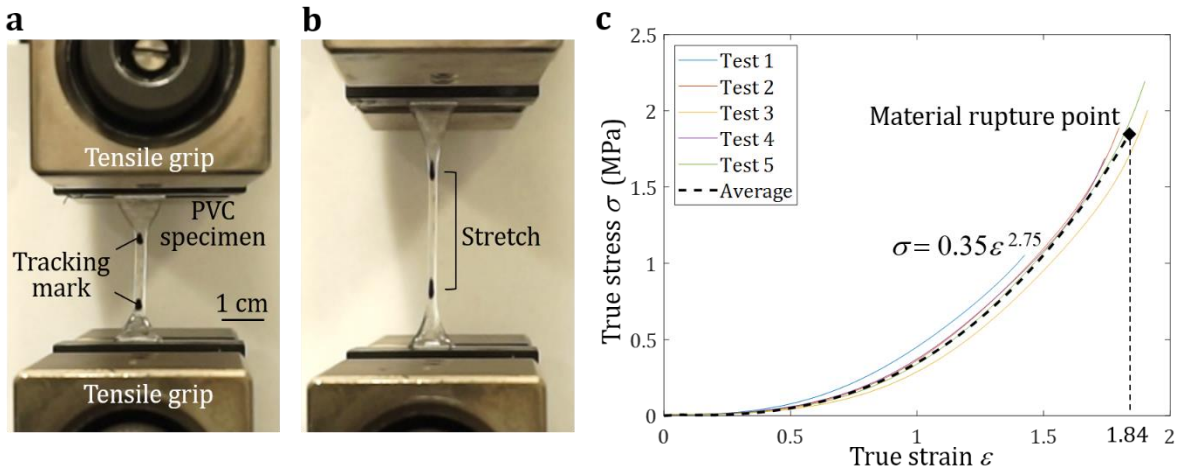

Fig. 5-3 (a) An overview of the tensile test of a PVC specimen with the tracking marks, (b) the material stretch during the test which was optically quantified, and (c) the resultant average true stress vs. strain curve.

5.2.4 L-SPG Model Verification

The L-SPG predicted deflection for SB, LMB, AMB, and HMB needles was compared with the needle deflection experimental measurements (as presented in Sec. 4.2.3) in transparent PVC phantom with Shore OOO-S hardness of 34. A spring-loaded needle biopsy device (SelectCore Variable Throw Biopsy Device by Inrad, Kentwood, Michigan, USA) was utilized. This biopsy device advanced the needle under a high constant acceleration to reach the maximal speed of 8 m/s at the end of the insertion. Positions of the needle tip before and after the insertion were captured using the high speed camera. The needle deflection was measured using the imagining analysis (Matlab by MathWorks, Natick, Massachusetts, USA).

The L-SPG model was also able to observe the tissue deformation and contact with the deflected needle. The shape of tissue within the needle groove was qualitatively compared to the sampling length of ex-vivo chicken breast tissue in trucut biopsy (as presented in Section 4.2.4).

5.3 Results

5.3.1 Needle Deflection

Figure 5-4 shows the L-SPG predicted needle deflection δ_p vs. the experimental measured needle deflection δ for the SB, LMB, AMB, and HMB needles. The error bars represented the standard deviations of 10 insertion tests. Figure 5-4 also presents the L-SPG modeling results of the needle and tissue displacement along the *y*-axis before (top) and after (bottom) the insertion. The dashed lines represent the path without needle deflection. Experimental images of the needle tip before (top) and after (bottom) the insertion into the PVC tissue phantom (same material used in the L-SPG model) are also shown in Fig. 5-4. The top images illustrate the location of tip point A before the insertion. The bottom images show the needle with deflection after the insertion into the tissue. The δ_p in L-SPG was defined as the *y*-displacement at the needle tip point A.

The δ_p of the SB, LMB, AMB, and HMB needles were –1.15 (downward), 0.12 (upward), 0.28, and 1.03 mm, respectively (vs. –1.14, 0.15, 0.24, and 1.71 mm for δ, respectively). The L-SPG model demonstrated a reasonably good prediction, with the δ_p and δ discrepancy of 0.01, 0.03, and 0.04 mm for the SB, LMB, and AMB needles, respectively, as shown in Fig. 5-4. The error for L-SPG model prediction of HMB needle was the largest among four needles. The model underpredicted the upward deflection of HMB needle by 0.68 mm. This was possibly due to the relatively coarse SPG particle density, which led to computational errors at the contact between the tissue and HMB needle, and therefore the upward bottom and side bevel face forces and the resultant deflection were underpredicted (details to be further discussed in Sec. 5.3.3).

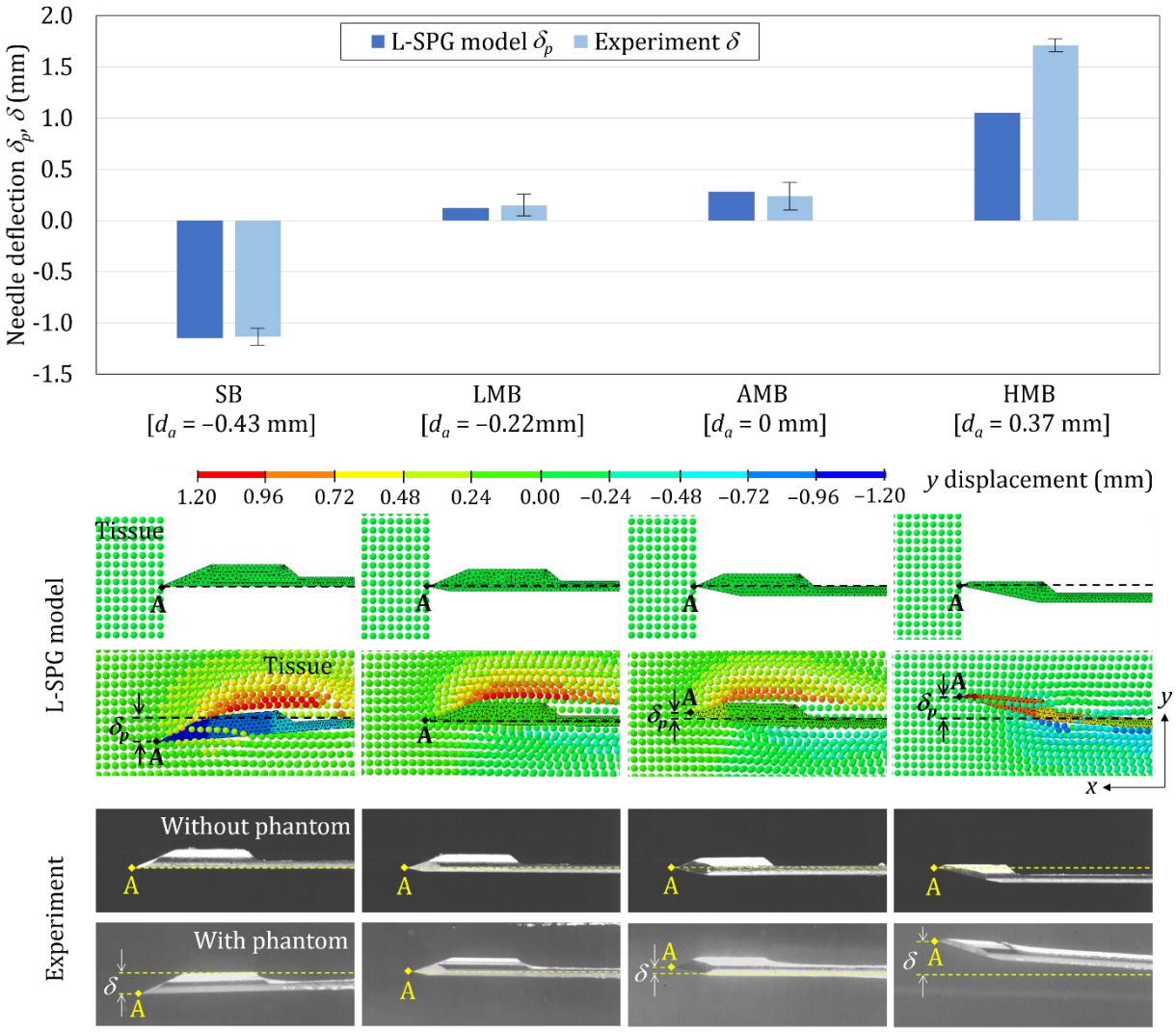

Fig. 5-4 The L-SPG predicted needle deflection δ_p vs. the experimental measured needle deflection δ (error bars representing the standard deviations) for the SB, LMB, AMB, and HMB needles. The L-SPG model and experimental images of the needle tip before (top) and after (bottom) the insertion into the tissue phantom are also presented.

5.3.2 Tissue Deformation and Contact with Needle

Figure 5-5 shows the tissue deformation and contact with SB, LMB, AMB, and HMB needles in the L-SPG model at the end of the insertion. The mean strain in L-SPG modeling, denoted as strain hereafter, was calculated based on the displacement of the tissue and needle to represent the resultant deformation. The SPG particles highlighted by the pink circles illustrate the shape of the tissue within the needle groove as shown in Fig. 5-5. The L-SPG modeling results of

needle insertion to PVC were qualitatively compared with the experimentally measured tissue sampling length l_s (in the ex-vivo chicken breast tissue) for four needles (SB, LMB, AMB, and HMB) as shown in Fig. 5-6.

Results show that the shape of tissue within the needle groove correlated with the l_s for all four needles. For the SB (d_a = –0.43 mm) and LMB (d_a = –0.22 mm) needles, as shown in Figs. 5-5(a) and (b), respectively, the tissue was cut and separated below the groove face which allowed the rebounded tissue to fill and contact the groove (details to be discussed in Sec. 5.3.3). Such tissue contact enabled the long (over 12 mm) tissue samples in biopsy as shown in Fig. 5-5. The AMB needle (d_a = 0 mm), compared to the SB and LMB needles, had a higher tissue separation point relative to the groove face, leading to almost no tissue contact inside the groove as shown in Fig. 5-6(c). This was reflected as a shorter l_s compared to the SB and LMB needles as shown in Fig. 5-5. The HMB needle (d_a = 0.37 mm) had the highest tissue separation point among four needles. The high d_a increased the gap between the tissue and the needle groove face (as shown in Fig. 5-6(d)) and resulted the lowest l_s (as shown in Fig. 5-5) compared to the other three needles.

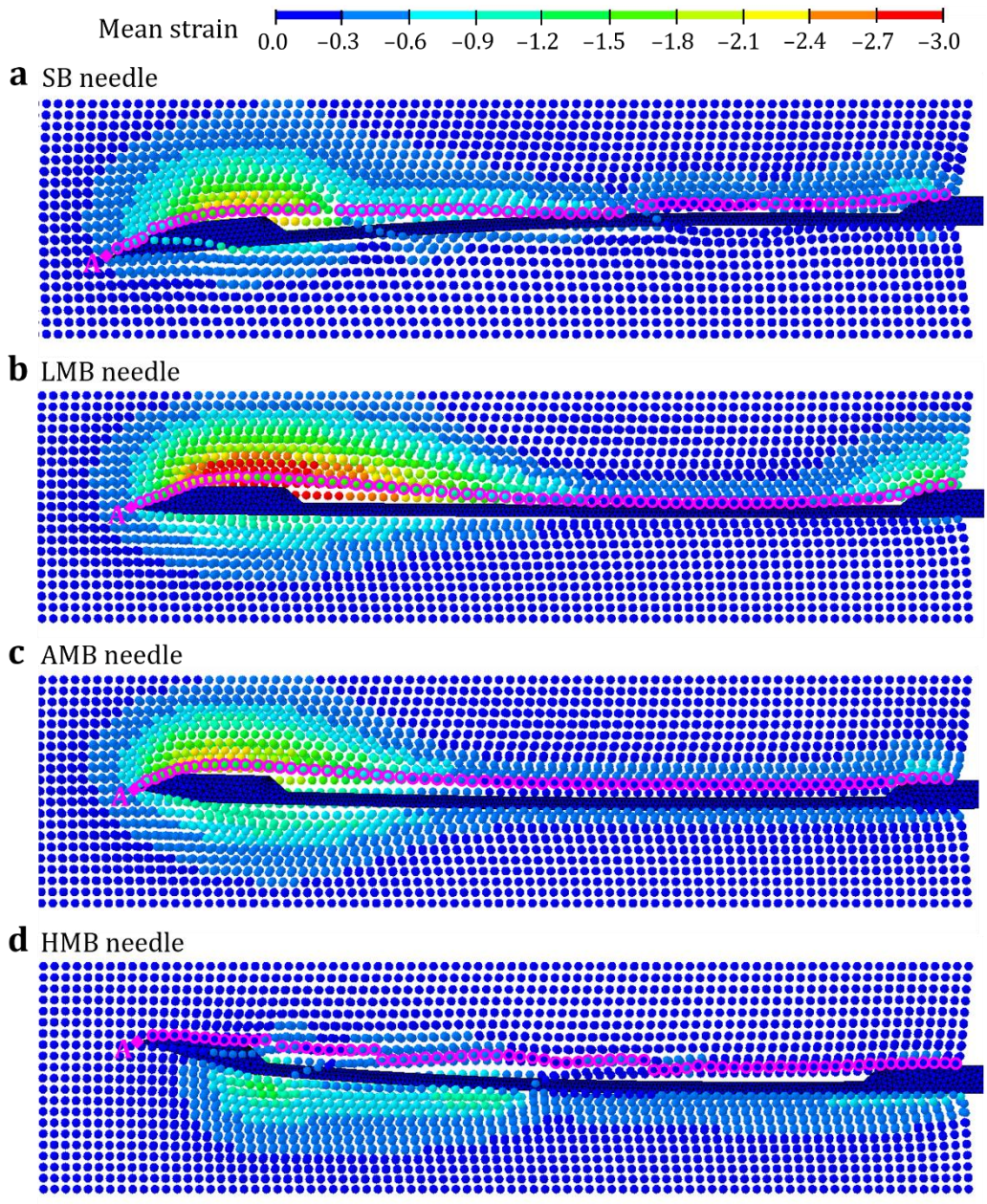

Fig. 5-5 The tissue deformation and contact with SB, LMB, AMB, and HMB needles in the L-SPG model at the end of the insertion.

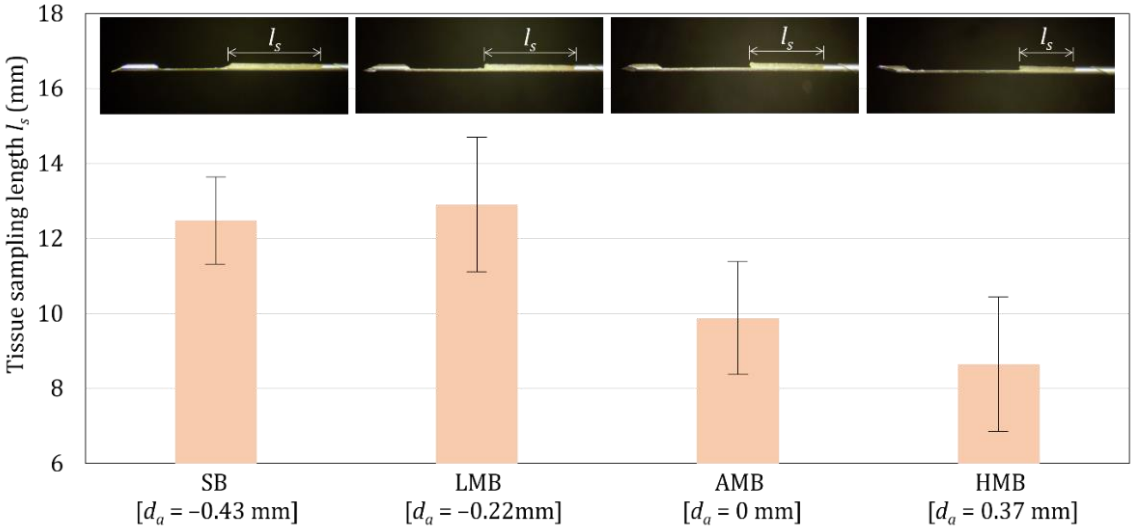

Fig. 5-6 The experimental results of tissue sampling length l_s and the microcopy images of tissue samples for the SB, LMB, AMB, and HMB needles (the error bar representing the standard deviation of 10 tests).

5.3.3 Needle-Tissue Interaction

The needle-tissue interactions for the SB, LMB, AMB, and HMB needles in the L-SPG model are illustrated in Figs. 5-7 and 5-8. Figure 5-7 presents the L-SPG model predicted displacement of the needle and tissue in the *y*-axis (the direction of needle deflection) during the insertion. Figure 5-7(a) shows the side view of symmetric plane CDEF with the undisplaced SB needle (as an example) and tissue at the needle insertion length L = 0 mm. At this state, the tissue were undeformed with zero strain as shown in Fig. 5-8(a).

Figure 5-7(b) shows the distribution of displacement during the insertion of SB needle at L = 4.8 and 30 mm. At L = 4.8 mm, the tissue displacements on the top and bottom of the needle tip were about 0.80 and 0 mm, respectively. At this state, the δ_p was almost equal to 0 mm and the needle was mostly supported by the cannula without deflection. The tissue was cut and separated at the needle tip point A. The separated tissue on the top of the needle was pushed upward, resulting in a high compressive strain of about –1.2 around the needle tip, as shown in Fig. 5-8(b). The bottom separated tissue was almost undeformed with zero strain because the point A was at the bottom of the needle tip surface. At L = 30 mm, as shown in Fig. 5-7(b), the needle was significantly deflected downward with the δ_p of –1.15 mm. The tissue displacements at the top of

the needle tip and around the groove were about 1.20 and 0.60 mm, respectively. The tissue displacement at the bottom of the needle tip was about –0.24 mm. The tissue in front of the needle was greatly deformed with a highly concentrated compressive strain of about –1.8 at the top of the needle tip as shown in Fig. 5-8(b). Such tissue deformation exerted a high force on the bevel face of the needle tip, inducing over 1 mm downward deflection of the needle. Once the separated tissue reached the groove opening, it rebounded from its compression state and filled in the groove. The SB needle had the $d_a < 0$ which allowed the rebounded tissue to contact the groove face as illustrated by the highlighted tissue shape (SPG particles marked by pink circle) within the groove in Figs. 5-7(b) and 5-8(b). The filled tissue still remained at the slight compression state with the compressive stain of about –0.6, generating the tissue pressure on the groove face and further aggravating the downward needle deflection. Such contact enabled the outer cannula to acquire a long tissue sample in biopsy as observed in the tissue sampling experiment (Sec. 5.3.2). The resultant δ_p also matched the experimentally measured needle deflection (Sec. 5.3.1). The deflected needle also slightly pushed the tissue at the bottom of the needle downward with the compressive strain of about –0.6.

In the L-SPG model, it was observed that a few separated SPG particle lines crossed through the needle (particle penetration) as marked by M_1, M_1, and M_3 in Figs. 5-7(b) and 5-8(b). These were likely due to the relatively coarse SPG particle density compared to the needle meshes, which caused some computational errors at the contact to have some residual SPG particles still connected to and not fully separated from the separated tissue during needle insertion.

Figure 5-7(c) shows the distribution of displacement during the insertion of LMB needle. At L = 4.8 mm, similar to the SB needle, the δ_p was 0 mm and the tissue y-displacement on the top of the needle tip was about 0.80 mm. The tissue y-displacement at the bottom of the needle tip was increased to about –0.24 mm (vs. 0 mm for the SB needle). This is close to the d_a = –0.22 mm. The multi-bevel LMB needle, compared to the SB needle, had the bottom and side bevel facets deforming and pushing the tissue downward (negative y-displacement) during the insertion. This led a compressive strain of about –0.45 at the bottom of the needle tip, generating the upward face forces to stabilize the needle tip as shown in Fig. 5-8(c). At L = 30 mm, the needle deflection was much reduced compared to that of SB needle with the δ_p of 0.12 mm (Fig. 5-7(c)), as a result of the multi-bevel facets at the needle tip. The tissue displacement on the top of the needle tip and around the groove were about 1.20 and 0.24 mm, respectively. The tissue displacement at the

bottom of the needle was about –0.48 mm. Since the LMB needle also had the $d_a < 0$, the tissue also rebounded to contact the groove face as illustrated by the highlighted tissue shape in Figs. 5-7(c) and 5-8(c). The filled tissue was also at the compression state with the compressive strain of about –0.6, generating the tissue pressure on the groove face as shown in Fig. 5-8(c). However, the upward face forces on the bottom and side bevel facets provided the critical support to balance the downward needle bending moments caused by the top bevel face force and the tissue pressure on the groove face. This enabled the LMB needle to have low needle deflection and high tissue sampling as the experimental results shown in Secs. 5.3.1 and 5.3.2.

Figure 5-7(d) show the insertion of AMB needle (d_a = 0 mm) with the resultant displacement. At L = 4.8 mm, compared to the LMB needle, the tissue displacements on the top of the needle tip was reduced to about 0.6 mm while the tissue displacement at the bottom of the needle tip was increased to about –0.48 mm. This was because the AMB needle had the larger bottom and side bevel facets than those of the LMB needle, further deforming the tissue downward during the insertion. At L = 30 mm, the upward needle deflection was increased compared to that of SB needle with the δ_p of 0.28 mm. The tissue displacement on the top of the needle tip and around the groove were about 0.84 and 0.36 mm, respectively. The tissue displacement at the bottom of the needle was about –0.60 mm. Compared to the LMB needle, as shown in Fig. 5-8(d), the compressive strain at the bottom of the needle tip was increased to about –0.9 which caused larger upward face forces to deflect the needle upward. The AMB needle had the higher tissue separation point relative to the groove face (d_a = 0 mm) compared to the SB and LMB needles, leading to almost no tissue contact inside the groove as the highlighted tissue shape shown in Figs. 5-7(d) and 5-8(d). At this state, tissue around the groove had mostly rebounded back to the undeformed state with the strain of 0. These phenomena explained the results of the larger upward deflection and shorter tissue sampling length compared to those of LMB needle as observed in the experiments.

Figure 5-7(e) show the insertion of HMB needle (d_a = 0.37 mm). At L = 4.8 mm, compared to the AMB needle, the tissue displacement at the bottom of the needle tip was much increased to about –0.60 mm. The tissue displacement on the top of the needle tip was small with about 0.10 mm. Since the HMB needle had the bottom bevel facet which was much larger than the other three facets, the separated tissue was mostly deformed and pushed downward. This resulted in a concentrated compressive strain of about –0.75 at the bottom of the needle tip as shown in Fig. 5-

8(e). At L = 30 mm, the needle was significantly deflected upward with the δ_p of 1.03 mm (Fig. 5-7(e)). The tissue displacements on the top of the needle tip and around the groove were all small with almost 0 displacement. The tissue displacement at the bottom of the needle was about –0.72 mm. At this state, the tissue at the bottom of the needle was greatly deformed with the compressive strain of about –1.20, as shown in Fig. 5-8(e). This generated large force on the bottom bevel facet of the HMB needle and significantly deflect the needle upward. The HMB needle had the highest tissue separation point (d_a = 0.37 mm) among four needles. This resulted in no tissue contact with the groove face and further increased the gap between the tissue and the groove compared to that of AMB needle, as the highlighted tissue shape shown in Figs. 5-7(e) and 5-8(e). Therefore, the HMB needle had the largest upward deflection and shortest tissue sampling length among four needles as observed in the experiments. However, the δ_p was underpredicted compared to the experimentally measured deflection. This was due to the computational errors at the contact as marked by the M_1, M_2, and M_3 regions in Figs. 5-7(e) and 5-8(e) with particle penetration issue, similar to that in the SB needle insertion. In the HMB needle, it was observed that the affecting region of M_3 (close to the needle tip) was large which led to reduced tissue contact with the bottom and side bevel facets at the HMB needle tip. This was reflected in the tissue at the bottom of the needle tip which was almost undeformed (almost no contact at the region close to the needle tip point A). Therefore, the upward face forces and the resultant needle deflection for the HMB needle in the L-SPG model were underpredicted.

In summary, the L-SPG model demonstrated the capability of simultaneously modeling the needle deflection and tissue deformation during needle insertion. The L-SPG predicted correlation between the needle tip type vs. the resultant needle deflection and tissue sampling length had been shown to match the trend observed in the experimental results. This L-SPG model also revealed the needle-tissue interaction for the SB, LMB, AMB, and HMB needles to support the experimental findings as presented in Chapter 4.

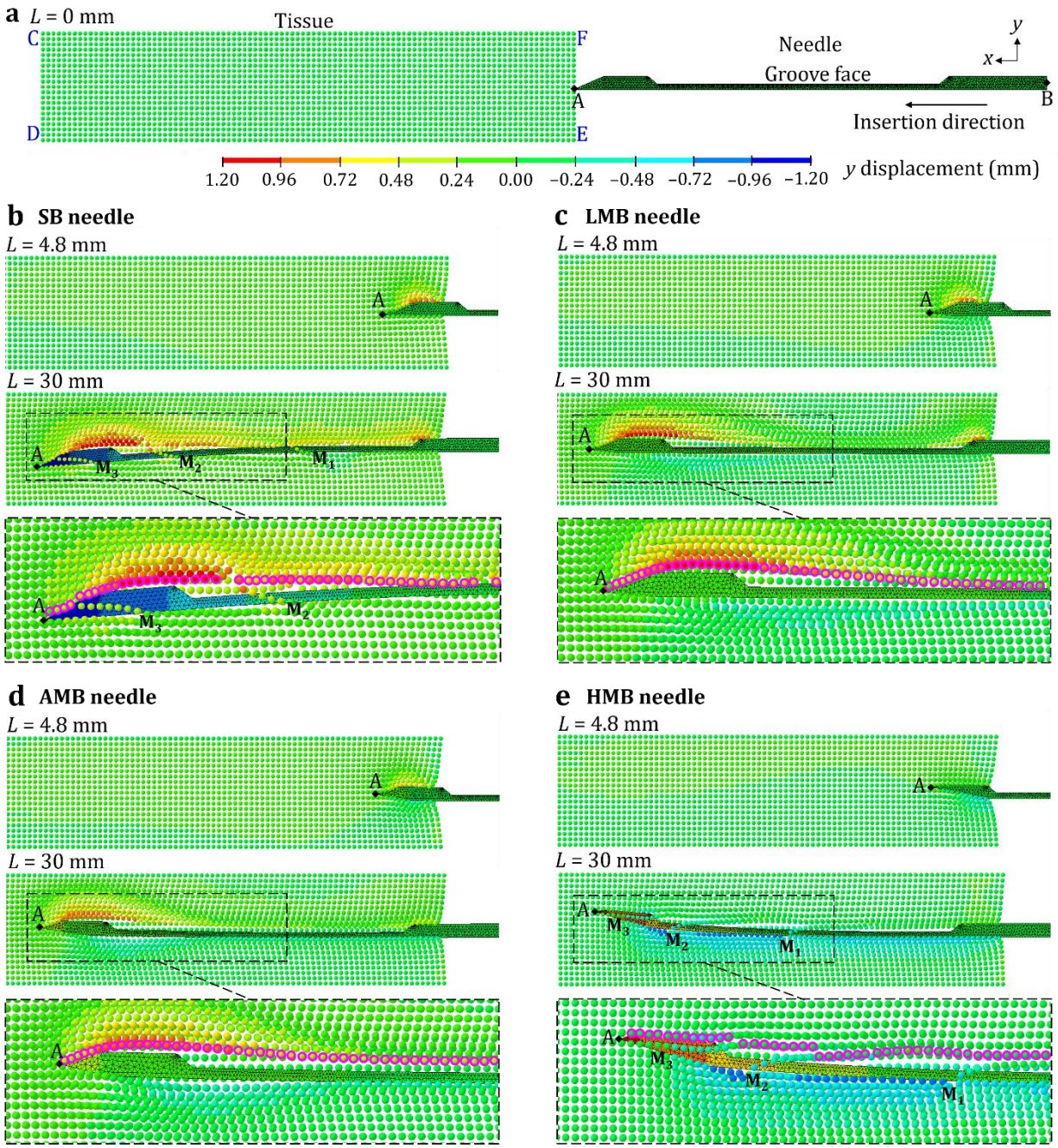

Fig. 5-7 The L-SPG displacement results of the needle and tissue: (a) the undisplaced SB needle and the tissue before the insertion and the (b) SB, (c) LMB, (d) AMB, and (e) HMB needles during the insertion.

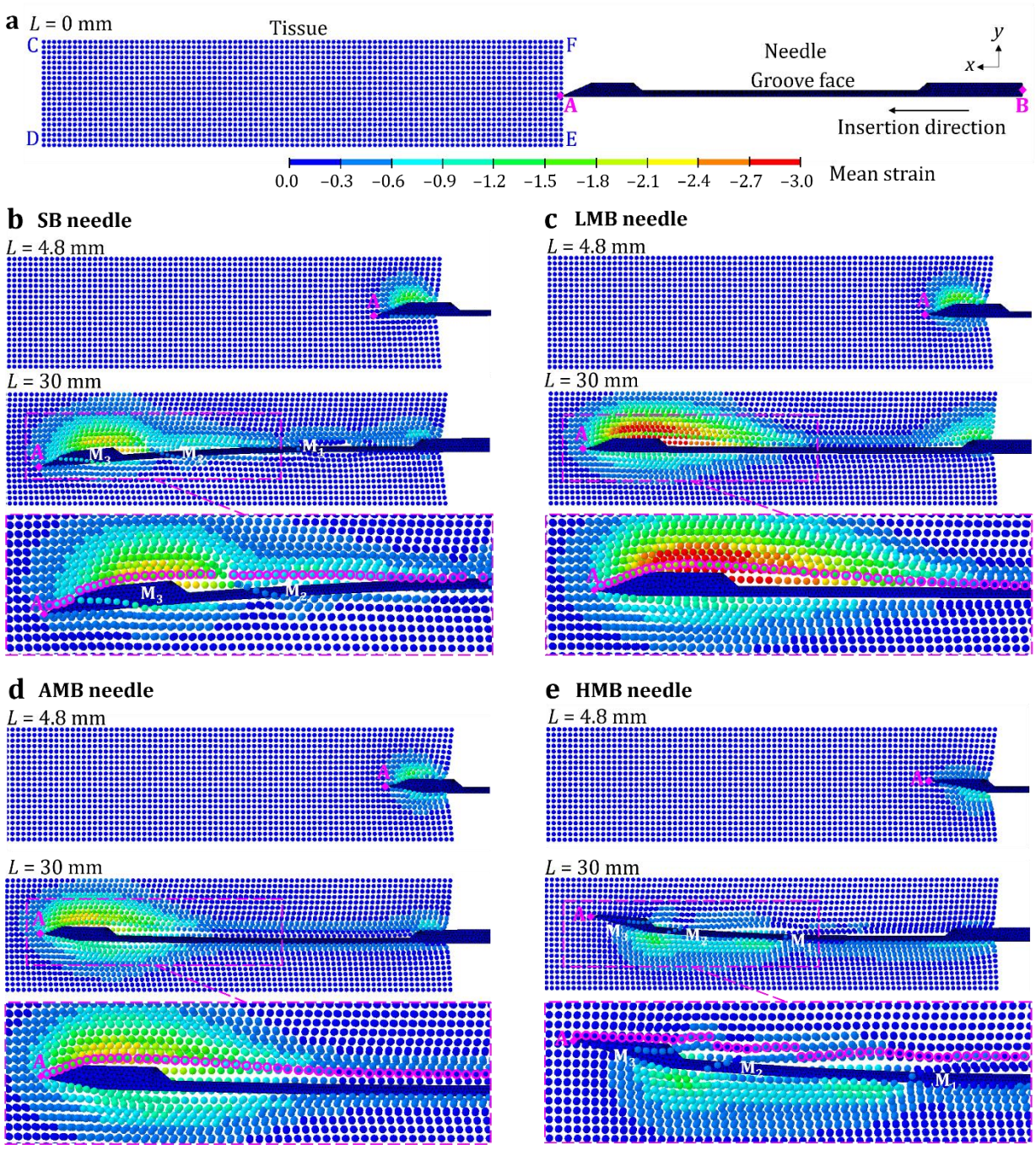

Fig. 5-8 The L-SPG stain results of the needle and tissue: (a) the undisplaced SB needle and the tissue before the insertion and the (b) SB, (c) LMB, (d) AMB, and (e) HMB needles during the insertion.

5.4 Conclusions

This study established the L-SPG modeling of needle-tissue interaction to simultaneously predict the needle deflection and tissue deformation. The L-SPG model demonstrated a reasonably good prediction on the correlation of the needle tip type (SB, LMB, AMB, and HMB needles) vs. the resultant needle deflection and tissue sampling length. This model had also revealed the needle-tissue interaction for the SB, LMB, AMB, and HMB needles during the insertion to support the experimental findings. Future work will focus on formulating a better material model to account for the hyperelastic behavior of the real tissue, and the deformation and rupture under high strain rate in biopsy. The L-SPG mesh density including the needle Lagrangian elements and tissue SPG particles will also be adjusted to more accurately represent the tissue deformation at the contact with the needle and assess the convergence in numerical analysis. The L-SPG modeling methodology developed in this study can have broad applications for various clinical procedures to provide the insights of the interaction between the surgical tool and soft tissues. This L-SPG model can also serve as an evaluation platform to guide the development of needle technology enabling minimal needle deflection and tissue deformation.

Chapter 6: Conclusions and Future Works

6.1 Conclusions

This dissertation studied the needle-tissue interaction mechanics to establish the scientific and technological foundations for accurate needle insertion and tissue sampling in biopsy. First, the effect of the needle insertion motion on tissue deformation and organ displacement was investigated. Second, the relationship between the needle tip geometry and the resultant needle deflection and tissue sampling length was studied. The needle design criteria enabling low needle deflection and high tissue sampling was identified. Last, the predictive needle-tissue interaction modeling of needle deflection and tissue deformation was established.

The original discoveries and key conclusions of this dissertation can be summarized as follows:

(1) Current needle biopsy procedure can be divided into two Phases: 1) low-speed pre-insertion to position the needle to be close to the targeted sampling site and 2) high-speed firing for tissue sampling of the diseased site. The traditional needle delivery process during Phase I often leads to large tissue deformation and organ displacement. Furthermore, the currently available trucut needle devices can yield long and adequate tissue sample but often induce significant deflection during Phase II. These issues causes variances in the targeted and actual locations of the sampled tissue core, leading to lesion missampling or undersampling in biopsy.

(2) A MPI needle insertion with the incremental needle-cannula motion and the harpoon-shape notches at the needle tip demonstrated the benefits to reduce tissue deformation and displacement compared to the traditional direct needle insertion (in Phase I). The opposite

incremental motions of needle-cannula balanced forces and reduced local deformation and global prostate displacement during the insertion. Notches at the needle tip provided the critical tissue anchoring and support to further reduce the displacements of surrounding tissue.

(3) The tissue separation location at the needle tip relative to the needle groove face was revealed to be a key factor affecting both needle deflection and tissue sampling length (in Phase II). By varying the tissue separation location and creating a multi-bevel needle tip geometry, the bending moments induced by the insertion forces could be altered to reduce the needle deflection. However, the tissue separation location also affected the tissue contact inside the needle groove, potentially reducing the tissue sampling length.

(4) Two critical design criteria for ideal needle in trucut biopsy: 1) the tissue separation point should be below the needle groove face to ensure high tissue sampling and 2) the multi-bevel needle tip geometry, which can have bevel faces generating the upward forces while maintaining the low separation point, will be needed to balance the bending moments during the insertion and enable low needle deflection. A new trucut biopsy needle (LMB needle) achieving both criteria had demonstrated the lowest needle deflection and long tissue sampling compared to the traditional and other multi-bevel needles (all with the same groove geometry). The capabilities of improved needle deployment accuracy and tissue sampling on human tissue for this new needle biopsy device were also confirmed.

(5) The new L-SPG methodology demonstrated the capability of simultaneously modeling the needle deflection and tissue deformation during needle insertion. The L-SPG model demonstrated a reasonably good prediction on the correlation of the needle tip type vs. the resultant needle deflection and tissue sampling length, matching the trend observed in the experimental results. This model also revealed the needle-tissue interaction for the various needle geometries during the insertion to support the experimental findings in this dissertation.

Results from this dissertation can fulfill three identified research gaps (also presented in Section 1.2): 1) needle biopsy technology enabling low tissue deformation and low needle deflection and potentially feasible for clinical use, 2) understanding of needle targeting accuracy vs. tissue sampling volume in trucut biopsy, and 3) a method to predict needle deflection and tissue

deformation during needle insertion. Knowledge established here can also help the clinicians and researchers to gain insights of needle-tissue interaction to improve the needle biopsy performance as well as other clinical procedures requiring accurate needle deployment.

6.2 Major Contributions

This dissertation has established the scientific and technological foundations for accurate needle insertion and tissue sampling in biopsy. The major contributions to the research areas of focus (as presented in Section 1.2) relevant to the scope of this dissertation are:

(1) *Understanding of needle insertion mechanics in biopsy:* This dissertation provided the knowledge of the effect of needle insertion motion on tissue deformation (Chapter 2) and needle tip geometry on needle deflection and tissue sampling (Chapters 3 and 4). In Chapter 2, it was found that by having the relative opposite incremental motions of needle and cannula, the deformation during the insertion could be canceled to reduce the organ displacement in front of the needle. In Chapters 3 and 4, it was found that the by having the multi-bevel needle tip geometry with low tissue separation point, the needle deflection during the insertion could be reduced while maintaining the adequate tissue sampling. These basic findings are aimed to inspire the researchers in the field to develop the more effective, efficient, and feasible needle technology for biopsy procedure.

(2) *Experimental methods to study needle deflection and tissue deformation during needle insertion:* This dissertation established the experimental approach using the transparent tissue-mimicking phantom to optically quantify the needle deflection and tissue deformation by the imagining analysis. The specially designed particle-embedded phantom with the DIC and particle tracking analysis provided the qualitative visualization and quantitative analysis of tissue deformation and displacement (Chapter 2). The transparent phantom with the gradient material property enabled a clear observation of the location of the needle tip with needle deflection with different levels of hardness (Chapters 3 and 4). The developed methods could be exploited as an evaluation platform allowing researchers to investigate the performance of various needle and surgical tools.

(3) *Innovative needle biopsy technologies enabling accurate needle insertion and tissue sampling*: Based on the understanding of needle-tissue interaction, two innovative needle designs had been developed for accurate needle insertion and tissue sampling in this dissertation. The first was the MPI needle insertion reducing tissue deformation and organ displacement (Chapter 2). The second was the LMB needle tip geometry enabling low needle deflection and high tissue sampling in biopsy (Chapter 4). Since these innovations are established based on the currently used biopsy needle device, they are ready to be further developed for real clinical use (e.g. LMB trucut needle device in Chapter 4) or combined into a new biopsy system, aiming to improve the needle deployment accuracy while maintain the adequate tissue sampling for accurate cancer diagnosis in biopsy.

(4) *Needle-tissue interaction modeling methodologies to predict needle insertion performance:* This dissertation studied the numerical modeling methods to understand the needle-tissue interaction during needle insertion. A Coupled Eulerian-Lagrangian (CEL) model was developed to effectively model the tissue deformation and the resultant tissue stresses on the rigid needle to gain insights of the needle-tissue interaction at the contact (Chapter 3). The tissue deformation and contact with the needle in CEL revealed that the tissue separation location at the needle tip affected both needle deflection and tissue sampling length. The model using the Lagrangian analysis coupled with smoothed particle Galerkin method (L-SPG) demonstrated the capability for simultaneously modeling of the needle deflection and tissue deformation, which were coupled with the needle-tissue interaction phenomenon during the needle insertion (Chapter 5). This L-SPG model demonstrated a reasonably good prediction on the correlation of the needle tip type vs. the resultant needle deflection and tissue sampling length, matching the trend observed in experimental measurements. These modeling methods will allow the researchers in this field to not only reveal the true needle-tissue interaction mechanics but also severe as the effective simulation platforms for validations of new needle or surgical tools.

6.3 Future Work

The experimental setup, modeling methodologies, and needle biopsy technologies established in this dissertation could be further improved and extended in the following directions:

(1) For proposed needle biopsy technologies (MPI needle insertion and LMB needle tip geometry), further assessments will be needed to make sure they can be implemented into the current hand-held biopsy device and are clinically feasible. For example, a mechanical-driven mechanism to generate the MPI incremental insertion motion (instead of electricity-driven) will be desired for hand-held use while maintaining the reasonable device costs for adoption. Since the LMB needle has been implemented into a commercial biopsy device for testing in this dissertation, the next step is to conduct the human clinical trials to confirm the clinical feasibility and safety of LMB needled device.

(2) The MPI needle insertion and the LMB needle tip geometry will be combined into a new biopsy system enabling optimal tissue sampling in biopsy. For example, the notches can be added onto the LMB needle tip geometry as the final needle tip design. In the envisioned biopsy procedure, the needle and cannula will be pre-inserted using the MPI insertion to reduce tissue deformation, and fired with a predictable straight insertion path as the result of LMB needle tip geometry. Further development and assessments will be needed for such combination to establish a new needle biopsy system.

(3) For the CEL and L-SPG models, a more accurate material model will be formulated to account for the hyperelastic behavior and inhomogeneity of the real tissue, and the deformation and rupture under high strain rate in biopsy. The tissue model with various tissue/organ materials and the anatomically accurate geometries can be constructed to study the needle insertion of the realistic clinical procedures where the needle is required to penetrate through multiple tissues. For L-SPG model, a future study on the mesh density, including the needle Lagrangian elements and tissue SPG particles, and the convergence of numerical analysis will be required to more accurately model the tissue deformation at the contact with the needle.

(4) The methodology and findings in this dissertation can be further extended to be applied for the researches of medical robotics to provide the insights of needle-tissue interaction and

develop the precision needle guidance system with the predictable insertion path and low tissue deformation to improve needle deployment accuracy.

References

[1] I.G. Schoots, M.J. Roobol, D. Nieboer, C.H. Bangma, E.W. Steyerberg, M.G.M. Hunink, Magnetic Resonance Imaging–targeted Biopsy May Enhance the Diagnostic Accuracy of Significant Prostate Cancer Detection Compared to Standard Transrectal Ultrasound-guided Biopsy: A Systematic Review and Meta-analysis, Eur. Urol. 68 (2015) 438–450. doi:10.1016/j.eururo.2014.11.037.

[2] J.S. Wu, J.D. Goldsmith, P.J. Horwich, S.K. Shetty, M.G. Hochman, Bone and Soft-Tissue Lesions: What Factors Affect Diagnostic Yield of Image-guided Core-Needle Biopsy?, Radiology. 248 (2008) 962–970. doi:10.1148/radiol.2483071742.

[3] L. Maier-Hein, A. Tekbas, A. Seitel, F. Pianka, S.A. Müller, S. Satzl, S. Schawo, B. Radeleff, R. Tetzlaff, A.M. Franz, B.P. Müller-Stich, I. Wolf, H.-U. Kauczor, B.M. Schmied, H.-P. Meinzer, In vivo accuracy assessment of a needle-based navigation system for CT-guided radiofrequency ablation of the liver, Med. Phys. 35 (2008) 5385–5396. doi:10.1118/1.3002315.

[4] N. Abolhassani, R. V. Patel, F. Ayazi, Minimization of needle deflection in robot-assisted percutaneous therapy, Int. J. Med. Robot. Comput. Assist. Surg. 3 (2007) 140–148. doi:10.1002/rcs.136.

[5] A.G. Anastasiadis, M.P. Lichy, U. Nagele, M.A. Kuczyk, A.S. Merseburger, J. Hennenlotter, S. Corvin, K. Sievert, C.D. Claussen, A. Stenzl, H. Schlemmer, MRI-Guided Biopsy of the Prostate Increases Diagnostic Performance in Men with Elevated or Increasing PSA Levels after Previous Negative TRUS Biopsies, Eur. Urol. 50 (2006) 738–749. doi:10.1016/j.eururo.2006.03.007.

[6] C. Senft, A. Bink, K. Franz, H. Vatter, T. Gasser, V. Seifert, Intraoperative MRI guidance and extent of resection in glioma surgery: a randomised, controlled trial, Lancet Oncol. 12

(2011) 997–1003. doi:10.1016/S1470-2045(11)70196-6.

[7] T.H. Kuru, M.C. Roethke, J. Seidenader, T. Simpfendörfer, S. Boxler, K. Alammar, P. Rieker, V.I. Popeneciu, W. Roth, S. Pahernik, H.-P. Schlemmer, M. Hohenfellner, B.A. Hadaschik, Critical Evaluation of Magnetic Resonance Imaging Targeted, Transrectal Ultrasound Guided Transperineal Fusion Biopsy for Detection of Prostate Cancer, J. Urol. 190 (2013) 1380–1386. doi:10.1016/j.juro.2013.04.043.

[8] M.M. Siddiqui, S. Rais-Bahrami, B. Turkbey, A.K. George, J. Rothwax, N. Shakir, C. Okoro, D. Raskolnikov, H.L. Parnes, W.M. Linehan, M.J. Merino, R.M. Simon, P.L. Choyke, B.J. Wood, P.A. Pinto, Comparison of MR/Ultrasound Fusion–Guided Biopsy With Ultrasound-Guided Biopsy for the Diagnosis of Prostate Cancer, JAMA. 313 (2015) 390. doi:10.1001/jama.2014.17942.

[9] N. Abi-Jaoudeh, J. Kruecker, S. Kadoury, H. Kobeiter, A.M. Venkatesan, E. Levy, B.J. Wood, Multimodality Image Fusion–Guided Procedures: Technique, Accuracy, and Applications, Cardiovasc. Intervent. Radiol. 35 (2012) 986–998. doi:10.1007/s00270-012-0446-5.

[10] C. Ewertsen, B. Henriksen, S. Torp-Pedersen, M. Bachmann Nielsen, Characterization by Biopsy or CEUS of Liver Lesions Guided by Image Fusion between Ultrasonography and CT, PET/CT or MRI, Ultraschall Der Medizin - Eur. J. Ultrasound. 32 (2011) 191–197. doi:10.1055/s-0029-1245921.

[11] S. Nakano, M. Yoshida, K. Fujii, K. Yorozuya, Y. Mouri, J. Kousaka, T. Fukutomi, J. Kimura, T. Ishiguchi, K. Ohno, T. Mizumoto, M. Harao, Fusion of MRI and Sonography Image for Breast Cancer Evaluation Using Real-time Virtual Sonography with Magnetic Navigation: First Experience, Jpn. J. Clin. Oncol. 39 (2009) 552–559. doi:10.1093/jjco/hyp087.

[12] H.J. Park, M.W. Lee, M.H. Lee, J. Hwang, T.W. Kang, S. Lim, H. Rhim, H.K. Lim, Fusion Imaging-Guided Percutaneous Biopsy of Focal Hepatic Lesions With Poor Conspicuity on Conventional Sonography, J. Ultrasound Med. 32 (2013) 1557–1564. doi:10.7863/ultra.32.9.1557.

[13] G.A. Sonn, D.J. Margolis, L.S. Marks, Target detection: Magnetic resonance imaging-ultrasound fusion-guided prostate biopsy, Urol. Oncol. Semin. Orig. Investig. 32 (2014) 903–911. doi:10.1016/j.urolonc.2013.08.006.

[14] J.D. Le, S. Stephenson, M. Brugger, D.Y. Lu, P. Lieu, G.A. Sonn, S. Natarajan, F.J. Dorey, J. Huang, D.J.A. Margolis, R.E. Reiter, L.S. Marks, Magnetic Resonance Imaging-Ultrasound Fusion Biopsy for Prediction of Final Prostate Pathology, J. Urol. 192 (2014) 1367–1373. doi:10.1016/j.juro.2014.04.094.

[15] M. Valerio, I. Donaldson, M. Emberton, B. Ehdaie, B.A. Hadaschik, L.S. Marks, P. Mozer, A.R. Rastinehad, H.U. Ahmed, Detection of Clinically Significant Prostate Cancer Using Magnetic Resonance Imaging–Ultrasound Fusion Targeted Biopsy: A Systematic Review, Eur. Urol. 68 (2015) 8–19. doi:10.1016/j.eururo.2014.10.026.

[16] N. Mendhiratta, A.B. Rosenkrantz, X. Meng, J.S. Wysock, M. Fenstermaker, R. Huang, F.-M. Deng, J. Melamed, M. Zhou, W.C. Huang, H. Lepor, S.S. Taneja, Magnetic Resonance Imaging-Ultrasound Fusion Targeted Prostate Biopsy in a Consecutive Cohort of Men with No Previous Biopsy: Reduction of Over Detection through Improved Risk Stratification, J. Urol. 194 (2015) 1601–1606. doi:10.1016/j.juro.2015.06.078.

[17] C.P. Filson, S. Natarajan, D.J.A. Margolis, J. Huang, P. Lieu, F.J. Dorey, R.E. Reiter, L.S. Marks, Prostate cancer detection with magnetic resonance-ultrasound fusion biopsy: The role of systematic and targeted biopsies, Cancer. 122 (2016) 884–892. doi:10.1002/cncr.29874.

[18] D.R.K. Shastri, Fine Needle Aspiration Cytology Verses Trucut Biopsy In Preoperative Planning Of Surgical Treatment Of Breast Lumps, IOSR J. Dent. Med. Sci. 15 (2016) 74–80. doi:10.9790/0853-150767480.

[19] A. Kar, B. Satapathy, K. Pattnaik, P. Dash, Trucut biopsy vs FNAC of pelvic tumors-who wins the match?, J. Cytol. 35 (2018) 179. doi:10.4103/JOC.JOC_63_18.

[20] M.J. Levy, M. Lou Jondal, J. Clain, M.J. Wiersema, Preliminary experience with an EUS-guided trucut biopsy needle compared with EUS-guided FNA, Gastrointest. Endosc. 57 (2003) 101–106. doi:10.1067/mge.2003.49.

[21] W.W. Lam, W.C. Chu, G.M. Tse, T.K. Ma, A.P. Tang, Role of fine needle aspiration and tru cut biopsy in diagnosis of mucinous carcinoma of breast—from a radiologist's perspective, Clin. Imaging. 30 (2006) 6–10. doi:10.1016/j.clinimag.2005.06.031.

[22] G. Kalambokis, P. Manousou, S. Vibhakorn, L. Marelli, E. Cholongitas, M. Senzolo, D. Patch, A.K. Burroughs, Transjugular liver biopsy – Indications, adequacy, quality of specimens, and complications – A systematic review, J. Hepatol. 47 (2007) 284–294.

doi:10.1016/j.jhep.2007.05.001.

[23] D. Halstuch, J. Baniel, D. Lifshitz, S. Sela, Y. Ber, D. Margel, Assessment of Needle Tip Deflection During Transrectal Guided Prostate Biopsy: Implications for Targeted Biopsies, J. Endourol. 32 (2018) 252–256. doi:10.1089/end.2017.0694.

[24] A.D.R. Li, J. Plott, L. Chen, J.S. Montgomery, A.J. Shih, Needle Deflection and Tissue Sampling Length in Needle Biopsy, J. Mech. Behav. Biomed. Mater. (2019) (Submitted).

[25] N. Abolhassani, R. Patel, M. Moallem, Needle insertion into soft tissue: A survey, Med. Eng. Phys. 29 (2007) 413–431. doi:10.1016/j.medengphy.2006.07.003.

[26] T.M. Kim, S.-H. Jung, I.-P. Baek, S.-H. Lee, Y.-J. Choi, J.-Y. Lee, Y.-J. Chung, S.-H. Lee, Regional biases in mutation screening due to intratumoural heterogeneity of prostate cancer, J. Pathol. 233 (2014) 425–435. doi:10.1002/path.4380.

[27] P.C. Mozer, A.W. Partin, D. Stoianovici, Robotic image-guided needle interventions of the prostate., Rev. Urol. 11 (2009) 7.

[28] S.P. DiMaio, G.S. Fischer, S.J. Haker, N. Hata, I. Iordachita, C.M. Tempany, R. Kikinis, G. Fichtinger, A System for MRI-guided Prostate Interventions, in: First IEEE/RAS-EMBS Int. Conf. Biomed. Robot. Biomechatronics, 2006. BioRob 2006., IEEE, 2006: pp. 68–73. doi:10.1109/BIOROB.2006.1639062.

[29] A. Muthigi, A.K. George, A. Sidana, M. Kongnyuy, R. Simon, V. Moreno, M.J. Merino, P.L. Choyke, B. Turkbey, B.J. Wood, P.A. Pinto, Missing the Mark: Prostate Cancer Upgrading by Systematic Biopsy over Magnetic Resonance Imaging/Transrectal Ultrasound Fusion Biopsy, J. Urol. 197 (2017) 327–334. doi:10.1016/j.juro.2016.08.097.

[30] S. Loeb, H.B. Carter, S.I. Berndt, W. Ricker, E.M. Schaeffer, Complications After Prostate Biopsy: Data From SEER-Medicare, J. Urol. 186 (2011) 1830–1834. doi:10.1016/j.juro.2011.06.057.

[31] M. Mahvash, P.E. Dupont, Fast needle insertion to minimize tissue deformation and damage, in: 2009 IEEE Int. Conf. Robot. Autom., IEEE, 2009: pp. 3097–3102. doi:10.1109/ROBOT.2009.5152617.

[32] M. Giovannini, H. Ren, J. Cao, K. Ehmann, Study on design and cutting parameters of rotating needles for core biopsy, J. Mech. Behav. Biomed. Mater. 86 (2018) 43–54. doi:10.1016/j.jmbbm.2018.06.013.

[33] N.J. van de Berg, D.J. van Gerwen, J. Dankelman, J.J. van den Dobbelsteen, Design Choices

in Needle Steering—A Review, IEEE/ASME Trans. Mechatronics. 20 (2015) 2172–2183. doi:10.1109/TMECH.2014.2365999.

[34] N. Abolhassani, R. Patel, M. Moallem, Control of soft tissue deformation during robotic needle insertion, Minim. Invasive Ther. Allied Technol. 15 (2006) 165–176. doi:10.1080/13645700600771645.

[35] S. Badaan, D. Petrisor, C. Kim, P. Mozer, D. Mazilu, L. Gruionu, A. Patriciu, K. Cleary, D. Stoianovici, Does needle rotation improve lesion targeting?, Int. J. Med. Robot. Comput. Assist. Surg. 7 (2011) 138–147. doi:10.1002/rcs.381.

[36] A.C. Barnett, K. Wolkowicz, J.Z. Moore, Vibrating Needle Cutting Force, in: ASME 2014 Int. Manuf. Sci. Eng. Conf., ASME, 2014: p. V002T02A025. doi:10.1115/MSEC2014-4049.

[37] A.C. Barnett, J.A. Jones, Y. Lee, J.Z. Moore, Compliant Needle Vibration Cutting of Soft Tissue, J. Manuf. Sci. Eng. 138 (2016) 111011. doi:10.1115/1.4033690.

[38] M.J. Oldfield, A. Leibinger, T.E.T. Seah, F. Rodriguez y Baena, Method to Reduce Target Motion Through Needle–Tissue Interactions, Ann. Biomed. Eng. 43 (2015) 2794–2803. doi:10.1007/s10439-015-1329-0.

[39] J.Z. Moore, Q. Zhang, C.S. McGill, H. Zheng, P.W. McLaughlin, A.J. Shih, Modeling of the Plane Needle Cutting Edge Rake and Inclination Angles for Biopsy, J. Manuf. Sci. Eng. 132 (2010). doi:10.1115/1.4002190.

[40] B.L. Tai, Y. Wang, A.J. Shih, Cutting Force of Hollow Needle Insertion in Soft Tissue, in: Vol. 1 Process., ASME, 2013: p. V001T01A007. doi:10.1115/MSEC2013-1124.

[41] J.Z. Moore, K. Malukhin, A.J. Shih, K.F. Ehmann, Hollow needle tissue insertion force model, CIRP Ann. 60 (2011) 157–160. doi:10.1016/j.cirp.2011.03.101.

[42] J.Z. Moore, P.W. McLaughlin, A.J. Shih, Novel needle cutting edge geometry for end-cut biopsy, Med. Phys. 39 (2011) 99–108. doi:10.1118/1.3665253.

[43] Y. Podder, T., Clark, D., Sherman, J., Fuller, D., Messing, E., Rubens, D., Strang, J., Zhang, Y., O'Dell, W., Ng, W. and Yu, Effects of tip geometry of surgical needles: an assessment of force and deflection, IFMBE Proc. 11 (2005) 1727–1983.

[44] M.D. O'Leary, C. Simone, T. Washio, K. Yoshinaka, A.M. Okamura, Robotic needle insertion: effects of friction and needle geometry, in: 2003 IEEE Int. Conf. Robot. Autom. (Cat. No.03CH37422), IEEE, 2003: pp. 1774–1780. doi:10.1109/ROBOT.2003.1241851.

[45] A.M. Okamura, C. Simone, M.D. O'Leary, Force Modeling for Needle Insertion Into Soft Tissue, IEEE Trans. Biomed. Eng. 51 (2004) 1707–1716. doi:10.1109/TBME.2004.831542.

[46] K.W. Ng, J.Q. Goh, S.L. Foo, P.H. Ting, T.K. Lee, K. Esuvaranathan, Q.H. Wu, E. Chiong, Needle Deflection Studies for Optimal Insertion Modeling, Int. J. Biosci. Biochem. Bioinforma. 3 (2013) 570–574. doi:10.7763/IJBBB.2013.V3.278.

[47] N.J. Cowan, K. Goldberg, G.S. Chirikjian, G. Fichtinger, R. Alterovitz, K.B. Reed, V. Kallem, W. Park, S. Misra, A.M. Okamura, Surgical Robotics, Springer US, Boston, MA, 2011. doi:10.1007/978-1-4419-1126-1.

[48] T. Lehmann, C. Rossa, N. Usmani, R.S. Sloboda, M. Tavakoli, A Real-Time Estimator for Needle Deflection During Insertion Into Soft Tissue Based on Adaptive Modeling of Needle-Tissue Interactions, IEEE/ASME Trans. Mechatronics. 21 (2016) 2601–2612. doi:10.1109/TMECH.2016.2598701.

[49] S. Jiang, X. Wang, Mechanics-Based Interactive Modeling for Medical Flexible Needle Insertion in Consideration of Nonlinear Factors, J. Comput. Nonlinear Dyn. 11 (2016) 011004. doi:10.1115/1.4030747.

[50] S. Misra, K.B. Reed, A.S. Douglas, K.T. Ramesh, A.M. Okamura, Needle-tissue interaction forces for bevel-tip steerable needles, in: 2008 2nd IEEE RAS EMBS Int. Conf. Biomed. Robot. Biomechatronics, IEEE, 2008: pp. 224–231. doi:10.1109/BIOROB.2008.4762872.

[51] M. Oldfield, D. Dini, G. Giordano, F. Rodriguez y Baena, Detailed finite element modelling of deep needle insertions into a soft tissue phantom using a cohesive approach, Comput. Methods Biomech. Biomed. Engin. 16 (2013) 530–543. doi:10.1080/10255842.2011.628448.

[52] H. Lee, J. Kim, Intelligent Autonomous Systems 13, Springer International Publishing, Cham, 2016. doi:10.1007/978-3-319-08338-4.

[53] G. Fichtinger, J.P. Fiene, C.W. Kennedy, G. Kronreif, I. Iordachita, D.Y. Song, E.C. Burdette, P. Kazanzides, Robotic assistance for ultrasound-guided prostate brachytherapy, Med. Image Anal. 12 (2008) 535–545. doi:10.1016/j.media.2008.06.002.

[54] A. Krieger, S.-E. Song, N.B. Cho, I.I. Iordachita, P. Guion, G. Fichtinger, L.L. Whitcomb, Development and Evaluation of an Actuated MRI-Compatible Robotic System for MRI-Guided Prostate Intervention, IEEE/ASME Trans. Mechatronics. 18 (2013) 273–284.

doi:10.1109/TMECH.2011.2163523.

[55] D. Stoianovici, C. Jun, S. Lim, P. Li, D. Petrisor, S. Fricke, K. Sharma, K. Cleary, Multi-Imager Compatible, MR Safe, Remote Center of Motion Needle-Guide Robot, IEEE Trans. Biomed. Eng. 65 (2018) 165–177. doi:10.1109/TBME.2017.2697766.

[56] G.I. Barbash, S.A. Glied, New technology and health care costs—the case of robot-assisted surgery, N. Engl. J. Med. 363 (2010) 701–704.

[57] S. Kasraeian, D.C. Allison, E.R. Ahlmann, A.N. Fedenko, L.R. Menendez, A Comparison of Fine-needle Aspiration, Core Biopsy, and Surgical Biopsy in the Diagnosis of Extremity Soft Tissue Masses, Clin. Orthop. Relat. Res. 468 (2010) 2992–3002. doi:10.1007/s11999-010-1401-x.

[58] Y.J. Yang, T.A. Damron, Comparison of Needle Core Biopsy and Fine-Needle Aspiration for Diagnostic Accuracy in Musculoskeletal Leisons, Arch. Pathol. Lab. Med. 128 (2004) 759–764.

[59] W. Li, P. Zhou, W.-C. Lin, V. Nteziyaremye, H. Yamaguchi, D. Guo, A. Shih, Effects of needle inner surface topography on friction and biopsy length, Int. J. Mech. Sci. 119 (2016) 412–418. doi:10.1016/j.ijmecsci.2016.11.005.

[60] S. Aoyagi, Y. Takaoki, H. Takayanagi, C. Huang, T. Tanaka, M. Suzuki, T. Takahashi, T. Kanzaki, T. Matsumoto, Equivalent negative stiffness mechanism using three bundled needles inspired by mosquito for achieving easy insertion, in: 2012 IEEE/RSJ Int. Conf. Intell. Robot. Syst., IEEE, 2012: pp. 2295–2300. doi:10.1109/IROS.2012.6386088.

[61] M.K. Ramasubramanian, O.M. Barham, V. Swaminathan, Mechanics of a mosquito bite with applications to microneedle design, Bioinspir. Biomim. 3 (2008) 046001. doi:10.1088/1748-3182/3/4/046001.

[62] A. Sakes, D. Dodou, P. Breedveld, Buckling prevention strategies in nature as inspiration for improving percutaneous instruments: a review, Bioinspir. Biomim. 11 (2016) 021001. doi:10.1088/1748-3190/11/2/021001.

[63] D. Gurera, B. Bhushan, N. Kumar, Lessons from mosquitoes' painless piercing, J. Mech. Behav. Biomed. Mater. 84 (2018) 178–187. doi:10.1016/j.jmbbm.2018.05.025.

[64] S. Aoyagi, H. Izumi, M. Fukuda, Biodegradable polymer needle with various tip angles and consideration on insertion mechanism of mosquito's proboscis, Sensors Actuators A Phys. 143 (2008) 20–28. doi:10.1016/j.sna.2007.06.007.

[65] M.J. Leveridge, A. Finelli, J.R. Kachura, A. Evans, H. Chung, D.A. Shiff, K. Fernandes, M.A.S. Jewett, Outcomes of Small Renal Mass Needle Core Biopsy, Nondiagnostic Percutaneous Biopsy, and the Role of Repeat Biopsy, Eur. Urol. 60 (2011) 578–584. doi:10.1016/j.eururo.2011.06.021.

[66] K. Oka, S. Aoyagi, Y. Arai, Y. Isono, G. Hashiguchi, H. Fujita, Fabrication of a micro needle for a trace blood test, Sensors Actuators A Phys. 97–98 (2002) 478–485. doi:10.1016/S0924-4247(01)00872-X.

[67] M. Sahlabadi, S. Khodaei, K. Jezler, P. Hutapea, Insertion mechanics of bioinspired needles into soft tissues, Minim. Invasive Ther. Allied Technol. 27 (2018) 284–291. doi:10.1080/13645706.2017.1418753.

[68] H. Izumi, T. Yajima, S. Aoyagi, N. Tagawa, Y. Arai, M. Hirata, S. Yorifuji, Combined Harpoonlike Jagged Microneedles Imitating Mosquito's Proboscis and Its Insertion Experiment with Vibration, IEEJ Trans. Electr. Electron. Eng. 3 (2008) 425–431. doi:10.1002/tee.20295.

[69] H. Izumi, M. Suzuki, S. Aoyagi, T. Kanzaki, Realistic imitation of mosquito's proboscis: Electrochemically etched sharp and jagged needles and their cooperative inserting motion, Sensors Actuators A Phys. 165 (2011) 115–123. doi:10.1016/j.sna.2010.02.010.

[70] W. Li, B. Belmont, J.M. Greve, A.B. Manders, B.C. Downey, X. Zhang, Z. Xu, D. Guo, A. Shih, Polyvinyl chloride as a multimodal tissue-mimicking material with tuned mechanical and medical imaging properties, Med. Phys. 43 (2016) 5577–5592. doi:10.1118/1.4962649.

[71] D.R. Li, J.K. Yeh, W. Lin, J.S. Montgomery, A. Shih, An Experimental Method of Needle Deflection and Prostate Movement Using the Anatomically Accurate Prostate Simulator and the Electromagnetic Tracking System, in: Vol. 4 Bio Sustain. Manuf., ASME, 2017: p. V004T05A010. doi:10.1115/MSEC2017-3000.

[72] D.R. Li, J.K. Yeh, K. Putra, A. Shih, Optical Measurement of Tissue Deformation in Needle Insertion, Procedia CIRP. 65 (2017) 175–179. doi:10.1016/j.procir.2017.04.051.

[73] J.M. Correas, A.-M. Tissier, A. Khairoune, G. Khoury, D. Eiss, O. Hélénon, Ultrasound elastography of the prostate: State of the art, Diagn. Interv. Imaging. 94 (2013) 551–560. doi:10.1016/j.diii.2013.01.017.

[74] R.G. Barr, R. Memo, C.R. Schaub, Shear Wave Ultrasound Elastography of the Prostate, Ultrasound Q. 28 (2012) 13–20. doi:10.1097/RUQ.0b013e318249f594.

[75] S. Okazawa, R. Ebrahimi, J. Chuang, S.E. Salcudean, R. Rohling, Hand-Held Steerable Needle Device, IEEE/ASME Trans. Mechatronics. 10 (2005) 285–296. doi:10.1109/TMECH.2005.848300.

[76] J. Blaber, B. Adair, A. Antoniou, Ncorr: Open-Source 2D Digital Image Correlation Matlab Software, Exp. Mech. 55 (2015) 1105–1122. doi:10.1007/s11340-015-0009-1.

[77] D.R. Li, J.K. Yeh, K. Putra, A. Shih, Optical Measurement of Tissue Deformation in Needle Insertion, in: Procedia CIRP, 2017. doi:10.1016/j.procir.2017.04.051.

[78] G. Qiu, S. Henke, J. Grabe, Application of a Coupled Eulerian–Lagrangian approach on geomechanical problems involving large deformations, Comput. Geotech. 38 (2011) 30–39. doi:10.1016/j.compgeo.2010.09.002.

[79] F. Ducobu, E. Rivière-Lorphèvre, E. Filippi, Finite element modelling of 3D orthogonal cutting experimental tests with the Coupled Eulerian-Lagrangian (CEL) formulation, Finite Elem. Anal. Des. 134 (2017) 27–40. doi:10.1016/j.finel.2017.05.010.

[80] J.T. Ferrucci, J. Wittenberg, CT Biopsy of Abdominal Tumors: Aids for Lesion Localization, Radiology. 129 (1978) 739–744. doi:10.1148/129.3.739.

[81] G.J. Ridder, K. Technau-Ihling, C.C. Boedeker, Ultrasound-Guided Cutting Needle Biopsy in the Diagnosis of Head and Neck Masses, Laryngoscope. 115 (2005) 376–377. doi:10.1097/01.mlg.0000154750.09303.36.

[82] S.F. Atashzar, I. Khalaji, M. Shahbazi, A. Talasaz, R. V. Patel, M.D. Naish, Robot-assisted lung motion compensation during needle insertion, in: 2013 IEEE Int. Conf. Robot. Autom., IEEE, 2013: pp. 1682–1687. doi:10.1109/ICRA.2013.6630796.

[83] Y. Zhou, K. Thiruvalluvan, L. Krzeminski, W.H. Moore, Z. Xu, Z. Liang, CT-guided robotic needle biopsy of lung nodules with respiratory motion - experimental system and preliminary test, Int. J. Med. Robot. Comput. Assist. Surg. 9 (2013) 317–330. doi:10.1002/rcs.1441.

[84] Y. Wang, B.L. Tai, R.K. Chen, A.J. Shih, The Needle With Lancet Point: Geometry for Needle Tip Grinding and Tissue Insertion Force, J. Manuf. Sci. Eng. 135 (2013) 041010. doi:10.1115/1.4023718.

[85] R. Alterovitz, J. Pouliot, R. Taschereau, I.C. Joe Hsu, K. Goldberg, Simulating needle insertion and radioactive seed implantation for prostate brachytherapy, Stud. Health Technol. Inform. 94 (2003) 19–25. doi:10.3233/978-1-60750-938-7-19.

[86] S.P. DiMaio, S.E. Salcudean, Needle insertion modeling and simulation, Ieee Trans. Robot. Autom. 19 (2003) 864–875. doi:10.1109/Tra.2003.817044.

[87] Y. Liu, Y. Zheng, A.D.R. Li, Y. Liu, L.E. Savastano, A.J. Shih, Cutting of blood clots – Experiment and smooth particle Galerkin modelling, CIRP Ann. 68 (2019) 97–100. doi:10.1016/j.cirp.2019.04.025.

[88] C.T. Wu, Y. Guo, W. Hu, An Introduction to the LS-DYNA ® Smoothed Particle Galerkin Method for Severe Deformation and Failure Analyses in Solids, 13th Int. LS-DYNA Users Conf. (2014) 1–20.

[89] Y. Wu, C.T. Wu, W. Hu, Parametric and Convergence Studies of the Smoothed Particle Galerkin (SPG) Method in Semi-brittle and Ductile Material Failure Analyses, 15th Int. LS-DYNA Users Conf. (2018) 1–12.

[90] K.J. Bathe, Finite Element Procedures, 2014.

[91] J.G. Snedeker, P. Niederer, F.R. Schmidlin, M. Farshad, C.K. Demetropoulos, J.B. Lee, K.H. Yang, Strain-rate dependent material properties of the porcine and human kidney capsule, J. Biomech. 38 (2005) 1011–1021. doi:10.1016/j.jbiomech.2004.05.036.